NORTHWESTERN UNIVERSITY

Nonlocal Correlations in a Proximity-coupled Normal metal

A DISSERTATION

SUBMITTED TO THE GRADUATE SCHOOL

IN PARTIAL FULFILLMENT OF THE REQUIREMENTS

for the degree

DOCTOR OF PHILOSOPHY

Field of Physics and Astronomy

By

Taewan Noh

EVANSTON, ILLINOIS

December 2019

ABSTRACT

Nonlocal Correlations in a Proximity-coupled Normal metal

Taewan Noh

A superconductor-normal metal-superconductor (SNS) junction is capable of carrying supercurrent due to the Josephson coupling between the two superconductors. More interestingly, this coupling is maintained through the normal metal in a length determined by the Thouless energy of the normal metal, which can be a few microns, much longer than the case of conventional Josephson junction consisting of two superconductors separated by a thin insulator, where the thickness is only a few nanometers. This provides us with a capability of measuring the electric potential in the proximity-coupled normal metal by placing multiple probes on it. In particular, in this thesis we present the experimental results of our attempt to search nonlocal correlations mediated by a proximity-coupled normal metal via electrical transport measurements. At very low temperatures, with an overall dependence on the bias current seemingly analogous to that observed in prior experiments on NSN structures, the nonlocal differential resistance exhibits a peculiar dip in a small range of bias current. In addition to the qualitative explanation that accounts for the nonlocal differential resistance arising from the separation of quasiparticle current due to the Josephson coupling between

the two superconductors, further analysis based on the quasiclassical theory of superconductivity reveals that the central dip can be attributed to penetration of pair correlations into the proximity-coupled normal metal from both superconductors in a coherent manner. While the processes analogous to crossed Andreev reflection and elastic cotunneling observed in a superconductor are yet to be found, our data and analysis provide insights on the physics behind the interplay between the quasiparticle current and the supercurrent which gives rise to the observed nonlocal correlations in a proximity-coupled normal metal.

Beside the nonlocal correlations in a proximity-coupled normal metal, we also investigated electrical transport through a heterostructure including double superconductor-ferromagnet (FS) interfaces. In addition to a typical signature of spin imbalance due to the Zeeman splitting in the density of states (DOS) of the quasiparticles in a superconductor, an interesting feature in a small range of bias current has been observed, which might be related to spin-dependent phenomena at FS interfaces although further investigation in a simpler geometry of the sample is required to elucidate the exact mechanism.

Acknowledgments

I would like to thank many people who have supported me throughout my journey as a graduate student at Northwestern.

Prof. Venkat Chandrasekhar, my academic advisor, has been an excellent teacher who patiently taught me with his vast amount of knowledge and insight on various topics ranging from fundamental condensed matter physics to thorough technical skills, which I believe has shaped me as a physicist.

I would also like to thank Prof. Matthew Grayson and Prof. Jens Koch for being on my committee and providing insightful comments on my thesis.

Prof. Dima Dikin, Prof. Jian Wei and Prof. Goutam Sheet were early members of the group as a research professor and post-docs when I joined and I owe them knowledge on the basics of superconductivity and experimental skills.

My life in the lab has become by far more fun and enjoyable with my labmates, Manan Mehta, Scott Mayle, Varada Bal, and Sam Davis. We shared the joys and sorrows of life in the lab while discussing physics, helping one another for experiments, and grabbing beers to chill out. Manan also had been my flatmate for three years and we encouraged each other especially when life was somewhat difficult like a "slider", rather than a "full toss". Sam was a junior student who worked with me for some of the work in the thesis and he was always ready to discuss physics behind the data.

I am very grateful for my parents and my brother for supporting me and cheering me up with their love even though I was far away from home.

Last, but not least, I would like to thank my wife Seyoung Ryu for her love and patience ever since I met her. I dedicate this thesis to her as it would have not been completed without her.

Table of Contents

List of Tables

List of Figures

CHAPTER 1

Introduction

Quantum entanglement is one of the key features that provide a clear distinction between quantum mechanics and its classical counterpart. Over many decades, there have been enormous amount of efforts and attempts to construct, detect, and manipulate the entanglement between two quantum objects. In the field of solid state physics, superconductors have been considered as a natural source of entangled quantum objects since the ground state of a conventional s-wave superconductor is formed by the condensation of electron pairs with singlet spin configuration, called Cooper pairs.

Recently, many experiments including the pioneering works by Beckmann [**1**], Russo [**2**], and Cadden-Zimansky [**3**] have been performed to observe the entanglement, in other words, *nonlocal correlation*, between two spatially separated electrons mediated by a superconductor. Moreover, the Cooper pair beam splitter where a Cooper pair is split into two electrons along separate paths through the quantum dots has been experimentally realized in the work of Hofstetter [**4**] and Herrmann [**5**]. From these works, it has been shown that two nonlocal processes, crossed Anreev reflection (CAR) and elastic cotunneling (EC), contribute to the correlation between two electrons spatially separated within the range of the coherence length of superconductor ξ_S of the order of a few hundreds of nanometers.

Intrigued by these earlier experiments, we have attempted to observe the nonlocal correlations of two electrons mediated by a proximity-coupled normal metal. The unique properties of the superconductor can migrate into a normal metal placed adjacent to a superconductor due to the proximity effect, which modifies the electronic properties of the normal metal. In particular, a proximity-coupled normal metal placed in between two superconductors is capable of carrying a finite amount of dissipationless supercurrent and also exhibits a "mini gap" in the density of states. However, the relevant energy scale for the proximity-coupled normal metal with diffusion constant D and the length L is the Thouless energy $E_T = \hbar D/L^2$ which can be much smaller than the gap of the superconductor in the long junction limit. In terms of the length scale, the Thouless length $L_T = \sqrt{\hbar D/k_B T}$ can be much longer than ξ_S at low temperatures T. If the entanglement between two electrons can be mediated by a proximity-coupled normal metal within such an extended length scale, it might open up a new possibility of a number of applications in the field of quantum information. With this motivation in mind, the goal of this thesis is to present the experimental work that we performed to probe the nonlocal correlations in a proximity-coupled normal metal and to provide the analysis to figure out the physical origin behind the observed result.

This thesis is organized as follows:

Chapter 2 consists of two parts. In the first part, I provide a brief review of theoretical approaches that help understand the physical phenomena occurring in superconducting heterostructures including the numerical recipe to implement the quasiclassical theory of superconductivity. In the second part, I present our theoretical proposal on the investigation of nonlocal correlations mediated by pure spin current.

In Chapter 3, I explain the experimental procedures and techniques used to obtain the experimental results.

In Chapter 4, the main chapter of this thesis, I present the experimental results of the investigation of the nonlocal correlation mediated by a proximity-coupled normal metal in different samples with different geometries.

In Chapter 5, as a separate experimental result, I report our experimental work on superconductor-ferromagnet heterostures along with a brief summary of related recent studies on spin imbalance.

In Chapter 6, I summarize our finding with some suggestions for future experiments.

CHAPTER 2

Theoretical Background

I. Charge transport through normal metal - superconductor heterostructures

In order to analyze the transport properties through heterostructures including a superconductor, it is helpful to acquire a qualitative picture on the processes occurring at the interface as well as an understanding based on detailed quantitative theoretical descriptions. For that purpose, in this chapter, I will review some of the theoretical approaches developed in the last few decades in addition to the explanation on the basics of key concepts necessary to understand the motivation and analysis of the experiments performed for this thesis.

2.1. Superconductivity

Before considering the processes occurring at the interface between normal metal (N) and superconductor (S), let us take a look at the properties of the superconductor. Ever since the observation of superconductivity in metals at low temperatures by Onnes [**6**], there have been many attempts to explain the origin of the superconductiviy from the phenomenological point of view. In 1957, Bardeen, Cooper, and Schrieffer (BCS) came up with the first microscopic theory of superconductivity [**7**]. They described that superconductivity is caused by a condensation of electron-pairs, named Cooper pairs [**8**], into a bosonic state. According to the theory, the formation of such a ground state consisting of Cooper pairs is favored due to the existence of the attractive interaction between electrons mediated by the virtual exchange of phonons, a collective excitation of the atomic lattice. For this thesis, instead of discussing all the aspects of the superconductivity based on the work of BCS, I will introduce the formalism developed by Bogoliubov as described in the textbook written by Madelung [**9**]. In this way, we will be able to smoothly move on to the Blonder-Tinkham-Klapwijk (BTK) theory [**10**] for the discussion of the transport phenomena through NS interfaces in the following section.

Let us start with the many-body Hamiltonian of electron system in the presence of the attractive interaction,

$$\hat{H} = \sum_{\mathbf{k}\sigma} \epsilon_{\mathbf{k}} \hat{c}^{\dagger}_{\mathbf{k},\sigma} \hat{c}_{\mathbf{k},\sigma} - \frac{V}{2} \sum_{\mathbf{k}\mathbf{k}'\sigma} \hat{c}^{\dagger}_{\mathbf{k}',\sigma} \hat{c}^{\dagger}_{-\mathbf{k}',-\sigma} \hat{c}_{-\mathbf{k},-\sigma} \hat{c}_{\mathbf{k},\sigma} \tag{2.1}$$

The first term in Eq. (2.1) denotes the energy of the electron gas where $\hat{c}^{\dagger}_{\mathbf{k}\sigma}$ and $\hat{c}_{\mathbf{k}\sigma}$ are the creation and the annihilation operator of the electron with momentum $\mathbf{k}$ and spin σ, which satisfy the anticommutation relations for fermions,

$$\{c^{\dagger}_{\mathbf{k}\sigma}, c^{\dagger}_{\mathbf{k}'\sigma'}\} = 0, \quad \{c_{\mathbf{k}\sigma}, c_{\mathbf{k}'\sigma'}\} = 0, \quad \{c^{\dagger}_{\mathbf{k}\sigma}, c_{\mathbf{k}'\sigma}\} = \delta_{\mathbf{k}\mathbf{k}'}\delta_{\sigma\sigma'} \tag{2.2}$$

where $\{\hat{A}, \hat{B}\} = \hat{A}\hat{B} + \hat{B}\hat{A}$ for arbitrary operators $\hat{A}$ and $\hat{B}$. The energy of the electron $\epsilon_{\mathbf{k}}$ is defined with respect to the Fermi energy $\epsilon_{\mathbf{k}} = \frac{\hbar^2\mathbf{k}^2}{2m} - E_F$. The second term describes the attractive interaction $-V$ which is assumed to be nonzero only for the electrons satisfying $|\epsilon_{\mathbf{k}}|$, $|\epsilon_{\mathbf{k}'}| \leq \hbar\omega_D$ where ω_D is the Debye frequency. It should be noted that the attractive interaction is also assumed to occur between two electrons with momentum $\mathbf{k}$ and $-\mathbf{k}$ with antiparallel spin configuration [**8**].

The above Hamiltonian can be rearranged by introducing the following Bogoliubov operators

$$
\begin{aligned}
\text{(2.3)} \qquad & \hat{\gamma}_{\mathbf{k}} = u_{\mathbf{k}}\hat{c}_{\mathbf{k}} - v_{\mathbf{k}}\hat{c}^{\dagger}_{-\mathbf{k}}, \quad \hat{\gamma}_{-\mathbf{k}} = u_{\mathbf{k}}\hat{c}_{-\mathbf{k}} + v_{\mathbf{k}}\hat{c}^{\dagger}_{\mathbf{k}}, \\
& \hat{\gamma}^{\dagger}_{\mathbf{k}} = u_{\mathbf{k}}\hat{c}^{\dagger}_{\mathbf{k}} - v_{\mathbf{k}}\hat{c}_{-\mathbf{k}}, \quad \hat{\gamma}^{\dagger}_{-\mathbf{k}} = u_{\mathbf{k}}\hat{c}^{\dagger}_{-\mathbf{k}} + v_{\mathbf{k}}\hat{c}_{\mathbf{k}},
\end{aligned}
$$

which leads to

$$
\begin{aligned}
\text{(2.4)} \qquad \hat{H} \;=\; & \sum_{\mathbf{k}} \epsilon_{\mathbf{k}}[2v^2_{\mathbf{k}} + (u^2_{\mathbf{k}} - v^2_{\mathbf{k}})(\hat{\gamma}^{\dagger}_{\mathbf{k}}\hat{\gamma}_{\mathbf{k}} + \hat{\gamma}^{\dagger}_{-\mathbf{k}}\hat{\gamma}_{-\mathbf{k}}) + 2u_{\mathbf{k}}v_{\mathbf{k}}(\hat{\gamma}^{\dagger}_{\mathbf{k}}\hat{\gamma}^{\dagger}_{\mathbf{k}} + \hat{\gamma}_{-\mathbf{k}}\hat{\gamma}_{\mathbf{k}})] \\
- \; & V\sum_{\mathbf{k}\mathbf{k}'}[u_{\mathbf{k}}v_{\mathbf{k}}u_{\mathbf{k}'}v_{\mathbf{k}'}(1 - \hat{\gamma}^{\dagger}_{-\mathbf{k}'}\hat{\gamma}_{-\mathbf{k}'} - \hat{\gamma}^{\dagger}_{\mathbf{k}'}\hat{\gamma}_{\mathbf{k}'})(1 - \hat{\gamma}^{\dagger}_{-\mathbf{k}}\hat{\gamma}_{-\mathbf{k}} - \hat{\gamma}^{\dagger}_{\mathbf{k}}\hat{\gamma}_{\mathbf{k}}) \\
+ \; & (u^2_{\mathbf{k}} - v^2_{\mathbf{k}})u_{\mathbf{k}'}v_{\mathbf{k}'}(1 - \hat{\gamma}^{\dagger}_{-\mathbf{k}'}\hat{\gamma}_{-\mathbf{k}'} - \hat{\gamma}^{\dagger}_{\mathbf{k}'}\hat{\gamma}_{\mathbf{k}'})(\hat{\gamma}_{-\mathbf{k}}\hat{\gamma}_{\mathbf{k}} + \hat{\gamma}^{\dagger}_{\mathbf{k}}\hat{\gamma}^{\dagger}_{-\mathbf{k}}) \\
+ \; & (u^2_{\mathbf{k}}\hat{\gamma}_{-\mathbf{k}}\hat{\gamma}_{\mathbf{k}} - v^2_{\mathbf{k}}\hat{\gamma}^{\dagger}_{\mathbf{k}}\hat{\gamma}^{\dagger}_{-\mathbf{k}})(u^2_{\mathbf{k}'}\hat{\gamma}^{\dagger}_{\mathbf{k}'}\hat{\gamma}^{\dagger}_{-\mathbf{k}'} - v^2_{\mathbf{k}'}\hat{\gamma}_{-\mathbf{k}'}\hat{\gamma}_{\mathbf{k}'})].
\end{aligned}
$$

Here, the spin indices for the operators are omitted by assuming a chirality such that the index $\mathbf{k}$ and $-\mathbf{k}$ represent $\mathbf{k}\uparrow$ and $-\mathbf{k}\downarrow$, respectively. The transformation between $\hat{c}$ operators and $\hat{\gamma}$ operators is called the Bogoliubov-Valatin transformation. The operators $\hat{\gamma}^{\dagger}_{\mathbf{k}}$ and $\hat{\gamma}_{\mathbf{k}}$ are the creation and the annihilation operator of a quasiparticle with momentum $\mathbf{k}$, which satisfy the same anticommuntation relations as the electron with the relation $|u_{\mathbf{k}}|^2 + |v_{\mathbf{k}}|^2 = 1$. If we focus on the case of the ground state in which the number of quasiparticles is zero, we can neglect all the terms involving $\hat{\gamma}^{\dagger}_{\mathbf{k}}\hat{\gamma}_{\mathbf{k}}$. This simplifies the Hamiltonian in Eq. (2.4) to

$$
\begin{aligned}
\text{(2.5)} \qquad \hat{H} \;=\; & 2\sum_{\mathbf{k}} \epsilon_{\mathbf{k}} v^2_{\mathbf{k}} - V\sum_{\mathbf{k}\mathbf{k}'} u_{\mathbf{k}}v_{\mathbf{k}}u_{\mathbf{k}'}v_{\mathbf{k}'} \\
+ \; & \sum_{\mathbf{k}} \left[2u_{\mathbf{k}}v_{\mathbf{k}}\epsilon_{\mathbf{k}} - (u^2_{\mathbf{k}} - v^2_{\mathbf{k}})V\sum_{\mathbf{k}'} u_{\mathbf{k}'}v_{\mathbf{k}'}\right](\hat{\gamma}^{\dagger}_{\mathbf{k}}\hat{\gamma}^{\dagger}_{-\mathbf{k}} + \hat{\gamma}_{-\mathbf{k}}\hat{\gamma}_{\mathbf{k}}).
\end{aligned}
$$

By requiring the term in the bracket to vanish, the Hamiltonian is reduced to a constant, i.e., the ground state energy. By setting $\sum_{\mathbf{k}'} u_{\mathbf{k}'} v_{\mathbf{k}'}$ to a constant Δ/V, the following condition is obtained.

$$2u_{\mathbf{k}} v_{\mathbf{k}} \epsilon_{\mathbf{k}} = \Delta(u_{\mathbf{k}}^2 - v_{\mathbf{k}}^2) \tag{2.6}$$

It is straightforward to find

$$u_{\mathbf{k}} = \frac{1}{\sqrt{2}}\left(1 + \frac{\epsilon_{\mathbf{k}}}{E_{\mathbf{k}}}\right)^{1/2}, \quad v_{\mathbf{k}} = \frac{1}{\sqrt{2}}\left(1 - \frac{\epsilon_{\mathbf{k}}}{E_{\mathbf{k}}}\right)^{1/2} \tag{2.7}$$

by applying the relation $|u_{\mathbf{k}}|^2 + |v_{\mathbf{k}}|^2 = 1$, where $E_{\mathbf{k}} = (\Delta^2 + \epsilon_{\mathbf{k}}^2)^{1/2}$. The result for $u_{\mathbf{k}}$ and $v_{\mathbf{k}}$ is plotted in Figure 2.1. They show a smooth transition between 0 and 1 within the range of $-\Delta \leq \epsilon_{\mathbf{k}} \leq \Delta$.

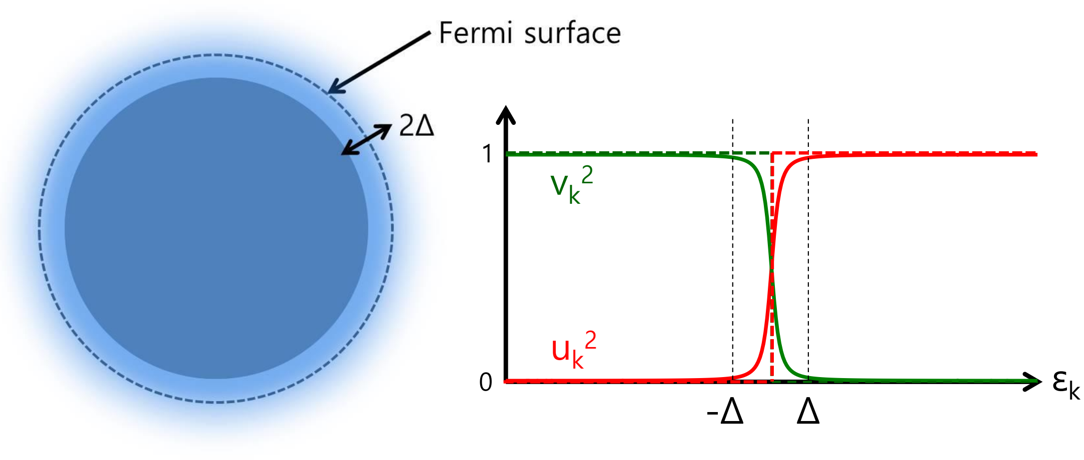

Figure 2.1. Left: In the presence of a small attractive potential V, electrons are rearranged from a Fermi gas (dotted line) to form Cooper pairs. The electrons within the range of $\pm\Delta$ from the Fermi surface probabilistically participate in the pair formation. Right: The occupation probability $u_{\mathbf{k}}^2$ (red solid line) and $v_{\mathbf{k}}^2$ (green solid line) for the BCS ground state. The dotted lines denote $u_{\mathbf{k}}^2$ and $v_{\mathbf{k}}^2$ in absence of the attractive potential.

With the results obtained for $u_{\mathbf{k}}$ and $v_{\mathbf{k}}$, we can calculate Δ by solving the following self-consistent equation,

$$\Delta = V \sum_{\mathbf{k}} u_{\mathbf{k}} v_{\mathbf{k}} = \frac{V}{2} \sum_{\mathbf{k}} \frac{\Delta}{\sqrt{\epsilon_{\mathbf{k}}^2 + \Delta^2}}. \tag{2.8}$$

The summation over the momentum $\mathbf{k}$ can be replaced by an integral including the density of state $N(\epsilon)$. If only energies near the Fermi surface are considered, $N(\epsilon) \simeq N(0)$, which leads to

$$1 = \frac{VN(0)}{4} \int_{-\hbar\omega_D}^{\hbar\omega_D} \frac{d\epsilon}{\sqrt{\epsilon^2 + \Delta^2}} \tag{2.9}$$

and eventually to

$$\Delta = 2\hbar\omega_D \mathrm{exp}[-2/N(0)V] \tag{2.10}$$

which corresponds to the binding energy of a Cooper pair [**7**]. Therefore, the spatial correlation between two electrons participating in the formation of the condensate of Cooper pairs can be estimated by Δ, translated into the length scale $\hbar v_F/\Delta$, which is called coherence length ξ_0. In the diffusive regime, however, there is a reduction of the coherence length by the mean free path l_e of the material, which leads to $\xi_S = \sqrt{\xi_0 l_e}$. In case of diffusive aluminum that we used in the experiments for this thesis, it is typically a few hundred nanometers.

Having calculated the binding energy Δ, the ground state energy E_g, with respect to the energy of the filled Fermi sphere without condensation E_0, can be calculated from 2.5,

$$
\begin{aligned}
E_g - E_0 &= 2\sum_{\mathbf{k}} \epsilon_{\mathbf{k}} v_{\mathbf{k}}^2 - V\sum_{\mathbf{k}\mathbf{k}'} u_{\mathbf{k}} v_{\mathbf{k}} u_{\mathbf{k}'} v_{\mathbf{k}'} - 2\sum_{k<k_F} \epsilon_{\mathbf{k}} \\
&= N(0)\int_0^{\hbar\omega_D} \left(\epsilon - \frac{1}{2}\frac{2\epsilon^2+\Delta^2}{\sqrt{\epsilon^2+\Delta^2}}\right) d\epsilon \simeq -\frac{N(0)\Delta^2}{4}
\end{aligned} \tag{2.11}
$$

where the final relation is valid only for the weak interaction regime, $\Delta \ll \hbar\omega_D$. Eq. (2.11) shows the amount of the condensation energy from the formation of the ground state consisting of Cooper pairs.

As we have diagonalized the Hamiltonian in Eq. (2.1) for the ground state by introducing the transformation given in Eq.(2.3), we can construct the wave function for the ground state by applying the quasiparticle operators with $u_{\mathbf{k}}$ and $v_{\mathbf{k}}$ as defined above to the vacuum state $|0\rangle$. The ground state in the absence of the attractive interaction, the filled Fermi sphere, is represented as

$$
|\Psi_0\rangle = \prod_{k<k_F} \hat{c}^\dagger_{\mathbf{k}} \hat{c}_{\mathbf{k}} |0\rangle, \tag{2.12}
$$

which can be expressed in terms of quasiparticle operators

$$
|\Psi_0\rangle = \prod_{\mathbf{k}} \hat{\gamma}_{\mathbf{k}} \hat{\gamma}_{-\mathbf{k}} = \prod_{\mathbf{k}} (u_{\mathbf{k}} \hat{c}_{\mathbf{k}} - v_{\mathbf{k}} \hat{c}^\dagger_{-\mathbf{k}})(u_{\mathbf{k}} \hat{c}_{-\mathbf{k}} - v_{\mathbf{k}} \hat{c}^\dagger_{\mathbf{k}})|0\rangle \tag{2.13}
$$

with $u_{\mathbf{k}}$ and $v_{\mathbf{k}}$ in the limit of $\Delta = 0$. The same operator can be generally used to construct the ground state for nonzero Δ. Therefore, the wave function for the ground state $|\Psi_g\rangle$ is given by

$$|\Psi_g\rangle = C\prod_{\mathbf{k}}(u_{\mathbf{k}}\hat{c}_{\mathbf{k}} - v_{\mathbf{k}}\hat{c}^{\dagger}_{-\mathbf{k}})(u_{\mathbf{k}}\hat{c}_{-\mathbf{k}} - v_{\mathbf{k}}\hat{c}^{\dagger}_{\mathbf{k}})|0\rangle$$
$$= C\prod_{\mathbf{k}}\left[u^2_{\mathbf{k}}\hat{c}_{\mathbf{k}}\hat{c}_{-\mathbf{k}} + u_{\mathbf{k}}v_{\mathbf{k}}(\hat{c}_{\mathbf{k}}\hat{c}^{\dagger}_{\mathbf{k}} - \hat{c}^{\dagger}_{-\mathbf{k}}\hat{c}_{-\mathbf{k}}) + v^2_{\mathbf{k}}\hat{c}^{\dagger}_{\mathbf{k}}\hat{c}^{\dagger}_{-\mathbf{k}}\right]|0\rangle$$
$$= C\prod_{\mathbf{k}}(u_{\mathbf{k}}v_{\mathbf{k}} + v^2_{\mathbf{k}}\hat{c}^{\dagger}_{\mathbf{k}}\hat{c}^{\dagger}_{-\mathbf{k}})|0\rangle \tag{2.14}$$

where C is a constant to normalize the wave function as $\langle\Psi_g|\Psi_g\rangle = 1$,

$$\langle\Psi_g|\Psi_g\rangle = |C|^2\langle 0|\prod_{\mathbf{k}}(u_{\mathbf{k}}v_{\mathbf{k}} + v^2_{\mathbf{k}}\hat{c}_{-\mathbf{k}}\hat{c}_{\mathbf{k}})|0\rangle(u_{\mathbf{k}}v_{\mathbf{k}} + v^2_{\mathbf{k}}\hat{c}^{\dagger}_{\mathbf{k}}\hat{c}^{\dagger}_{-\mathbf{k}})|0\rangle$$
$$= |C|^2\langle 0|\prod_{\mathbf{k}}(u^2_{\mathbf{k}}v^2_{\mathbf{k}} + v^4_{\mathbf{k}}\hat{c}_{-\mathbf{k}}\hat{c}_{\mathbf{k}}\hat{c}^{\dagger}_{\mathbf{k}}\hat{c}^{\dagger}_{-\mathbf{k}})|0\rangle = |C|^2\prod_{\mathbf{k}}(u^2_{\mathbf{k}}v^2_{\mathbf{k}} + v^4_{\mathbf{k}}) \tag{2.15}$$

which results in $|C|^2 = (\prod_{\mathbf{k}} v^2_{\mathbf{k}})^{-1}$. Therefore, the final expression for the wave function is

$$|\Psi_g\rangle\prod_{\mathbf{k}} = (u_{\mathbf{k}} + v_{\mathbf{k}}\hat{c}^{\dagger}_{\mathbf{k}}\hat{c}^{\dagger}_{-\mathbf{k}})|0\rangle. \tag{2.16}$$

Now we can understand the physical meaning of $u_{\mathbf{k}}$ and $v_{\mathbf{k}}$ used in the quasiparticle operators from the wave function of the ground state. While $u_{\mathbf{k}}$ can be interpreted as the probability amplitude for the pair state consisting of electrons with momentum $\mathbf{k}$ and $-\mathbf{k}$ to be unoccupied, $v_{\mathbf{k}}$ stands for the probability amplitude for the pair state to be occupied, to form the ground state. From the plot of $u_{\mathbf{k}}$ and $v_{\mathbf{k}}$ as a function of energy $\epsilon_{\mathbf{k}}$ in Figure 2.1, one can see that the states with energies $\epsilon_{\mathbf{k}} < -\Delta$ are pretty much all occupied and $\epsilon_{\mathbf{k}} > \Delta$ are almost unoccupied, which shows a deviation from the case for the ground state without the condensation only in the vicinity of $\pm\Delta$ with respect to the Fermi energy. It should be also noted from Eq. (2.3) that in the range of $\epsilon_{\mathbf{k}} \ll -\Delta$ the quasiparticle is essentially a hole state whereas in the range of $\epsilon_{\mathbf{k}} \gg \Delta$ the quasiparticle is essentially an electron state. However, in the range of energies within Δ from the Fermi surface where the electrons participate in forming the Cooper pairs, the quasiparticle is a mixture of an electron and a hole, being different from either of them. The schematic illustration of the distribution of electrons is shown in Figure 2.1.

Let us now discuss excitations from the ground state. For doing that, the terms in Eq. (2.4) including $\hat{\gamma}^{\dagger}_{\mathbf{k}}\hat{\gamma}_{\mathbf{k}}$ and $\hat{\gamma}^{\dagger}_{\mathbf{k}}\hat{\gamma}_{\mathbf{k}}$ that are ignored in case of the ground state should be taken into account. Straightforward algebra generates the energy with the excitations of quasiparticles with respect to the ground state energy

$$E - E_g = \sum_{\mathbf{k}} [\epsilon_{\mathbf{k}}(u_{\mathbf{k}}^2 - v_{\mathbf{k}}^2) + 2\Delta u_{\mathbf{k}} v_{\mathbf{k}}](n_{\mathbf{k}} + n_{-\mathbf{k}}) = \sum_{\mathbf{k}} \left(\sqrt{\epsilon_{\mathbf{k}}^2 + \Delta^2}\right) n_{\mathbf{k}} \tag{2.17}$$

where $n_{\mathbf{k}}$ is the number of quasiparticles with momentum $\mathbf{k}$, whose energy is given by $E_{\mathbf{k}} = \sqrt{\epsilon_{\mathbf{k}}^2 + \Delta^2}$. This evidently shows that at least the amount of energy Δ is required to excite a quasiparticle, hence there is no state available for quasiparticle excitations below $E < \Delta$. To be more specific, the density of states $N_S(E)$ in the superconductor can be obtained by equating $N_S(E)dE = N(\epsilon)d\epsilon$. Again, assuming that $N(\epsilon) = N(0)$ for a small energy range near the Fermi surface, the density of the states $N_S(E)$ is

$$\frac{N_S(E)}{N(0)} = \frac{d\epsilon}{dE} = \begin{cases} \frac{E}{\sqrt{E^2 - \Delta^2}} & E > \Delta \\ 0 & E < \Delta. \end{cases} \tag{2.18}$$

So far I have introduced the treatment of the ground state and the excitation of quasiparticles of the superconducting electron gas at a temperature $T = 0$. The energy dependence of $u_{\mathbf{k}}$ and $v_{\mathbf{k}}$ used in the quasiparticle operators was calculated by assuming that the expected number of quasiparticle $n_{\mathbf{k}}$ is zero for the ground state, which is no longer valid at a temperature $T \neq 0$. Instead, $n_{\mathbf{k}}$ should be replaced by the statistical distribution $f_{\mathbf{k}}(E_{\mathbf{k}}) = \left[\exp\left(\frac{E_{\mathbf{k}}}{k_B T}\right) + 1\right]^{-1}$ for the quasiparticle with energy $E_{\mathbf{k}}$. Then the condition equivalent to Eq. (2.6)

$$2u_{\mathbf{k}}v_{\mathbf{k}}\epsilon_{\mathbf{k}} = \Delta(T)(u_{\mathbf{k}}^2 - v_{\mathbf{k}}^2) \tag{2.19}$$

is obtained where $\Delta(T)$ is now defined by

$$\Delta(T) = V\sum_{\mathbf{k}'} u_{\mathbf{k}'}v_{\mathbf{k}'}(1 - 2f_{\mathbf{k}'}), \tag{2.20}$$

which leads to

$$1 = \frac{VN(0)}{4}\int_{-\hbar\omega_D}^{\hbar\omega_D} \frac{d\epsilon}{\sqrt{\epsilon^2 + \Delta^2(T)}}\left[1 - 2f\left(\frac{\sqrt{\epsilon^2 + \Delta^2(T)}}{k_B T}\right)\right] \tag{2.21}$$

corresponding to Eq. (2.9) for $T \neq 0$. By performing the numerical calculation, the temperature T_c satisfying the condition $\Delta(T_c) = 0$ can be obtained as

$$k_B T_c \simeq 0.57\Delta(0). \tag{2.22}$$

and T_c is called the critical temperature. Again in case of aluminum, for example, the experimental value of $\Delta(0) \simeq 180$ μeV and $T_c \simeq 1.2$ K is in good agreement with the above relation.

Up to this point, I have introduced the theoretical discussion of superconductivity. Even though it is far away from a complete description, it may be enough to understand the origin of some basic properties of superconductivity and to start considering the transport phenomena through an NS interface.

2.2. Blonder-Tinkham-Klapwijk (BTK) Theory

Blonder, Tinkham, and Klapwijk came up with a simple theory [**10**] that treats the transport through an NS interface as the transmission of a plane-wave-like wave function in one dimension. They describe the superconductor based on the work of Bogoliubov as I introduced in the previous section. By considering the possible processes occurring at the NS interface and applying the boundary conditions for the wave functions, they calculated the differential conductance through the interface.

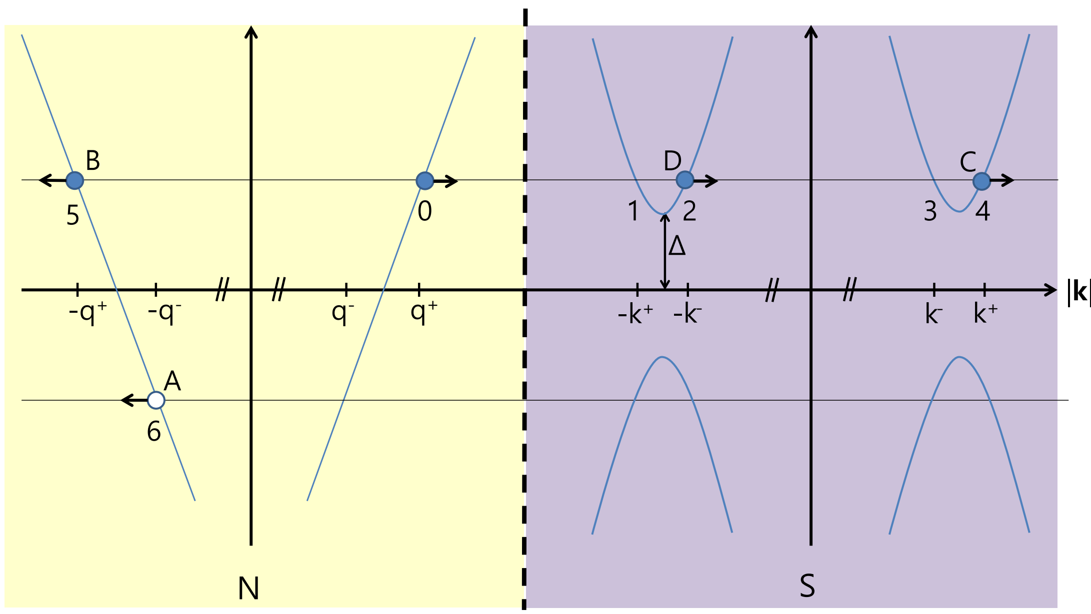

Figure 2.2. Schematic diagram of energy vs momentum at NS interface. The open circles denote holes, the closed circles electrons, and the arrows point in the direction of the group velocity. This figure describes an injected electron "0" resulting in transmitted "2","4" and reflected "5","6" particles. Figure is based on the original figure in Ref. [**10**].

To be more specific, let us consider an electron with energy E injected from the normal metal into the superconductor, indexed "0", as shown in Figure 2.2. Four processes can occur as a response to the injection of the electron with $E > \Delta$: On the normal metal side, Andreev [**11**] reflection indexed "6" occurs with the probability $A(E)$. During Andreev reflection, the injected electron is "retroreflected" as a hole back to the normal metal leaving a Cooper pair in the superconductor. The normal reflection where the injected electron is reflected back as an electron is indexed "5" and occurs with the probability $B(E)$. On the superconductor side, among the four degenerate solutions $\pm k^{\pm}$ for the quasiparticle energy spectrum $E_k = \sqrt{\epsilon_{k_\pm}^2 + \Delta^2}$, where $\epsilon_{k_\pm} = \frac{\hbar^2 k_\pm^2}{2m} - E_F$, two of the states indexed "2" and "4" with positive group velocity $dE/d(\hbar k)$ are accessible with the probability $C(E)$ and $D(E)$, respectively. In other words, $C(E)$ is the probability of transmission with a wave vector on the same side of the Fermi surface, $(q^+ \to k^+)$, whereas $D(E)$ is the probability of transmission with crossing through the Fermi surface, $(q^+ \to -k^-)$. It should be noted that the conservation of the probability requires that $A(E) + B(E) + C(E) + D(E) = 1$. Meanwhile, the potential of the interface between N and S is characterized in the form of a δ-function, $V(x) = H\delta(x)$, where the strength of the barrier H is expressed in terms of a dimensionless parameter $Z = H/\hbar v_F$. In a similar manner to solving the textbook quantum mechanics problem including a δ-function barrier, one can find the transmission and reflection coefficient as shown in the following table, Table. 2.1.

In case of no barrier, $Z = 0$, the probability of the Andreev reflection $A(E)$ approaches unity for electrons with energy $E < \Delta$, subgap energy. As the height of the barrier increases, Andreev reflection occurs less frequently and more electrons go through normal reflection, which reaches unity in the limit of $Z \to \infty$.

By using the transmission and reflection probabilities obtained above, the total current I through the NS interface under bias voltage V can be calculated as

$$I_{NS} = 2N(0)ev_F S \int_{-\infty}^{\infty} [f_0(E - eV) - f_0(E)][1 + A(E) - B(E)]dE \tag{2.23}$$

	$A(E)$	$B(E)$	$C(E)$	$D(E)$
Normal state	0	$\frac{Z^2}{1+Z^2}$	$\frac{1}{1+Z^2}$	0
General form				
$E < \Delta$	$\frac{\Delta^2}{E^2+(\Delta^2-E^2)(1+2Z^2)^2}$	$1 - A(E)$	0	0
$E > \Delta$	$\frac{u_0^2 v_0^2}{\gamma^2}$	$\frac{(u_0^2-v_0^2)Z^2(1+Z^2)}{\gamma^2}$	$\frac{u_0^2(u_0^2-v_0^2)(1+Z^2)}{\gamma^2}$	$\frac{v_0^2(u_0^2-v_0^2)Z^2}{\gamma^2}$

Table 2.1. Transmission and reflection probabilities. $A(E)$: Andreev reflection, $B(E)$: normal reflection, $C(E)$: transmission without branch crossing, and $D(E)$ transmission with branch crossing. $\gamma^2 = [u_0^2 + Z^2(u_0^2 - v_0^2)]$, $u_0^2 = 1 - v_0^2 = \frac{1}{2}\{1 + [(E^2 - \Delta^2)/E^2]^{1/2}\}$. Table is taken from Ref. [**10**].

where $N(0)$ is the density of states at the Fermi surface and S is the cross-sectional area of the interface, which leads to the normalized differential conductance $g_{NS} = R_N \frac{dI}{dV}$ at $T = 0$ given by

$$g_{NS}|_{T=0} = (1 + Z^2)[1 + A(E) - B(E)]. \tag{2.24}$$

The dependence of the normalized differential conductance on the bias voltage V at various barrier strengths Z is shown in Figure 2.3. In case of no barrier, $Z = 0$, which results in only Andreev reflection, the normalized differential conductance is doubled for the bias voltage $V < |\Delta|$ since the injection of an electron results in a Cooper pair consisting of two electrons during Andreev reflection. In the other limit of $Z \to \infty$, corresponding to tunnel junction, the subgap transport is completely suppressed resulting in the normalized differential conductance analogous to the density of states $N(E)$ of the superconductor.

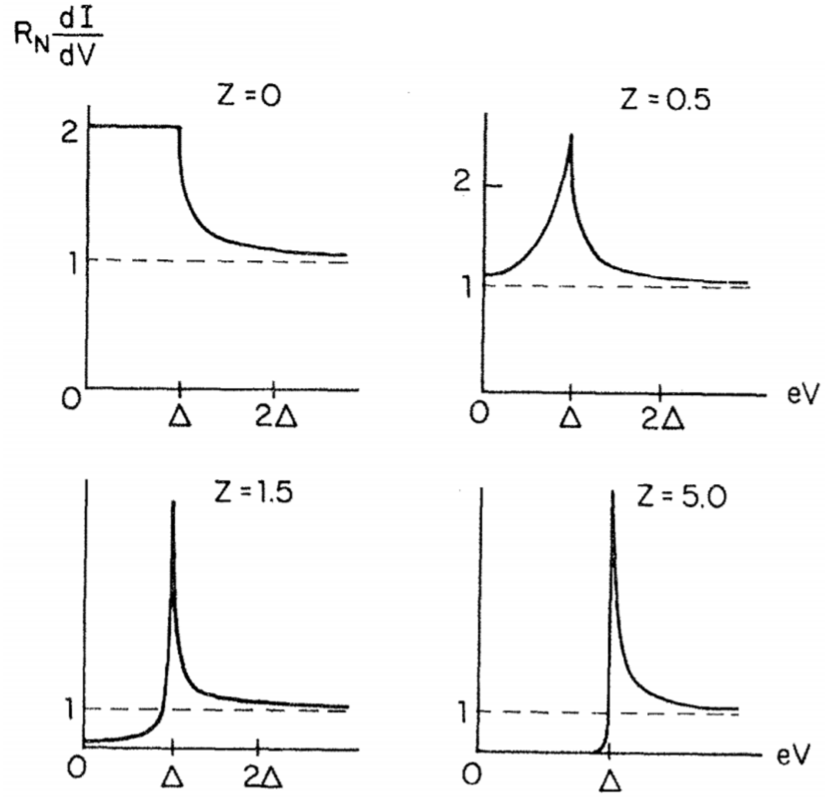

Figure 2.3. The normalized differential conductance $R_N \frac{dI}{dV}$ as a function of bias voltage for various barrier strengths Z at $T = 0$. Figure is taken from Ref. [**10**].

Although the BTK theory successfully reproduces the enhancement of conductance associated with Andreev reflection and its dependence on the barrier strength based on a simple plane-wave formalism, it should be noted that BTK theory is only valid for a system where scattering of quasiparticles in the normal metal and the superconductor can be ignored so the ballistic treatment of the wavefunction can be made, such as point contacts. However, the heterostructures experimentally investigated for this thesis consist of diffusive metals where scattering occurs due to the short mean free path l compared to the dimension of the system of interest, which makes it inadequate to directly apply BTK theory to the analysis of our experimental data. Moreover, the BTK theory only considers a single NS interface and does not provide any information on the spatial dependence of the processes under consideration. Therefore, it is not useful as a stand-alone theory to analyze our experimental results obtained from heterostructures consisting of many leads with different dimensions, which requires the introduction of a more sophisticated approach in the next section.

2.3. Quasiclassical theory of superconductivity

The quasiclassical theory of superconductivity is based on a Green's function formalism and has shown exceptional ability in providing quantitative description of many interesting transport phenomena observed in various systems. While there are a number of references that have explored the application of the quasiclassical theory of superconductivity to proximity coupled systems in a wide range of regimes [**12, 13, 14, 15, 16, 17, 18, 19**], in this section, I will briefly introduce the quasiclassical theory by mainly focusing on the diffusive regime that the samples used in the experiments fall into and its application to the systems with different geometries.

2.3.1. The Usadel equation

In the diffusive regime, often called the *dirty limit* since the mean free path l is much shorter than the size of sample, the electrons experience a series of elastic scatterings with the impurities which averages out the anisotropic components of the Green's function. Then the Green's function can be expanded only up to the first order in v_F as [**20**]

$$\check{g}(\mathbf{R}, \hat{v}_F, E) \simeq \check{g}_s(\mathbf{R}, E) + \hat{v}_F \check{g}_p(\mathbf{R}, E) \tag{2.25}$$

where $\check{g}_{s,p}$ has $\hat{g}_{s,p}^{R,A,K}$, the retarded, advanced, and Keldysh Green's functions, as components in a matrix form in Nambu-Gorkov space

$$\check{g}_{s,p} = \begin{pmatrix} \hat{g}_{s,p}^{R} & \hat{g}_{s,p}^{K} \\ 0 & \hat{g}_{s,p}^{A} \end{pmatrix}. \tag{2.26}$$

By applying the approximation made in Eq. (2.25) into the Eilenberger equation [**21**] and the relation $v_F \check{g}_s \partial \check{g}_s = -\frac{1}{\tau_{tr}} \check{g}_p$ with the scattering time τ_{tr}, we obtain the Usadel equation

$$[E\check{\tau}_3 + \check{\Delta}, \check{g}_s] - iD\hat{\partial}(\check{g}_s \hat{\partial} \check{g}_s) = 0, \tag{2.27}$$

where $D = {v_F}^2 \tau_{tr}/3 = v_F l/3$ is the diffusion constant of the material. Since the detailed procedure of derivation for the Usadel equation can be found in Ref. [**19**], here I will focus on the resulting equations. By applying the matrix form of $\check{g}_s$ as given above, we obtain three separate equations:

$$[E\hat{\tau}_3 + \hat{\Delta}, \hat{g}_s^R] = iD\partial(\hat{g}_s^R \partial \hat{g}_s^R), \tag{2.28a}$$

$$[E\hat{\tau}_3 + \hat{\Delta}, \hat{g}_s^A] = iD\partial(\hat{g}_s^A \partial \hat{g}_s^A), \tag{2.28b}$$

and

$$[E\hat{\tau}_3 + \hat{\Delta}, \hat{g}_s^K] = iD\partial[(\hat{g}_s^R \partial \hat{g}_s^K) + (\hat{g}_s^K \partial \hat{g}_s^A). \tag{2.28c}$$

While the first two equations from the diagonal components represent the equilibrium properties of the system such as the density of states $N(E)$, spectral supercurrent $Q(E)$

and so on, the third equation from the off-diagonal term component represents the non-equilibrium aspects of the system by generating equations for the distribution functions under bias voltage.

Keeping the normalization condition $\hat{g}^R\hat{g}^R = 1$ in mind[1], one can parametrize the retarded Green's function $\hat{g}^R$ as

$$\hat{g}^R = \begin{pmatrix} \cosh\theta & \sinh\theta\, e^{i\phi} \\ -\sinh\theta\, e^{-i\phi} & -\cosh\theta \end{pmatrix}, \tag{2.29}$$

where θ and ϕ are complex functions of the energy E and the position $\mathbf{R}$. Since the advanced Green's function $\hat{g}^A$ is related to $\hat{g}^R$ by the relation $\hat{g}^A = -\hat{\tau}_3(\hat{g}^{R\dagger})\hat{\tau}_3$, it is written as

$$\hat{g}^A = \begin{pmatrix} -\cosh\theta^* & -\sinh\theta^*\, e^{i\phi^*} \\ \sinh\theta^*\, e^{-i\phi^*} & \cosh\theta^* \end{pmatrix}, \tag{2.30}$$

which satisfies the normalization condition as well. Now we can express the Usadel equations in terms of θ and ϕ by inserting $\hat{g}^R$ into the matrix in Eq. (2.28a), whose (1,1) component is written as

$$D(\sinh^2\theta)\partial^2\phi + D(\sinh 2\theta)\partial\phi\partial\theta - 2i\mathbf{Im}(\Delta)\sinh\theta = 0, \tag{2.31a}$$

and off-diagonal (1,2) component is written as

$$D\partial^2\theta - \frac{D}{2}\sinh 2\theta(\partial\phi)^2 + 2Ei\sinh\theta - 2i\mathbf{Re}(\Delta)\cosh\theta = 0, \tag{2.31b}$$

[1] I will omit the subscript s for the Green's function for the rest of this chapter.

respectively. By defining a current $j_s(E,\mathbf{R}) = \sinh^2\theta(E,\mathbf{R})\partial\phi(E,\mathbf{R})$, Eq. (2.31a) is rewritten as

$$D\partial j_s(E,\mathbf{R}) - 2i\mathbf{Im}(\Delta)\mathrm{sinh}\theta = 0. \tag{2.32}$$

It should be noted that j_s is related to the conventional definition of spectral supercurrent $Q(E,\mathbf{R})$ by

$$Q(E,\mathbf{R}) = -\mathbf{Im}j_s(E,\mathbf{R}) \tag{2.33}$$

Hence, the spectral supercurrent is proportional to the square of the pair amplitude and to the gradient of phase ϕ. In a normal metal wire where $\Delta = 0$, Eq. (2.32) is reduced to $\partial j_s(E,\mathbf{R}) = 0$, which implies the conservation of the spectral supercurrent through the wire.

In order to solve the differential equations, the application of proper boundary conditions is critical. General boundary conditions for the Green's functions at the inteface have been derived by Zaitsev [**22**] for arbitrary transparency of the interface and simplified by Kupriyanov and Lukichev [**23**] in the limit of small value of the transparency. With the subscripts standing for different materials meeting at the interface, the boundary condition for the Green's functions are written as

$$v_{F1}D_1\hat{g}_1(\partial\hat{g}_1) = v_{F2}D_2\hat{g}_2(\partial\hat{g}_2) \tag{2.34a}$$

$$\hat{g}_1\partial\hat{g}_1 = \frac{1}{2r}[\hat{g}_1,\hat{g}_2] \tag{2.34b}$$

where $r = R_b/R_N$ is the ratio of the barrier (interface) resistance R_b to the resistance of the normal metal wire per length R_N. While the first equation involves the diffusion coefficient and the derivative of the Green's function implying the conservation of the current across the interface, the second equation contains the first order term in terms of $1/r$, thus it is only valid for low values of $1/r$.

By inserting the parametrized form of the Green's functions, the boundary conditions of Kupriyanov and Lukichev is expressed in terms of θ and ϕ as

$$r\,\sinh\theta_1(\partial\phi_1) = \sinh\theta_2 \sin(\phi_2 - \phi_1) \tag{2.35a}$$

$$r\left[\partial\theta_1 + i\sinh\theta_1\cosh\theta_1(\partial\phi_1)\right] = \cosh\theta_1 \sinh\theta_2 e^{i(\phi_2-\phi_1)} - \sinh\theta_1\cosh\theta_2 \tag{2.35b}$$

For the case of a perfect interface with $r = 0$, the boundary conditions are reduced to the continuity of the functions at the interface, i.e., $\theta_1 = \theta_2$ and $\phi_1 = \phi_2$, and the conservation of the currents, i.e., $A_1\partial\theta_1 + A_2\partial\theta_2 = 0$ and $A_1\partial\phi_1 + A_2\partial\phi_2 = 0$, analogous to the Kirchoff's law where A_i $(i = 1, 2)$ is the cross-sectional area of the i-th wire at the node. If n wires meet at a single node, the conditions are generalized to $\theta_1 = \theta_2 = \cdots = \theta_n$ and $\phi_1 = \phi_2 = \cdots = \phi_n$, and $\sum_{i=1}^{n} A_i\partial\theta_i = 0$ and $\sum_{i=1}^{n} A_i\partial\phi_i = 0$, respectively.

The retarded Green's function $\hat{g}^R$ for a bulk superconductor in equilibrium can be found by solving Eq. (2.28a) with $\partial\hat{g}^R = 0$ and by applying the normalization condition, which leads to

$$\hat{g}^R = \begin{pmatrix} \frac{E}{\sqrt{E^2-|\Delta|^2}} & \frac{\Delta}{\sqrt{E^2-|\Delta|^2}} \\ -\frac{\Delta^*}{\sqrt{E^2-|\Delta|^2}} & -\frac{E}{\sqrt{E^2-|\Delta|^2}} \end{pmatrix}. \tag{2.36}$$

With the parametrization introduced earlier, it is straightforward to obtain

$$\cosh\theta_0 = \frac{E}{\sqrt{E^2 - |\Delta|^2}}, \tag{2.37}$$

which can be written for θ as

$$\theta_0 = \begin{cases} -\frac{\pi}{2}i + \frac{1}{2}\ln\frac{\Delta+E}{\Delta-E} & \text{if } E < \Delta \\ \frac{1}{2}\ln\frac{E+\Delta}{E-\Delta} & \text{if } E > \Delta \end{cases} . \tag{2.38}$$

For a normal metal, as $\Delta = 0$, the retarded Green's function is reduced to $\hat{g}^R = \hat{\tau}_3$ leading to $\theta_0 = 0$.

The parametrization of Green's function shown in Eq. (2.29) is not the only way of parametrization for numerical calculations. For example, in Ref. [**24**] cosine and sine functions are used to parametrize the retarded Green's function g^R instead of hyperbolic cosine and hyperbolic sine whose relation is derived as the following. By substituting θ in Eq. (2.29) with $\theta = i\xi$, the retarded Green's function $\hat{g}^R$ is expressed as

$$\begin{aligned} \hat{g}^R &= \begin{pmatrix} \cos\xi & i\sin\xi\, e^{i\phi} \\ -i\sin\xi\, e^{-i\phi} & -\cos\xi \end{pmatrix} \\ &= \begin{pmatrix} \cos\xi & \sin\xi\, e^{i(\chi+\pi/2)} \\ \sin\xi\, e^{-i(\chi+\pi/2)} & -\cos\xi \end{pmatrix} \end{aligned} \tag{2.39}$$

where ϕ is now replaced by $\chi + \pi/2$. Then the Usadel equations are expressed in terms of ξ and χ as

$$(\sin^2\xi)\partial^2\chi + (\sin 2\xi)\partial\chi\partial\xi = 0 \tag{2.40a}$$

and

$$D\partial^2\xi - \frac{D}{2}\sin\xi(\partial\chi)^2 + 2Ei\sin\xi = 0 \tag{2.40b}$$

in a normal metal wire where $\Delta = 0$.

In addition to (θ, ϕ) parametrization and (ξ, χ) parametrization, there is another way of parametrization called Ricatti parametrization. Further details of the parametrization and the application can be found in recent theoretical works [**25, 26, 27**].

2.3.2. The kinetic equation

While the solution of the Usadel equation provides spectral information of the system which describes the equilibrium properties of the system as a function of energy, nonequilibrium properties can be obtained by solving another set of equations, Eq. (2.28c), and extracting the distribution functions of the system. From the normalization condition of $\check{g}$, the Keldysh Green's function $\hat{g}^K$ can be written as

$$\hat{g}^K = \hat{g}^R \hat{h} - \hat{h} \hat{g}^A \tag{2.41}$$

where $\hat{h}$ is called distribution matrix. Then Eq. (2.28c) is expressed as

$$\partial[\partial \hat{h} + \hat{g}^R(\partial \hat{g}^R)\hat{h} - \hat{h}\hat{g}^A(\partial \hat{g}^A) - \hat{g}^R(\partial \hat{h})\hat{g}^A] = 0, \tag{2.42}$$

with $\Delta = 0$ for a normal metal wire. Now the distribution matrix $\hat{h}$ is decomposed into two components as

$$\hat{h} = h_L \hat{\tau}_0 + h_T \hat{\tau}_3, \tag{2.43}$$

where h_L and h_T are called longitudinal and transverse components respectively. By inserting Eq. (2.43), Eq. (2.42) can be expanded in terms of h_L and h_T as

$$\begin{aligned}&\partial[(\hat{g}^R\partial\hat{g}^R - \hat{g}^A\partial\hat{g}^A)h_L + (1-\hat{g}^R\hat{g}^A)\partial h_L]\hat{\tau}_0 + \\ &\partial[(\hat{g}^R\partial\hat{g}^R - \hat{\tau}_3\hat{g}^A\partial\hat{g}^A\hat{\tau}_3)h_T + (1-\hat{g}^R\hat{\tau}_3\hat{g}^A\hat{\tau}_3)\partial h_T]\hat{\tau}_3 = 0.\end{aligned} \tag{2.44}$$

Two separate equations can be obtained i) by multiplying the equation by $\hat{\tau}_3$ and taking the trace and ii) by multiplying the equation by $\hat{\tau}_0$ and taking the trace. With the following definitions of Q and M_{ij},

$$Q = \frac{1}{4}\mathrm{Tr}[(\hat{g}^R\partial\hat{g}^R - \hat{g}^A\partial\hat{g}^A)\hat{\tau}_3] \tag{2.45}$$

and

$$M_{ij} = \frac{1}{4}\mathrm{Tr}[\delta_{ij} - \hat{g}^R\hat{\tau}_i\hat{g}^A\hat{\tau}_j], \tag{2.46}$$

i) and ii) result in

$$\partial[M_{33}\partial h_T + Q h_L + M_{03}\partial h_L] = 0, \tag{2.47a}$$

$$\partial[M_{00}\partial h_L + Q h_T + M_{30}\partial h_T] = 0 \tag{2.47b}$$

respectively. It should be mentioned that if a finite superconducting gap Δ is considered, a more general result can be obtained [**19**]:

(2.48a)
$$\partial[M_{33}\partial h_T + Qh_L + M_{03}\partial h_L] = \frac{i}{4D}[h_L \mathrm{Tr}\{\tau_3[\hat{g}_s^R - \hat{g}_s^A, \hat{\Delta}\} - 2h_T \mathrm{Tr}\{\hat{\Delta}(\hat{g}_s^R + \hat{g}_s^A)\}]],$$

(2.48b)
$$\partial[M_{00}\partial h_L + Qh_T + M_{30}\partial h_T] = 0$$

Here $Q(E, \mathbf{R})$ corresponds to the spectral supercurrent introduced in the previous section and the M_{ij}, multiplied by D, acts as diffusion coefficients that are dependent on the energy and position. Based on the parametrization shown in Eq. (2.29), M_{00}, M_{33}, and M_{03} are expressed in θ and ϕ as

(2.49a)
$$Q = -\mathbf{Im}(\sinh^2\theta\partial\phi),$$

(2.49b)
$$M_{00} = \frac{1}{2}[1 + \cosh\theta\cosh\theta^* - \sinh\theta\sinh\theta^*\cosh(2\mathbf{Im}(\phi))],$$

(2.49c)
$$M_{33} = \frac{1}{2}[1 + \cosh\theta\cosh\theta^* + \sinh\theta\sinh\theta^*\cosh(2\mathbf{Im}(\phi))],$$

and

(2.49d)
$$M_{03} = \frac{1}{2}\sinh\theta\sinh\theta^*\sinh(2\mathbf{Im}(\phi)) = -M_{30},$$

and in ξ and χ based on the parametrization shown in Eq. (2.40),

(2.50a)
$$Q = -\mathbf{Im}(\sin^2\xi\partial\chi),$$

(2.50b)
$$M_{00} = \frac{1}{2}[1 + \cos\xi\cos\xi^* - \sin\xi\sin\xi^*\cos(2\mathbf{Im}(\chi))],$$

(2.50c)
$$M_{33} = \frac{1}{2}[1 + \cos\xi\cos\xi^* + \sin\xi\sin\xi^*\cos(2\mathbf{Im}(\chi))],$$

and

$$M_{03} = \frac{1}{2}\sin\xi\sin\xi^{*}\sin(2\mathbf{Im}(\chi)) = -M_{30}. \tag{2.50d}$$

Therefore, before solving the kinetic equation, the following steps should be performed: i) solve the Usadel equation, ii) construct Q, M_{00}, M_{33}, and M_{03} using the solutions in a given parametrization, and iii) set up the kinetic equations accordingly.

In order to solve the kinetic equation, proper boundary conditions should be imposed. If n-wires meet at a single node, the continuity of the distribution function states that $h_{T,1} = h_{T,2} = \cdots = h_{T,n}$ and $h_{L,1} = h_{L,2} = \cdots = h_{L,n}$ at the node, where $h_{T,i}$ and $h_{L,i}$ are the distribution functions h_T and h_L evaluated in the i-th wire. In addition, the conservation law of currents, analogous to the Kirchoff's law, requires the conservation of both the charge current $j(E, \mathbf{R}, T)$ and the thermal current $j_{th}(E, \mathbf{R}, T)$ at energy E as $\sum_{i=1}^{n} A_i\, j(E, \mathbf{R}, T)_i = 0$ and $\sum_{i=1}^{n} A_i\, j_{th}(E, \mathbf{R}, T)_i = 0$ where A_i is the cross-sectional area of the i-th wire at the node. Here, $j(E, \mathbf{R}, T)_i$ and $j_{th}(E, \mathbf{R}, T)_i$ are the spectral charge current and the thermal current evaluated in the i-th wire, respectively, where the charge current $j(\mathbf{R}, T)$ and the thermal current $j_{th}(\mathbf{R}, T)$ are expressed in terms of the solution of Eq. (2.28) as

$$j(\mathbf{R}, T) = \int dE\, j(E, \mathbf{R}, T) = \frac{eN(0)D}{4} \int dE \mathrm{Tr}[\hat{\tau}_3(\hat{g}^R \partial \hat{g}^K + \hat{g}^K \partial \hat{g}^A)] \tag{2.51}$$

$$j_{th}(\mathbf{R}, T) = \int dE\, j_{th}(E, \mathbf{R}, T) = \frac{N(0)D}{4} \int dE\, E\, \mathrm{Tr}[\hat{\tau}_3(\hat{g}^R \partial \hat{g}^K + \hat{g}^K \partial \hat{g}^A)] \tag{2.52}$$

which can be written in terms of h_T and h_L as

$$j(\mathbf{R},T) = eN(0)D\int dE[M_{33}\partial h_T + Qh_L + M_{03}\partial h_L] \tag{2.53}$$

$$j_{th}(\mathbf{R},T) = N(0)D\int dE\,E\,[M_{33}\partial h_L + Qh_T + M_{30}\partial h_T]. \tag{2.54}$$

Since thermal effects are out of the scope of this thesis, I will focus only on the charge current. The first term in Eq. (2.51) represents the quasiparticle (or dissipative) current, and the second term is the supercurrent with spectral density Q. The third term is associated with an imbalance between electrons and holes, which is proportional to the derivative of h_L. In the limit where no superconductivity is involved, $\hat{g}^R = \hat{\tau}_3$, $\hat{g}^R = \hat{\tau}_3$, and $\hat{\Delta} = 0$, which leads to $M_{00} = M_{33} = 1$, and $Q = M_{03} = M_{30} = 0$.

The equilibrium distribution functions h_L and h_T at a reservoir at a temperature T with a voltage V applied are given by

$$h_{L,T} = \frac{1}{2}\left[\tanh\left(\frac{E+eV}{2k_BT}\right) \pm \tanh\left(\frac{E-eV}{2k_BT}\right)\right]. \tag{2.55}$$

For the case of a superconducting reservoir, we consider only the case $V = 0$, $h_L = \tanh\left(\frac{E}{2k_BT}\right) = 1 - 2f_0$ where $f_0 = \left[\exp\left(\frac{E}{k_BT}\right) + 1\right]^{-1}$ is the equilibrium Fermi distribution and $h_T = 0$.

2.4. Numerical simulation based on the quasiclassical theory

So far, I have briefly introduced the derivation of the Usadel equation and the kinetic equation in the diffusive regime based on the quasiclassical theory. In this section, I will explain the important steps of the numerical recipe to apply the equations into the system of our interest while the detailed description of the numerical recipe will be given in Appendix A. In particular, I explain how to treat a geometry including wires with different lengths.

2.4.1. Normalization of the equations

In order to implement the equations for numerical calculation, one needs to put them into a dimensionless form. Let us attempt to solve the Usadel equations Eq. (2.31a) and Eq. (2.31b) for a wire of length L_0. Since the equations are in the unit of energy, they should be normalized by an energy scale. A natural choice for such an energy is the Thouless energy of the wire, i.e., $E_T = \hbar D/{L_0}^2$. Then Eqs. (2.31a) and (2.31b) are rewritten as

$$(\sinh^2\theta)\frac{\partial^2\phi}{\partial x'^2} + (\sinh 2\theta)\frac{\partial\phi}{\partial x'}\frac{\partial\theta}{\partial x'} - 2i\mathbf{Im}\left(\frac{\Delta}{E_T}\right)\sinh\theta = 0, \tag{2.56a}$$

and

$$\frac{\partial^2\theta}{\partial x'^2} - \frac{1}{2}\sinh 2\theta\left(\frac{\partial\phi}{\partial x'}\right)^2 + 2\left(\frac{E}{E_T}\right)i\sinh\theta - 2i\mathbf{Re}\left(\frac{\Delta}{E_T}\right)\cosh\theta = 0. \tag{2.56b}$$

For the normal metal wire, the equations are reduced due to $\Delta = 0$. Here $\frac{\partial}{\partial x'}$ is a dimensionless spatial derivative with the normalized coordinate $x' = x/L_0$ running from 0 to 1. It should be noted that energy E and the gap Δ considered in the numerical calculation are normalized with respect to E_T. By defining $\frac{\partial\theta}{\partial x'} = \theta'$ and $\frac{\partial\phi}{\partial x'} = \phi'$, two second order differential equations written above are split into four first order differential equations as

$$
\begin{aligned}
&\frac{\partial \theta}{\partial x'} = \theta' \\
&\frac{\partial \phi}{\partial x'} = \phi' \\
&\sinh^2\theta \phi'^2 + \sinh 2\theta \phi' \theta' = 0 \\
&\theta'^2 - \frac{1}{2}\sinh 2\theta \phi'^2 + 2\left(\frac{E}{E_T}\right) i \sinh\theta = 0.
\end{aligned}
\tag{2.57}
$$

If there are m mesh points along the coordinate of the wire between 0 and 1, the derivative $\frac{\partial f}{\partial x'}$ of an arbitrary function f at the $k-$th mesh point x_k can be numerically calculated by $\frac{\partial f}{\partial x'} = \frac{f(x_k)-f(x_{k-1})}{h}$, where $h = 1/m$. Therefore, the equation can be rewritten in the form for the numerical calculation as

$$
\begin{aligned}
&\theta(x_k) - \theta(x_{k-1}) = h\,\theta'(x_k) = \frac{h}{2}\left[\theta'(x_k) + \theta'(x_{k-1})\right] \\
&\theta(x_k) - \phi(x_{k-1}) = h\,\phi'(x_k) = \frac{h}{2}\left[\phi'(x_k) + \phi'(x_{k-1})\right] \\
&(\sinh\theta(x_k))^2(\phi'(x_k))^2 + \sinh(2\theta(x_k))\phi'(x_k)\theta'(x_k) = 0 \\
&(\theta'(x_k))^2 - \frac{1}{2}\sinh(2\theta(x_k))(\phi'(x_k))^2 + 2\left(\frac{E}{E_T}\right) i \sinh\theta(x_k) = 0.
\end{aligned}
\tag{2.58}
$$

By applying adequate boundary conditions introduced in the previous section, one can find the solution vector $(\theta, \phi, \theta', \phi')$ for all x_k along the coordinate of the wire running from 0 to 1.

However, if we consider a geometry which consists of multiple wires with different lengths, care should be taken for solving the equations numerically. If the i-th wire has a length L_i, the Usadel equations for the wire should be normalized by the Thouless energy of the wire

$E_{T_i} = \hbar D/L_i^2$ as as

$$(\sinh^2\theta)\frac{\partial^2\phi}{\partial x_i'^2} + (\sinh 2\theta)\frac{\partial\phi}{\partial x_i'}\frac{\partial\theta}{\partial x_i'} = 0 \tag{2.59a}$$

and

$$\left[\frac{\partial^2\theta_i}{\partial x_i'^2} - \frac{1}{2}\sinh 2\theta_i\left(\frac{\partial\phi_i}{\partial x_i'}\right)^2\right] + 2\left(\frac{E}{E_{T_i}}\right) i\sinh\theta_i = 0 \tag{2.59b}$$

where θ_i and ϕ_i are θ and ϕ of the i-th wire, and $\frac{\partial}{\partial x_i'}$ is a dimensionless spatial derivative with the normalized coordinate $x' = x_i/L_i$ running from 0 to 1. This is in the same form as Eq. (2.56b) except the energy is normalized by E_{T_i}. Since we should solve the Usadel equation for a specific energy E for different wires included in the geometry, we should *a priori* choose a wire whose length L_0 defines the Thouless energy $E_{T_0} = \hbar D/L_0^2$ to scale the energy. The equations are then written as

$$(\sinh^2\theta)\frac{\partial^2\phi}{\partial x_i'^2} + (\sinh 2\theta)\frac{\partial\phi}{\partial x_i'}\frac{\partial\theta}{\partial x_i'} = 0 \tag{2.60a}$$

and

$$\left[\frac{\partial^2\theta_i}{\partial x_i'^2} - \frac{1}{2}\sinh 2\theta_i\left(\frac{\partial\phi_i}{\partial x_i'}\right)^2\right] + 2\left(\alpha_i^2\frac{E}{E_{T_0}}\right) i\sinh\theta_i = 0 \tag{2.60b}$$

where α_i is the relative length of L_i with respect to L_0, $\alpha_i = L_i/L_0$. Therefore, for a specific energy E, the factor α_i should be included in the equation to properly take into account the different lengths L_i of the wires. In addition, one should be careful when applying the boundary conditions. As introduced in the previous section, at a node where multiple normal metal wires meet, the Kirchoff type law should be applied as $\Sigma_i\partial\theta_i = \Sigma_i\frac{\Delta\theta_i}{\Delta x_i} = \Sigma_i\frac{\Delta\theta_i}{L_i\Delta x'} = 0$, which leads to

$$\sum_i \frac{1}{\alpha_i}\frac{\partial\theta_i}{\partial x'} = 0 \tag{2.61}$$

in normalized coordinates. It should be noted that the derivative should be multiplied by an additional factor $\frac{1}{\alpha_i} = \frac{L_0}{L_i}$ in the numerical calculation. As an example, let us consider a simple system which consists of two wires each connected to a normal metal reservoir at $x = -L_1$ and a superconducting reservoir at $x = L_2$, respectively, and meet at a node at $x = 0$. The solution of the Usadel equation at a specific energy is shown in Figure 2.4 (a) for different lengths of the wire connected to the normal reservoir with $L_1/L_2 = 1, 2,$ and 3. The solutions not only show the continuity of the real and imaginary part of θ and θ' at the node, they match perfectly to one another for the same energy $E = 8E_T$ where E_T is the Thoughless energy of the entire wire with length $L_1 + L_2$, which demonstrates that the scaling of different lengths is properly treated. On the contrary, Figure 2.4 (b) shows the solutions of the Usadel equation where the factor α_i is not taken into account, which results in different solutions for the same energy value.

Similarly, in order to solve the kinetic equations Eq. (2.47a)and Eq. (2.47b) for a wire of length L_0, the equations should be normalized as

$$\frac{\partial}{\partial x'}\left[M_{33}\frac{\partial h_T}{\partial x'} + Q' h_L + M_{03}\frac{\partial h_L}{\partial x'}\right] = 0 \tag{2.62a}$$

and

$$\frac{\partial}{\partial x'}\left[M_{00}\frac{\partial h_T}{\partial x'} + Q' h_T + M_{03}\frac{\partial h_L}{\partial x'}\right] = 0. \tag{2.62b}$$

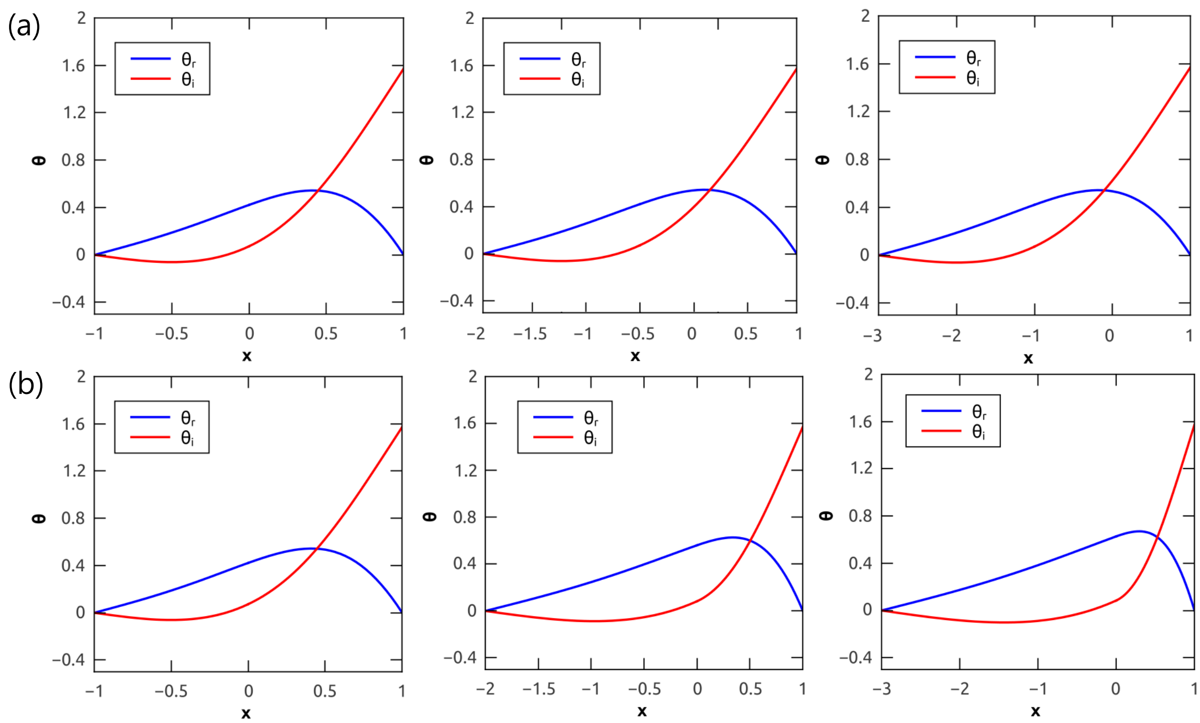

Figure 2.4. (a) The solution of the Usadel equations written in Eq. (2.59) and Eq. (2.59b) with the boundary condition given in Eq. (2.61). Real (blue) and imaginary (red) part of θ are shown for different lengths L_1, 1.0 (left), 2.0 (middle), and 3.0 (right) of the wire connected to the normal reservoir with respect to the length of the wire L_2 connected to the superconducting reservoir. The node is at $x = 0$ and the coordinate for two wires runs to negative and positive direction, respectively. $\Delta = 1000E_T$ and $E = 8E_T$ in the calculation where E_T is the Thouless energy of the entire wire with length $L_1 + L_2$. (b) The solutions of the Usadel equation where the factor α_i is not taken into account are shown for comparison.

where the normalized coordinate $x' = x/L_0$ runs from 0 to 1. Here, as the expression for the spectral supercurrent Q in Eq. (2.49a) involves the gradient of the phase, Q is written as $Q = Q'/L_0$ from the relation $\partial\phi = \frac{\partial\phi}{\partial x} = \frac{\partial\phi}{L_0 \partial x'}$ where Q' is evaluated in the normalized coordinate x'. Therefore, for the case including multiple wires with different lengths, L_i for the i-th wire, the normalized equations should be solved for each wire as

$$\frac{\partial}{\partial x_i'}\left[M_{33,i}\frac{\partial h_{T,i}}{\partial x_i'} + Q_i' h_{L,i} + M_{03,i}\frac{\partial h_{L,i}}{\partial x_i'}\right] = 0 \tag{2.63a}$$

and

$$\frac{\partial}{\partial x_i'}\left[M_{00,i}\frac{\partial h_{L,i}}{\partial x_i'} + Q_i' h_{T,i} + M_{30,i}\frac{\partial h_{L,i}}{\partial x_i'}\right] = 0, \tag{2.63b}$$

where $h_{T,i}$, $h_{L,i}$, and Q_i are the distribution functions h_T, h_L, and Q evaluated in i-th wire and the normalized coordinate $x' = x/L_i$ runs from 0 to 1 for each wire. It should be noted that the kinetic equations for all the wires are normalized to essentially the same equation in contrast to the Usadel equations. However, the boundary conditions take into account the relative lengths of the wires. At the node where multiple normal metal wires meet, the Kirchoff type boundary condition requires the conservation of the charge current

$$\sum_i M_{33,i}\partial h_{T,i} + Q_i h_{L,i} + M_{03,i}\partial h_{L,i} = 0 \tag{2.64a}$$

and the thermal current

$$\sum_i M_{00,i}\partial h_{L,i} + Q_i h_{T,i} + M_{30,i}\partial h_{T,i} = 0, \tag{2.64b}$$

which leads to the following boundary conditions in the normalized coordinates

$$\sum_i \frac{1}{\alpha_i}\left[M_{33,i}\frac{\partial h_{T,i}}{\partial x'} + Q_i' h_{L,i} + M_{03,i}\frac{\partial h_{L,i}}{\partial x'}\right] = 0, \tag{2.65a}$$

$$\sum_i \frac{1}{\alpha_i}\left[M_{00,i}\frac{\partial h_{L,i}}{\partial x'} + Q_i' h_{T,i} + M_{30,i}\frac{\partial h_{T,i}}{\partial x'}\right] = 0, \tag{2.65b}$$

where α_i is the relative length of L_i with respect to a chosen length L_0, $\alpha_i = L_i/L_0$, as introduced before.

2.4.2. Application to proximity-coupled systems

Having discussed how to implement the equations for numerical calculation, we are ready to solve the Usadel equation and kinetic equation for a specific geometry to calculate meaningful physical quantities. As the first example, I will consider a single normal metal wire connected to a superconducting reservoir on one end and to a normal metal reservoir on the other end. Despite the simplicity of the geometry, it reveals many interesting phenomena arising due to the proximity effect of superconductivity. The geometry used in the numerical calculation is shown in Figure 2.5 where the superconducting reservoir is at $x = 0$ and the normal metal reservoir is at $x = L$. In this case, the supercurrent $j_s = 0$ through the wire and Δ are set to be 0 at the normal metal reservoir and in the normal metal wire. Since ϕ does not play any role here, it can be set to 0 without loss of generality. Then only M_{00} and M_{33} are non-zero, which reduces Eq. (2.47a) and Eq. (2.47b) to $\partial(M_{33}\partial h_T) = 0$ and $\partial(M_{00}\partial h_L) = 0$. By following the approach given in Ref. [**19**], we integrate the first equation to obtain

$$h_T(x = L) - h_T(x = 0) = C\left[\int_0^L \frac{1}{M_{33}(E, x)}dx\right] \tag{2.66}$$

where C is a constant that arises from integration. In the limit of a small voltage V applied to the normal metal reservoir, the left hand side of the above equation is expanded as

$$\begin{aligned} h_T(x = L) - h_T(x = 0) &= \frac{1}{2}\left[\tanh\left(\frac{E + 2V}{2k_BT}\right) - \tanh\left(\frac{E - 2V}{2k_BT}\right)\right] \\ &\simeq \frac{eV}{2k_BT\cosh^2(E/2k_BT)} \end{aligned} \tag{2.67}$$

which leads to $C = M_{33}\partial h_T = \frac{eV}{2k_BT\cosh^2(E/2k_BT)}\left[\int_0^L \frac{1}{M_{33}(E,x)}dx\right]^{-1}$. Therefore, the conductance of the system can be expressed by using the Eq. (2.54) as

$$G = \int dE \frac{G(E)}{2k_BT\cosh^2(E/2k_BT)} \tag{2.68}$$

where $G(E)$ is given as

$$G(E) = G_N\left[\int_0^L \frac{1}{M_{33}(E,x)}dx\right]^{-1}. \tag{2.69}$$

In short, in the small bias regime, the conductance of a normal metal wire between two reservoirs can be calculated by integrating the spectral conductance $G(E)$ which is obtained by solving the Usadel equations, with a proper temperature-dependent weight.

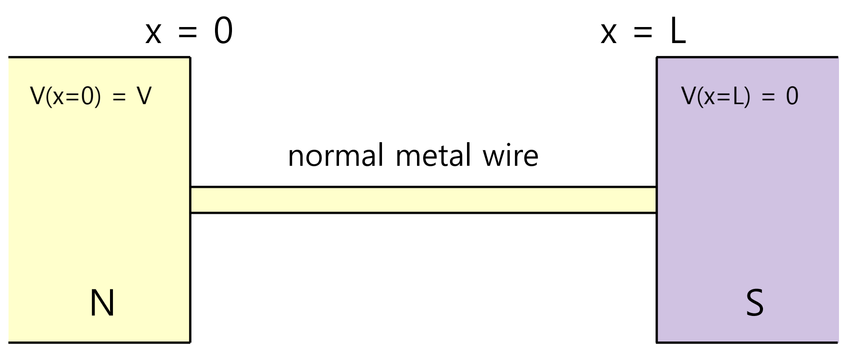

Figure 2.5. Single wire between a normal reservoir N (positioned at $x = 0$) and a superconducting reservoir S (positioned at $x = L$). The voltage V is applied to N.

The result is shown in Figure 2.6 where the resistance of the normal metal wire decreases as a function of temperature due to the proximity effect from the superconducting reservoir before reaching a minimum at $T \simeq 5E_T$, where E_T is the Thouless energy of the normal metal wire. The result has been obtained by assuming a perfectly transparent interface. According to the result of the calculation presented in Ref. [**19**], the temperature at which the

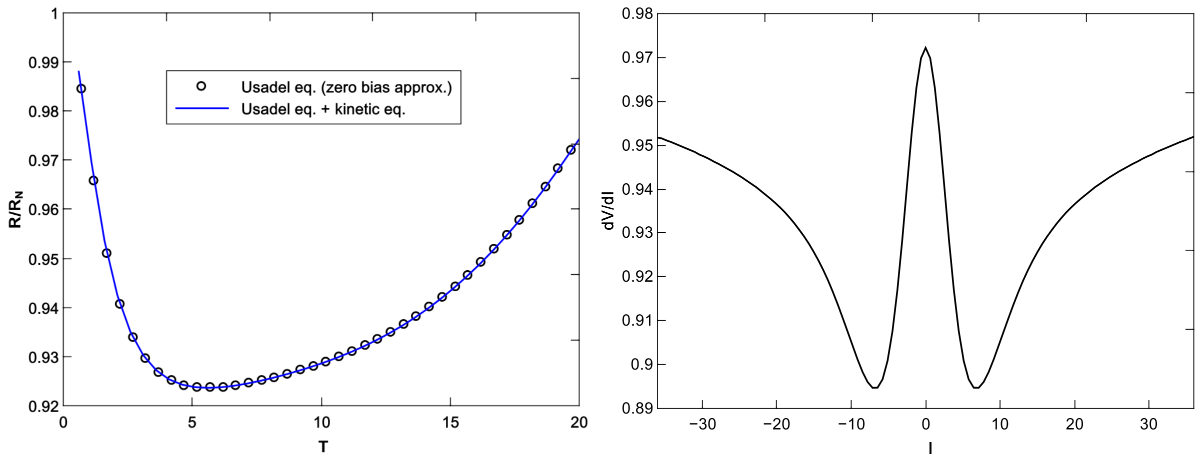

Figure 2.6. Left: Temperature dependence of the calculated resistance of a normal metal wire between a superconducting reservoir and a normal metal reservoir: The result obtained by solving the Usadel equation (black open circle) and by solving both the Usadel equation and the kinetic equation (blue solid line) with applied voltage $eV = 0.01\ E_T$. Right: dV/dI as a function of current at $T = E_T$. The gap is set to $\Delta = 1000\ E_T$, and the barrier resistance is $r = 0$.

minimum appears is lowered below $5E_T$ as the barrier resistance r increases. As temperature is further decreased, the resistance starts to increase and recovers its normal value R_N at $T = 0$. This phenomena is called the *reentrance effect* and it happens due to the proximity-induced opening of the gap in the density of the states which then increases the resistance of the normal metal wire. The topic has been studied extensively in the last decades both theoretically [**28, 29, 30, 31, 32**] and experimentally [**33, 34, 35**].

The bias dependence of the differential conductance (or resistance) can be investigated by solving the kinetic equation with different values of voltage bias. For each value of the voltage V, the distribution functions h_T and h_L are obtained and the current $j(\mathbf{R}, T)$ is calculated by using Eq. (2.54). Since $Q = 0$ and $M_{03} = 0$, only quasiparticle current flows through the normal metal wire. The right panel in Figure (2.6) shows the differential resistance $\frac{dV}{dI}$ as

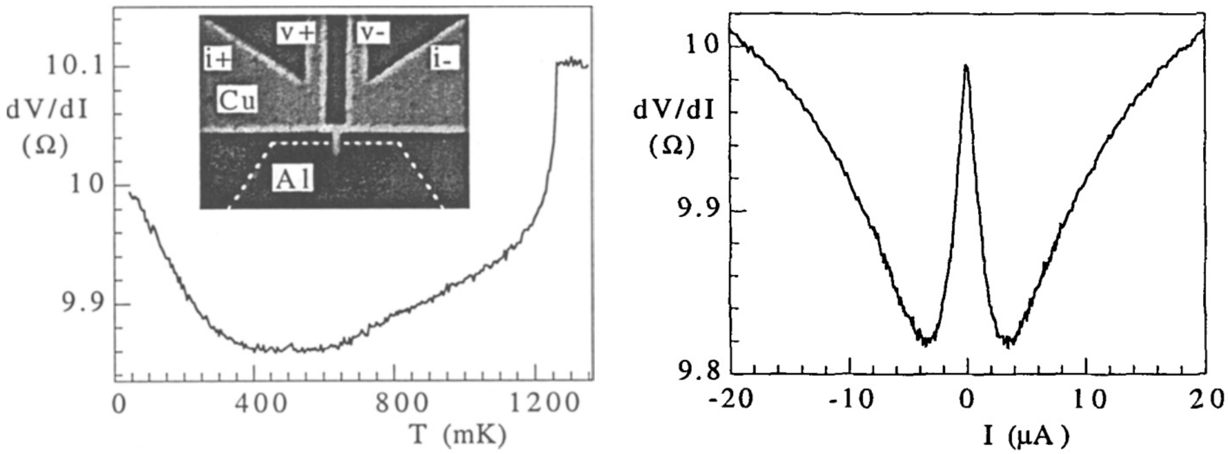

Figure 2.7. Left: Temperature dependence of the resistance. The measurement configuration is denoted in the inset with the image of the sample. Right: Bias current dependence of the differential resistance at $T = 50$ mK. Figures taken from Ref.[**35**].

a function of bias current, which is obtained by differentiating the applied voltage V with respect to the calculated current I. A large peak appears near zero bias which is consistent with the experimental result in the work by Charlat [**35**] shown in the right panel of Figure 2.7. In the small bias regime, $V \simeq 0$, the calculated resistance is in perfect agreement with the resistance obtained by only using the solution of the Usadel equation, as shown in the left panel in Figure 2.6.

As the next geometry, let us consider a normal metal wire between two superconducting reservoirs as shown in Figure 2.8. This so called proximity-coupled normal metal reveals a gap referred to as the *minigap* in the density of states (DOS), which was theoretically predicted [**36, 37, 38, 39, 40**] and experimentally probed [**41**]. According to these studies, the magnitude of the minigap is constant along the normal metal wire and is varied by the phase difference $\Delta\phi$ between the two superconductors. Figure 2.9 shows the result of our numerical calculation of the normalized DOS, $N(E)/N(0)$ ($N(0)$: DOS at the Fermi surface),

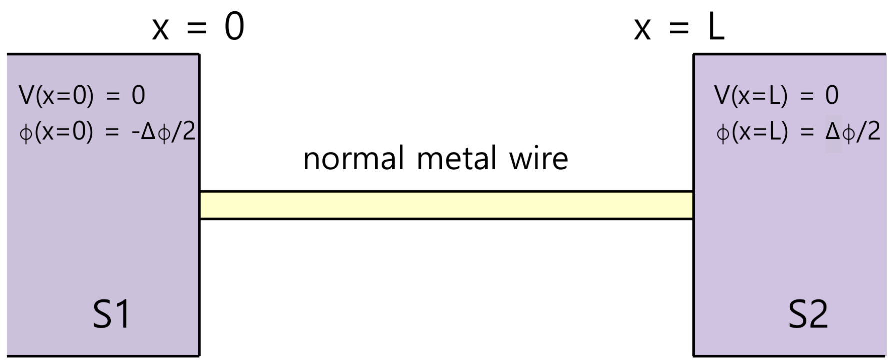

Figure 2.8. Single normal metal wire between two superconducting reservoirs S1 (positioned at $x = 0$) and S2 (positioned at $x = L$). There is a phase difference $\Delta\phi$ between two reservoirs.

by solving the Usadel equation for $\phi = 0$. For this calculation, the superconducting gap is set to $\Delta = 1000\ E_T$ with E_T being the Thouless energy of the proximity-coupled normal metal wire, which corresponds to $\Delta \gg E_T$, falling into the regime of the *long junction limit*. As all the samples experimentally studied for this thesis are in the long junction limit, I will only consider the case $\Delta \gg E_T$ throughout this chapter. The result exhibits a constant minigap δ with magnitude $\delta \simeq 3.1\ E_T$ in the normal metal wire, which is consistent with the theoretical result obtained earlier for the long junction limit [**40**].

Another interesting feature of the proximity-coupled normal metal is that it is capable of carrying a finite amount of supercurrent. As we only consider the case where the voltage applied to the superconductors is $V = 0$, the spatial derivatives of both h_T and h_L, ∂h_T and ∂h_L, are zero. Then the charge current $j(\mathbf{R}, T)$ in Eq. (2.54) is simplified to

$$j(\mathbf{R}, T) = eN(0)D \int dE\, Q(E)\, h_L(E) \tag{2.70}$$

where h_L is independent of position and is given by $h_L(E) = \tanh(E/2k_BT)$. The spectral supercurrent $Q(E)$ along the normal metal wire is shown in Figure 2.10 for different values

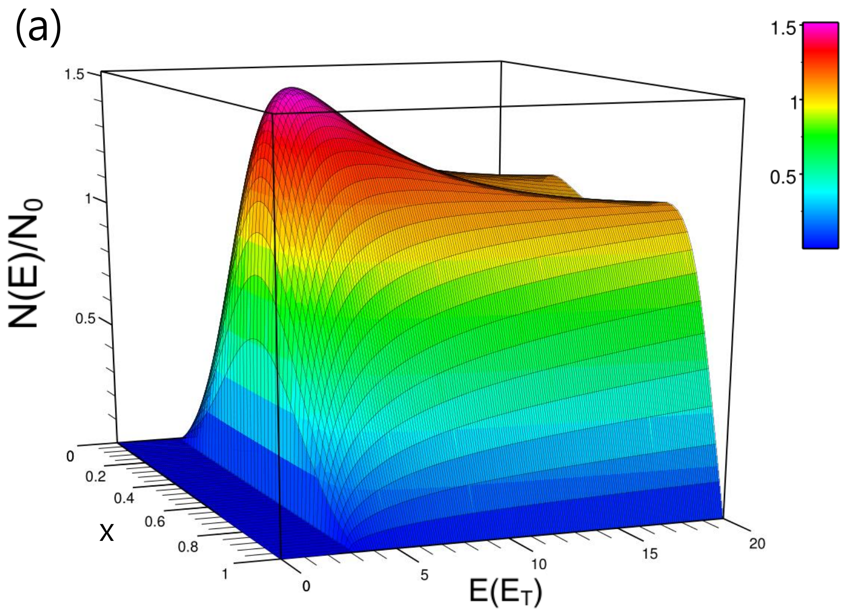

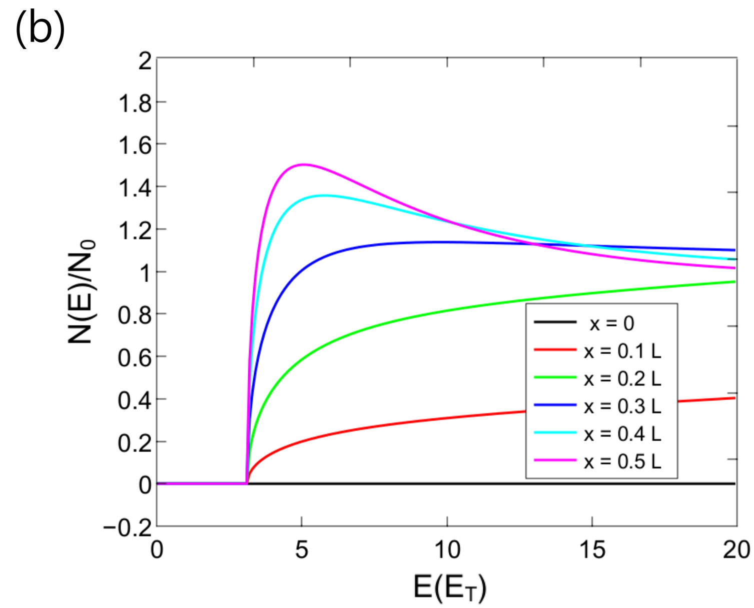

Figure 2.9. (a) Normalized DOS $N(E)/N(0)$ in the normal metal wire presented in Figure 2.8 as a function of position x and energy E. $\Delta = 1000\ E_T$ and $\phi = 0$ for the calculation. (b) Normalized DOS as a function of energy at various positions.

of phase $\phi = \pi/8, \pi/4$ and $\pi/2$ between two superconducting reservoirs. In the limit of low temperature, as $T \to 0$ ($h_L(E) \to 1$), the supercurrent I_s can be calculated by simply

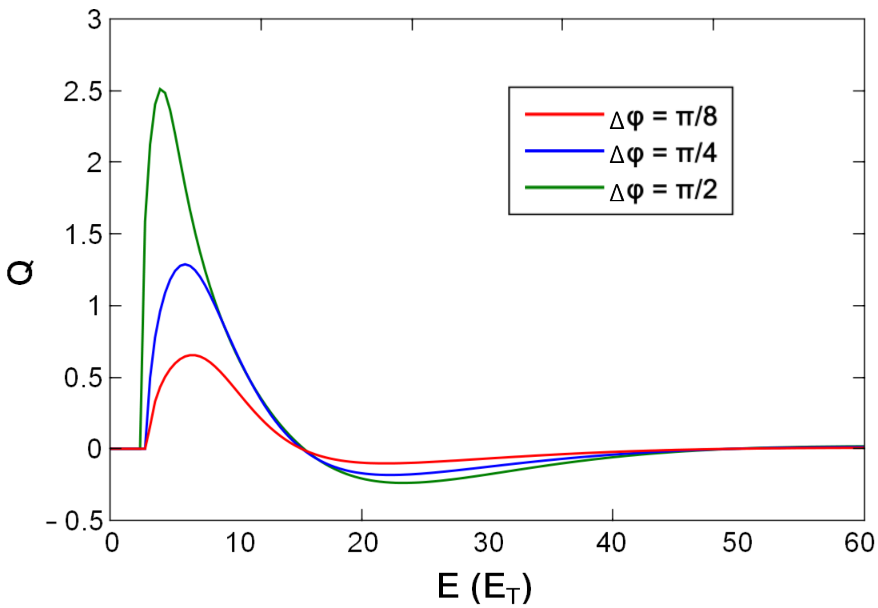

Figure 2.10. Spectral supercurrent Q as a function of energy in units of E_T of the wire, for $\Delta\phi = \pi/8$ (red), $\pi/4$ (blue), and $\pi/2$ (green). $\Delta = 1000E_T$.

integrating $Q(E)$ in energy. The maximum value of I_s is called the critical current I_c. By taking into account the relation between the diffusion constant D and the normal resistance R_N of the wire with length L and cross-sectional area A, $R_N = L/e^2N(0)AD$ [**19**], we obtained $eI_cR_N/E_T \simeq 10$. For this numerical calculation, the superconducting gap is again set to $\Delta = 1000\ E_T$. According to the work by Dubos [**42**], in the long junction limit, the critical current I_c across the normal metal wire is determined by the Thouless energy E_T not the gap Δ and is given by $eI_cR_N/E_T = 10.82$ as $T \to 0$ with the assumption of perfectly transparent interfaces between the superconducting reservoir and the normal metal wire on each end, which is in a good agreement with the result of our simulation.

Now I consider a slightly more complicated geometry shown in Figure. 2.11. It should be noted that there is a "dangling" normal metal arm connected on one end to the center of the normal metal wire between two superconducting reservoirs, and the other end to a normal

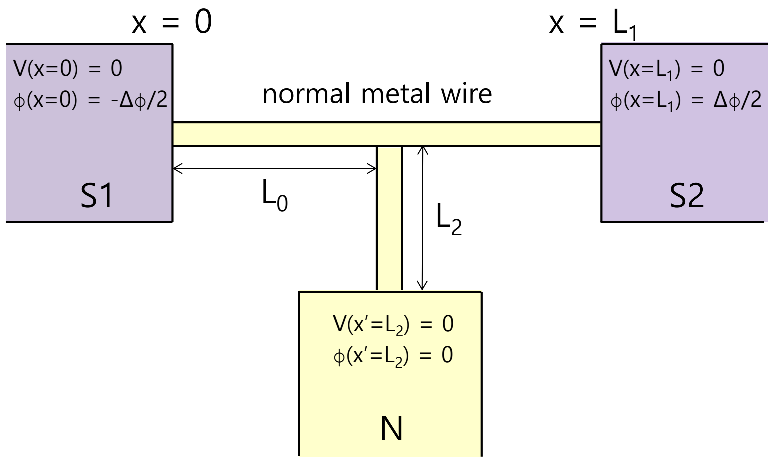

Figure 2.11. Single normal metal wire between two superconducting reservoirs with a dangling arm connected to the center of the normal metal wire at one end and to a normal reservoir at the other end.

reservoir. For numerical calculations, the geometry is broken down into three normal metal wires, two with length L_0 composing the proximity-coupled normal metal, thus $L_1 = 2L_0$, and one with L_2 connected to the normal reservoir, meeting at the node. The Usadel equation is scaled by the Thouless energy $E_{T_0} = \hbar D/L_0^2$ of the wire with length L_0 and the factor $\alpha = L_2/L_0$ is included as in Eq. (2.59b) to take into account different lengths L_2 of the dangling arm. Final numerical results are presented in terms of the Thouless energy of the proximity-coupled normal metal wire with length L_1, $E_T = \hbar D/L_1^2$, to maintain the consistency with the case of the simple SNS junction to make the comparison more convenient.

We first calculated the DOS along the normal metal wire to see if there is any change from the case of the simple SNS due to the modification in the geometry. Figure 2.12 shows the result of our numerical calculation of the normalized DOS for $\Delta\phi = 0$ and $L_2 = L_0$, with $\Delta = 1000\ E_T$ where E_T is the Thouless energy of the proximity-coupled normal metal wire, $E_T = \hbar D/L_1^2$, as before. Compared to the case of the simple SNS junction, the normalized

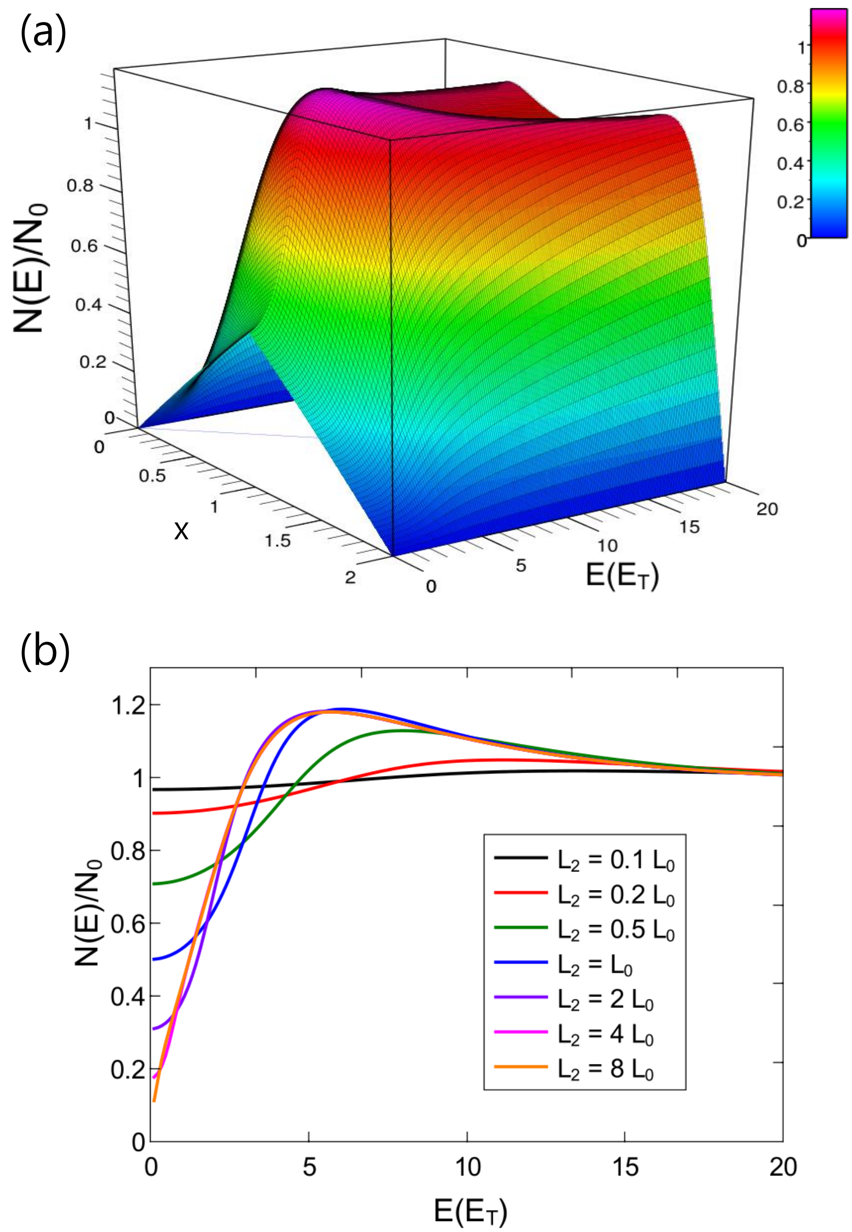

Figure 2.12. (a) Normalized DOS $N(E)/N(0)$ in the normal metal wire presented in Figure 2.11 as a function of position x and energy E. $\Delta = 1000\ E_T$ and $\phi = 0$ for the calculation. (b) Normalized DOS as a function of energy at the node for various lengths L_2.

DOS at low energies is highly dependent on the position in the normal metal wire showing a maximum at the node where the dangling arm is connected. We repeated the calculation by varying the length of the dangling arm L_2 with respect to the length L_0 used for scaling the Usadel equation. Figure 2.12 (b) exhibits the normalized DOS calculated at the node, which shows that the modification of the normalized DOS of the normal metal wire due to the proximity effect from two superconductors is reduced as the normal reservoir is placed closer to the node.

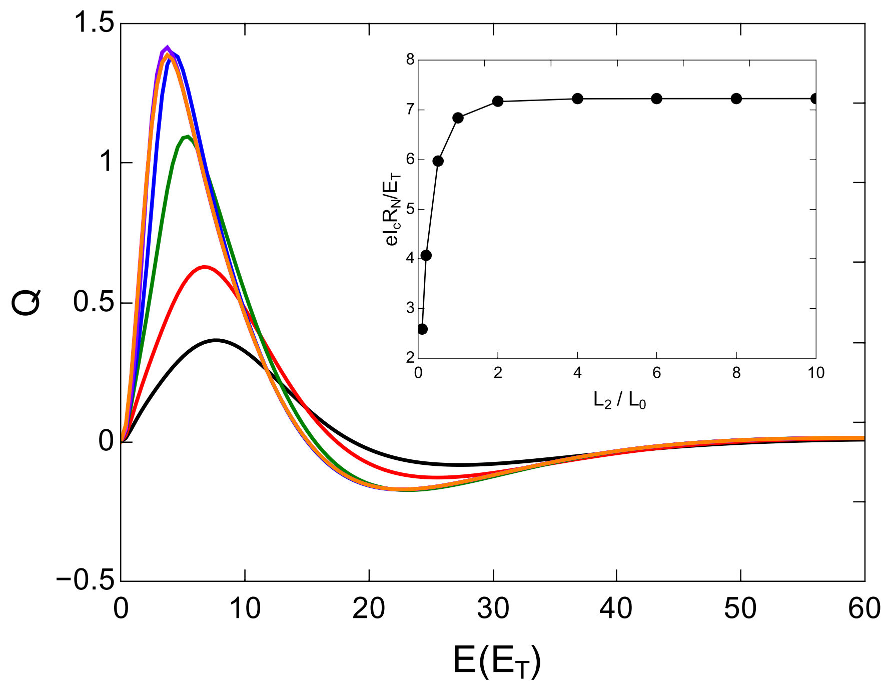

Figure 2.13. Spectral supercurrent Q numerically calculated for $\phi = \pi/2$ as the length L_2 is varied. The same color code is used as in the previous plot: 0.1 L_1 (black), 0.2 L_1 (red), 0.5 L_1 (green), L_1 (blue), 2 L_1 (purple), 4 L_1 (pink), and 8 L_1 (orange). Inset: Critical current eI_cR_N/E_T as a function of L_2/L_0.

Then we calculated the spectral supercurrent $Q(E)$ between two superconducting reservoirs for $\Delta\phi = \pi/2$. Figure 2.11 exhibits the result of the calculation for various lengths of L_2, the same values used to calculate the normalized DOS shown above. The maximum value of $Q(E)$ is reduced and the value of the energy where the maximum appears is shifted as the normal reservoir is placed closer to the normal wire between two superconducting reservoirs. It should be noted that the maximum value of $Q(E)$ does not fully recover the value obtained from the simple SNS junction even if the normal reservoir is placed far enough. As the supercurrent I_s at low temperature is obtained by integrating $Q(E)$ over E, the result indicates that I_s is also significantly reduced in the presence of the normal reservoir and further reduced as the normal reservoir is placed closer. The inset of Figure 2.10 explicitly shows the calculated critical current I_c as a function of L_2. As L_2 increases, I_c also increases but saturates at $eI_cR_N/E_T \simeq 7.2$, smaller than the I_c of the SNS junction.

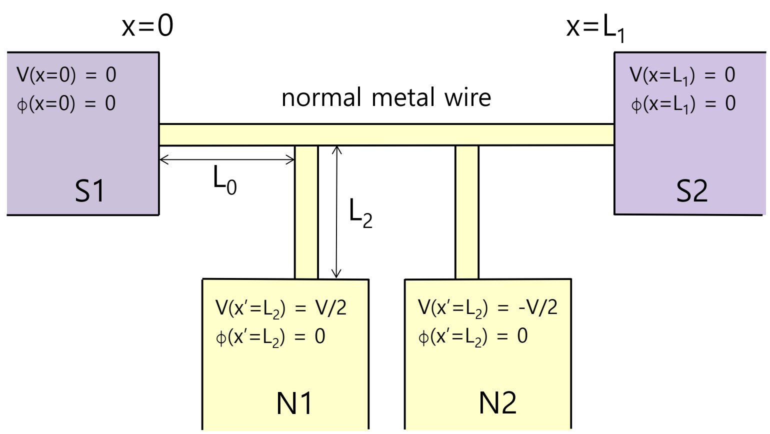

Figure 2.14. Proximity-coupled normal metal wire between two superconductors. For local configuration, voltage difference V is applied between N1 and N2 to calculate current as shown in the figure, For nonlocal configuration, voltage V is applied on N1 with S1 grounded to calculate the nonlocal voltage V_{nl}.

Since we successfully reproduced the expected results in relatively simple geometries, we are ready to consider the geometry equivalent to the ones of the samples measured in the experiments. Figure (2.14) shows the simplest version of such geometries. Similarly to the previous case, the geometry is broken down to five normal metal wires, three with length L_0 composing the proximity-coupled normal metal wire between two superconductors with

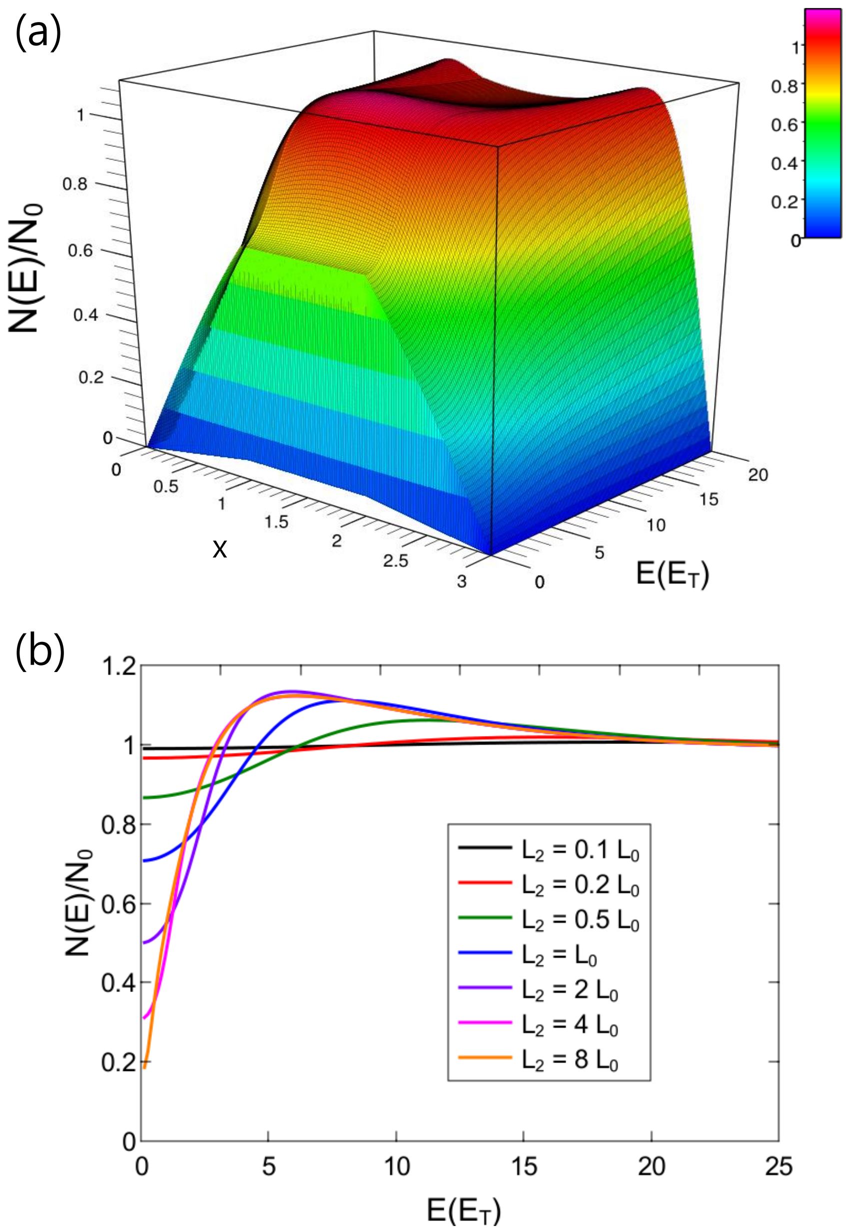

Figure 2.15. (a) Normalized DOS $N(E)/N(0)$ in the normal metal wire presented in Figure 2.14 as a function of position x and energy E. $\Delta = 1000\ E_T$ and $\Delta\phi = 0$ for the calculation. (b) Normalized DOS as a function of energy at the center of the proximity-coupled normal metal for various lengths L_2.

length L_1, thus $L_1 = 3L_0$, two with length L_2 connected to normal reservoirs N1 and N2 respectively. Again, the Usadel equation is scaled by the Thouless energy $E_{T_0} = \hbar D/L_0^2$ of

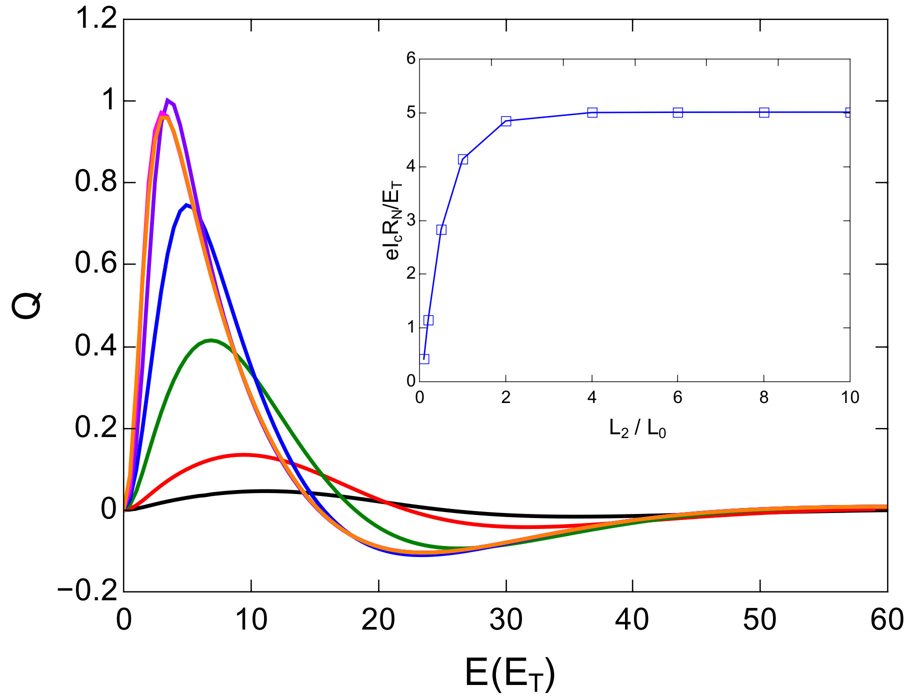

Figure 2.16. Spectral supercurrent Q numerically calculated for $\Delta\phi = \pi/2$ as the length L_2 is varied. The same color code is used as in the previous plot: 0.1 L_1 (black), 0.2 L_1 (red), 0.5 L_1 (green), L_1 (blue), 2 L_1 (purple), 4 L_1 (pink), and 8 L_1 (orange). Inset: Critical current eI_cR_N/E_T as a function of L_2/L_0.

the wire with length L_0 and the factor $\alpha = L_2/L_0$ is included for the ones with length L_2 connected to the normal reservoirs. Final numerical results are presented in terms of the Thouless energy of the proximity-coupled normal metal wire with length L_1, $E_T = \hbar D/L_1^2$, as before.

We first calculated the DOS in the proximity-coupled normal metal. Figure 2.15 shows the result for $\Delta\phi = 0$ and $L_2 = L_0$, with $\Delta = 1000\ E_T$ where E_T is the Thouless energy of the proximity-coupled normal metal. While there is a significant dependence of the DOS on the position in the range from the superconducting reservoir to the first node and from the second node to the other superconducting reservoir, the DOS is more or less constant between the two nodes. Similarly to the geometry considered before, the depth of the minigap is reduced as the normal reservoirs are placed closer to the nodes as shown in Figure 2.15 (b).

Figure 2.16 shows the dependence of the spectral supercurrent $Q(E)$ on the length L_2 of the normal metal wires connected to the normal reservoirs, analogous to Figure 2.13 shown before. Again, the maximum value of $Q(E)$ is reduced and the value of the energy where the maximum appears is shifted as the normal reservoirs are placed closer to the normal wire between two superconducting reservoirs. However, it should be noted that the overall value of $Q(E)$ is further suppressed due to the increased number of normal reservoir, which is translated into the reduced value of the calculated critical current I_c. The inset of the Figure shows I_c as a function of L_2 in the limit $T \to 0$, which again saturates as L_2 increases but at a reduced value of $eI_cR_N/E_T \simeq 5$.

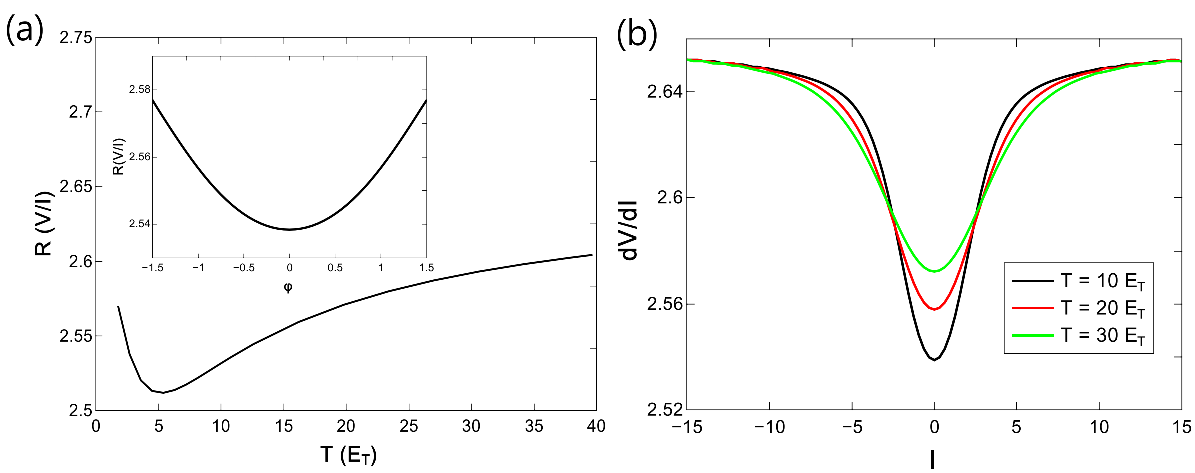

Figure 2.17. Left: Resistance through the normal metal wire between N1 and N2 as a function of temperature. A small voltage $eV = \pm\ 0.01\ E_T$ is applied on N1 and N2, respectively. Inset: Resistance (the same configuration as the main plot) as a function of the phase difference $\Delta\phi$ between S1 and S2. Right: Differential resistance dV/dI of the same local configuration as a function of current at $T = 10E_T$, $15E_T$, and $20E_T$.

Having considered some of the equilibrium properties of the system, let us discuss the transport through the system under the application of bias voltage. Among many measurement configurations that can be numerically simulated, we first consider a local configuration. As noted in Figure 2.14, by applying the voltage $V/2$ on the normal reservoir N1 and $-V/2$ on N2, respectively, and calculating the charge current, we can extract the local conductance (or resistance) of the normal metal wire between the two normal reservoirs N1 and N2, which includes a part of the proximity-coupled normal metal between the two superconducting reservoirs S1 and S2. Figure 2.17 (a) shows the calculated local resistance as a function of temperature T with the length L_2 of normal metal wires connected to the normal reservoirs set to $L_2 = L_0$. The resistance $R = V/I$ is obtained by calculating the current I under a small voltage $eV = \pm 0.01\ E_T$ applied on N1 and N2 respectively, where $E_T = \hbar D/L_1^2$ is the Thouless energy of the normal metal wire with length L_1 between S1 and S2. Similar to the case of a single wire, the reentrant behavior of the resistance is observed with the minimum at $T \sim 5.6\ E_T$. Figure 2.17 (b) exhibits the differential resistance as a function of bias current. Temperature is set to $T = 10$, 20, and 30 E_T where the resistance undergoes the decrease in the temperature dependence shown in (a). To calculate the differential resistance dV/dI, the current I along the normal wire between N1 and N2 is calculated first at different values of voltages $\pm V/2$ set on each of reservoirs and then the differential resistance is obtained by numerically differentiating the applied voltage difference V with respect to the resulting current I. The bias dependence shows a central dip near zero bias which develops further as temperature is lowered. This implies that the decrease of the resistance at low temperatures is associated with the appearance of the dip in the differential resistance.

Figure 2.18 (a) shows the temperature dependence of the resistance in the same configuration as the length L_2 is varied. While all the traces exhibit the reentrant behavior

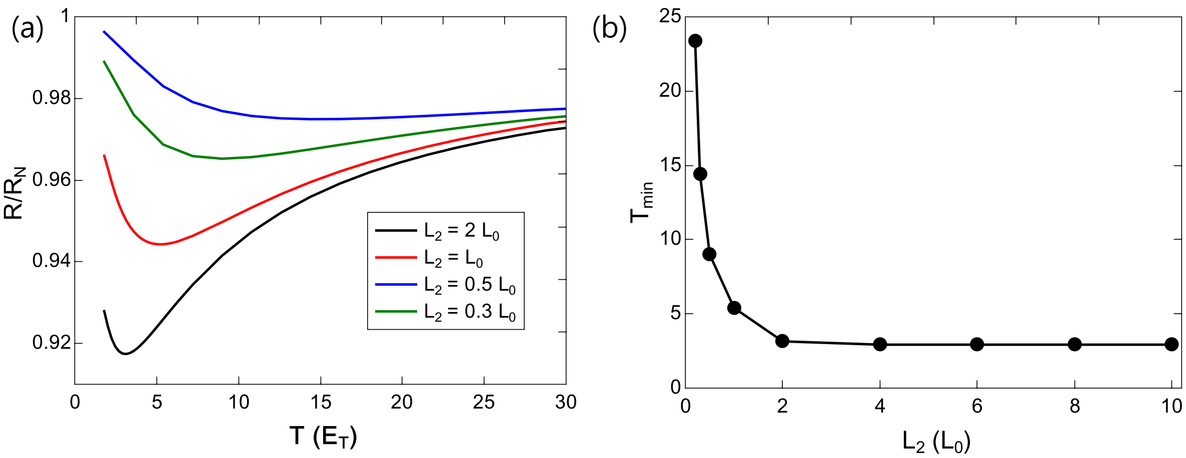

Figure 2.18. Normalized resistance R/R_N as a function of temperature as the length L_2 is varied. The configuration to calculate the resistance is the same as shown in Figure 2.14.

at low temperatures, the temperature T_{min} where the minimum of the resistance appears varies as a function of L_2. When the normal reservoirs are placed far enough from the proximity-coupled normal metal, the minimum of the resistance appears at a constant temperature of $T_{min} \simeq 2.9\ E_T$, as shown in (b). The increase of T_{min} as the normal metal reservoirs are placed closer can be attributed to the reduction of the phase coherence L_ϕ in the proximity-coupled normal metal wire as shown by the calculation reported in Ref [**43**].

Fig. 2.19 presents experimental results of the work done by Cadden-Zimansky *et al.* [**44**] where they measured the resistance of the proximity-coupled normal metal between two superconductors. Overall, the result of our numerical calculations shows good agreement as the resistance decreases at low temperatures at which the differential resistance exhibits a dip near zero bias current. However, the up-turn of the resistance is not observed in the experiment even at the lowest temperatures. According to the reference, E_T of the proximity-coupled normal metal wire calculated based on the measurement of the diffusion coefficient D is $E_T = 2.6\ \mu e\text{V}$, which corresponds to the temperature $T \simeq 30$ mK. Then the minimum

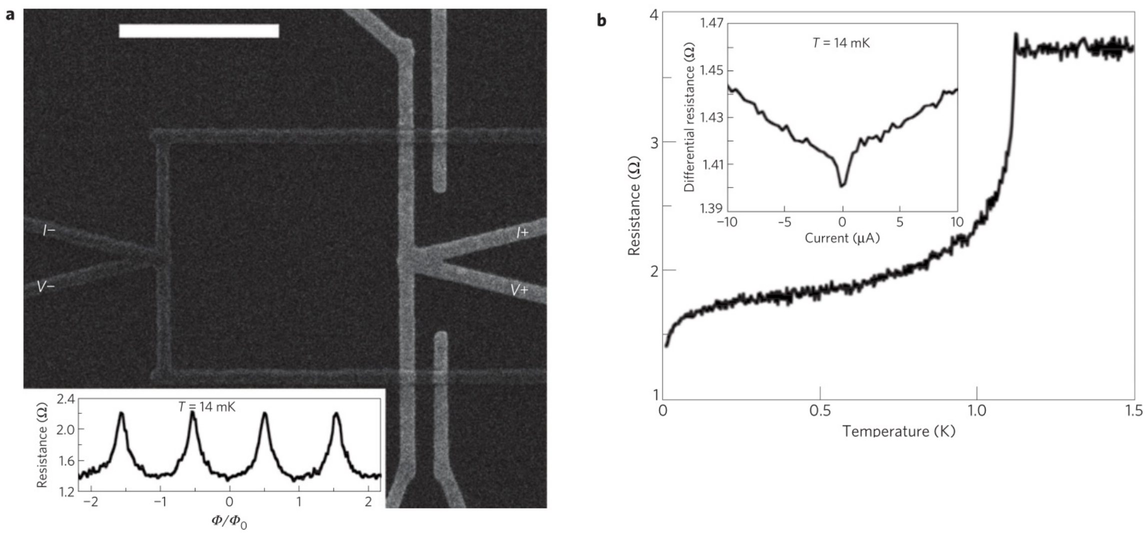

Figure 2.19. (a) Scanning electron microscope (SEM) image of a sample which consists of normal metal leads (Au: bright color) and superconducting leads (Al: darker color). The scale bar is 1 μm. The inset shows the resistance oscillation of the loop as function of flux through the loop, which has a $\Phi_0 = h/2e$ period. (b) Local resistance of the hybrid loop as a function of temperature. Inset: The differential resistance of the loop at 14 mK as a function of current. Figure taken from Ref. [**44**].

of the resistance is expected to appeared at $T_{min} \simeq 90$ mK with the normal reservoirs placed far enough, which is not the case in the experiment. We conjecture that T_{min} may have been shifted down to much lower temperatures below the lowest temperature accessible in the experiment. We will discuss the possible sources of the discrepancy in Chapter 4.

Let us now consider the nonlocal configuration where voltage V is applied to N1, with S1 grounded, and measure the voltage difference $V_{\rm nl}$ between N2 and S2 as a response. Before imposing boundary conditions for numerical simulations, let me give a qualitative explanation of the current along different sections of the sample in this measurement configuration. Due to the Josephson coupling between S1 and S2 below the critical temperature T_c, the voltage at S2 remains zero when S1 is grounded. Therefore, with a finite voltage V applied

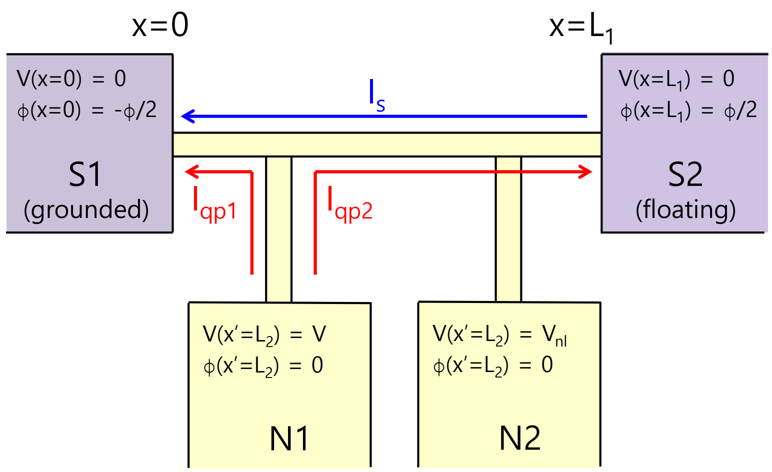

Figure 2.20. Current separation model. A supercurrent I_s is generated to cancel the quasiparticle current I_{qp2}.

on N1, a finite quasiparticle current I_{qp} is divided into two paths, I_{qp1} and I_{qp2} satisfying $I_{\mathrm{qp}} = I_{\mathrm{qp1}} + I_{\mathrm{qp2}}$ flowing into S1 and S2 respectively, as shown in Figure 2.20. Such a separation of applied current has been reported before in an experiment using a similar geometry of the sample by Crosser *et al.* [**45**]. The ratio of $I_{\mathrm{qp1}}/I_{\mathrm{qp2}}$ is determined by the length of each section of the normal metal wire with respect to the injection point of I_{qp} and the interface resistance between the normal metal wire and each superconducting reservoir. Meanwhile, there is no electrical current flowing into both N2 and S2 as they are electrically floating while measuring the voltage difference between N2 and S2 . Therefore, as a portion of quasiparticle current I_{qp2} flows into S2, supercurrent $I_s = -I_{\mathrm{qp2}}$ arises by generating the phase difference $\Delta\phi$ to compensate I_{qp2} so that the total current into S2 remains zero.

The generation of the compensating supercurrent can be readily confirmed in the numerical calculation. For example, in a simpler geometry with a dangling normal metal arm depicted in Figure 2.11, if the voltage V is applied on N while S1 is grounded and S2 is

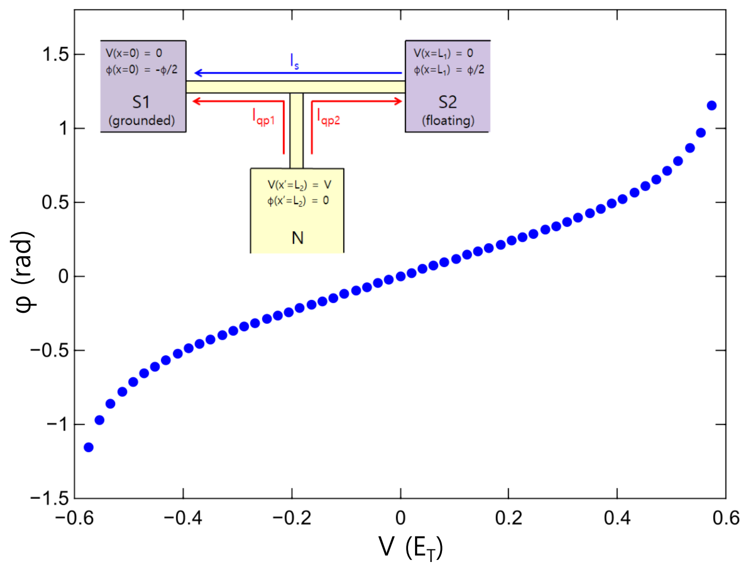

Figure 2.21. The phase difference $\Delta\phi$ as a function of the applied voltage V on N.

floating, the phase difference $\Delta\phi$ between S1 and S2 appears to generate the compensating supercurrent I_s. Figure 2.21 shows the dependence of $\Delta\phi$ on the applied voltage V on N, which increases as the amount of quasiparticle current that needs to be compensated increases as a function of the applied voltage.

In the geometry shown in Figure 2.20, however, the situation is slightly more complicated. For each value of a voltage V applied on N1, current along each path of the sample is calculated with two independent parameters of the phase difference $\Delta\phi$ between two superconducting reservoirs and the response voltage V_{nl} on N2, which should be repeated until the currents going into N2 and S2 become zero simultaneously.

II. Nonlocal correlations mediated by pure spin current

In the previous chapter, we considered the processes occurring at the normal metal-superconductor (NS) interface upon the injection of an electron, based on the simple formalism developed by Blonder, Tinkham, and Klapwijk. Among the processes, Andreev reflection is of particular interest as it occurs due to the fundamental difference in the normal metal and superconductor. More interestingly, in the presence of the second NS interface spatially separated from the first one, Andreev reflection occurs at the second interface as well, as a response to the injection of current on the first interface. This process is called crossed Andreev reflection (CAR), which occurs due to the mutual interaction of two spatially separated electrons with the superconductor [**46, 47, 48, 49**].

As an investigation of the nonlocal correlations mediated by the superconductor, in this chapter, we will theoretically propose a new scheme of injecting pure spin current into a superconductor. Before discussing the result in detail, I will briefly describe the process of CAR and another process called elastic cotunneling (EC) occurring at NSN structures involving two NS interfaces along with the introduction of theoretical and experimental works performed before. Then I will present the result of our theoretical consideration which shows that on the contrary to the injection of charge current, the nonlocal correlations associated with CAR and EC add up as a response to the injection of pure spin current, which is due to the singlet spin configuration of the electrons forming Cooper pairs in a conventional s-wave superconductor.

2.5. Crossed Andreev reflection (CAR) and elastic cotunneling (EC)

Crossed Andreev reflection (CAR) and elastic cotunneling (EC) couple two electrons from two spatially separated normal metal leads N_1 and N_2, as depicted in Figure 2.22. CAR is the nonlocal version of the Andreev reflection in which an electron with one spin orientation,

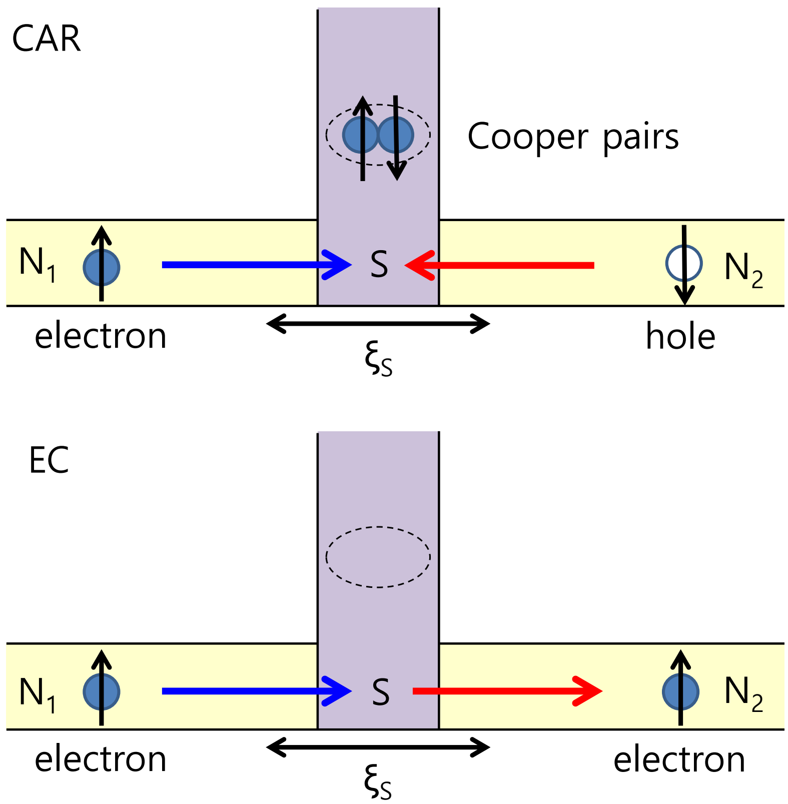

Figure 2.22. Schematic diagram for crossed Andreev reflection (top) and elastic cotunneling (bottom) occurring at two NS interfaces. Blue and red solid arrows note injected electron flux and induced electron flux, respectively.

e.g., spin-up injected from N_1 is retroreflected as a hole with spin-down into N_2 generating a Cooper pair in the superconductor. On the other hand, in EC, the spin-up electron directly tunnels through the superconductor from N_1 giving rise to the spin-up electron into N_2. While the injection current induces a current from the second normal metal lead into the superconductor to form the Cooper pair inside for CAR, the direction of the induced current is opposite for EC, which result in the opposite contribution to the induced current. As the relative amplitudes of CAR and EC are predicted to depend on the transparency of the interface [**50**], the effect of electron-electron interactions [**51**], and so on, the direction of the net induced current in the second normal metal may be parallel or antiparallel to the direction of the injected current. Experimentally, nonlocal correlations due to CAR and EC in charge transport have been verified by many different groups as shown in Refs. [**1, 2, 3**].

In addition to CAR and EC, there are additional processes that may contribute to the nonlocal correlations in NSN structures or FSF structures with normal metals replaced by ferromagnets. These are charge [**52, 53, 54, 55, 56**] and spin [**57, 58, 59**] imbalance associated with the injection of quasiparticles with energies larger than the superconducting gap Δ, into the superconductor. In contrast to these studies, we propose an experiment in the regime of subgap transport. Thus, no quasiparticle is injected above the gap, and the effect does not depend on the long spin relaxation times recently observed in the nonlocal measurements of Refs. [**57, 58, 59**] at applied bias voltage larger than Δ/e.

As I will present our theoretical study on nonlocal correlations induced in a NSN structure in response to a pure spin current, not a charge current as introduced so far, let us first discuss how to generate and detect a pure spin current by using NF interfaces.

2.6. Generation and detection of pure spin current

Generating and detecting a pure spin current has been drawing the interests of researcher for more than a decade. The term "pure" denotes that there is a separation between the flow of charge and that of spin in the sample under consideration. For instance, as shown in Figure 2.23(b), spin accumulation is generated at the interface between a ferromagnet (Permalloy: Py1) and a normal metal (Copper: Cu) by sending a charge current through the junction, due to the difference in the polarization of electrons in two metals. The diffusion of spin accumulation, called spin current, occurs along the normal metal, as well as along the ferromagnet, into all directions. If the charge current is drained through the left side of the normal metal as depicted, only the spin current flows between the center of the normal metal and the second ferromagnet (Py2). Since the diffusion of spin accumulation occurs within the length of λ_s, i.e., spin diffusion length, it can be detected if the spatial separation of the two ferromagnets is within λ_s. Jedema *et al.*, [**60**] experimentally demonstrated the spin

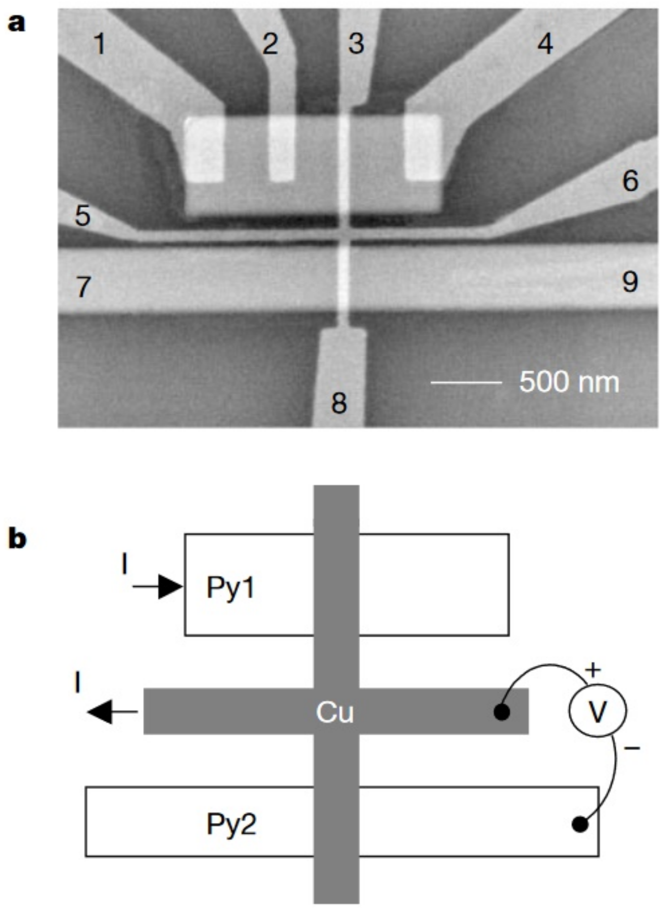

Figure 2.23. (a) Scanning electron microscope (SEM) image of a mesoscopic spin valve junction consisting of ferromagnet (Py: two wide horizontal strips) and normal metal leads (Cu: two thin vertical and horizontal wires). (b) Schematic diagram for nonlocal spin-valve measurement configuration. Current is biased from 1 to 5 and the voltage is measured between 6 and 9. Figure taken from Ref.[**60**].

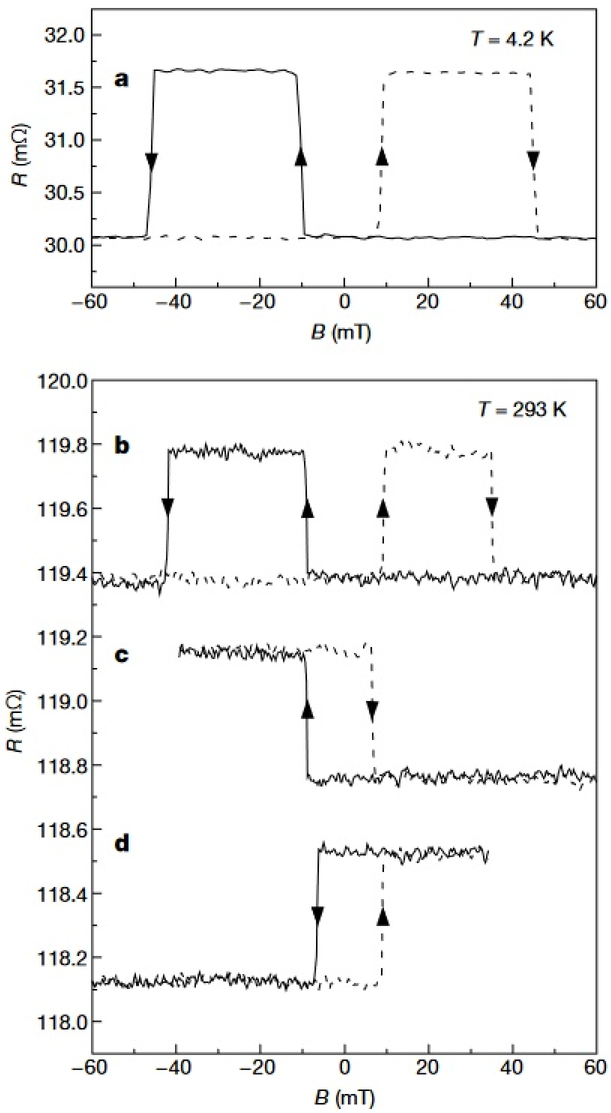

Figure 2.24. The spin valve effect at (a) 4.2K and (b) room temperature in the nonlocal spin-valve configuration. (c) and (d) show the 'memory effect'. Figure taken from Ref. [**60**].

diffusion at room temperature, which manifests itself as the nonlocal resistance dependent on the relative magnetization of two ferromagnets, similar to the so called "spin valve effect" as shown in Figure 2.24.

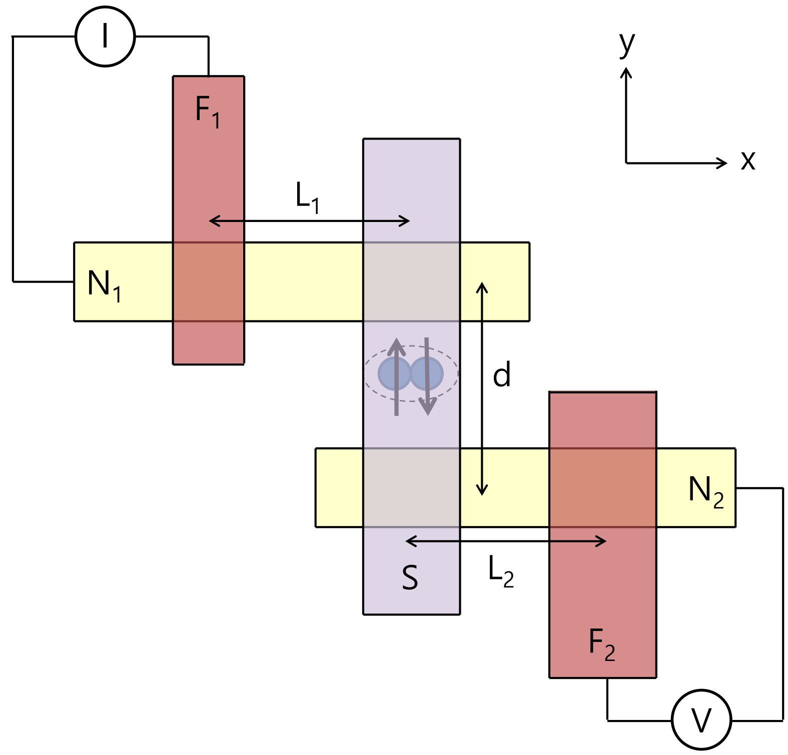

Figure 2.25. Schematic diagram of the device considered. The bias current is applied from a ferromagnet F_1 to a normal metal N_1 and nonlocal voltage is measured between F_2 and N_2.

Let us consider the injection and detection of pure spin current into a superconductor by using the same technique. The schematic diagram of the sample is shown in Figure 2.25. Our device is similar to the one shown above, except the normal metal wire is broken into two wires and connected by a superconductor. If one drives a bias current I from F_1 to N_1, as shown in Figure 2.25, spin accumulates at the N_1F_1 interface resulting in spin imbalance diffusing in all possible directions in N_1 as explained above. Since the bias current is drained from the left side of N_1, the right side of N_1 carries a pure spin current with no net flow of charge. The second NF interface (N_2F_2) is used to detect the spin current flowing through N_2 by measuring the nonlocal voltage $V_{\rm nl}$ between N_2 and F_2. It should be noted that F_1 and F_2 are designed to have different coercive fields. Hence, it is possible to realize both parallel and antiparallel magnetization directions by applying an external magnetic field. In the following, we assume that the normal metals are oriented along the x-axis whereas the ferromagnets are oriented along the y-axis (see Figure 2.25). To simplify the notation, we use two different coordinate systems for N_1 and N_2 with origins at each FN interface and the x-axis directed toward the superconductor, i.e., the respective NS interfaces are at $x = L_i$ $(i = 1, 2)$.

Spin accumulation and spin transport at N_i and F_i interface can be described by the model introduced in the work of Takahashi [**61**]. The current density for each spin species is driven by the electric field $\mathbf{E}_\alpha = -\nabla\phi_\alpha$ (ϕ_α: electric potential) and the gradient of the electron density of each spin species deviated from the equilibrium $\delta n_\alpha^{\uparrow,\downarrow}$ in material $\alpha = \mathrm{F}_i, \mathrm{N}_i$ $(i = 1, 2)$ as

$$j_\alpha^\uparrow = \sigma_\alpha^\uparrow \mathbf{E}_\alpha - eD_\alpha^\uparrow \nabla \delta n_\alpha^\uparrow, \tag{2.71a}$$

$$j_\alpha^\downarrow = \sigma_\alpha^\downarrow \mathbf{E}_\alpha - eD_\alpha^\downarrow \nabla \delta n_\alpha^\downarrow \tag{2.71b}$$

where $\sigma_\alpha^{\uparrow,\downarrow}$ and $D_\alpha^{\uparrow,\downarrow}$ are the spin-dependent electrical conductivity and diffusion constant. As $\delta n_\alpha^{\uparrow,\downarrow}$ is generated by the shift in the chemical potential, i.e., $\delta n_\alpha^{\uparrow,\downarrow} = N_\alpha^{\uparrow,\downarrow}\delta\epsilon_\alpha^{\uparrow,\downarrow}$ where $N_\alpha^{\uparrow,\downarrow}$ is the density of states and $\delta\epsilon_\alpha^{\uparrow,\downarrow}$ is the amount of the shift in the chemical potential from the equilibrium for up and down spin species, one can define the electrochemical potential $\mu_\alpha^{\uparrow,\downarrow} = \epsilon_\alpha^{\uparrow,\downarrow} + e\phi$ which modifies Eqs. (2.71a) to

$$j_\alpha^\uparrow = -(\sigma_\alpha^\uparrow/e)\nabla\mu_\alpha^\uparrow, \tag{2.72a}$$

$$j_\alpha^\downarrow = -(\sigma_\alpha^\downarrow/e)\nabla\mu_\alpha^\downarrow \tag{2.72b}$$

where $\sigma_\alpha^{\uparrow,\downarrow} = e^2 N_\alpha^{\uparrow,\downarrow} D_\alpha^{\uparrow,\downarrow}$. The charge current j_α is given by the sum of $j_\alpha^\uparrow$ and $j_\alpha^\downarrow$, which satisfies

$$\nabla \cdot j_\alpha = \nabla \cdot (j_\alpha^\uparrow + j_\alpha^\downarrow) = 0, \tag{2.73}$$

while the spin current j_α^s given by the difference of $j_\alpha^\uparrow$ and $j_\alpha^\downarrow$ satisfies

$$\nabla \cdot j_\alpha^s = \nabla \cdot (j_\alpha^\uparrow - j_\alpha^\downarrow) = -e\delta n_\alpha^\uparrow/\tau_{\uparrow\downarrow} + e\delta n_\alpha^\downarrow/\tau_{\downarrow\uparrow}, \tag{2.74}$$

where $\tau_{\uparrow\downarrow}$ and $\tau_{\downarrow\uparrow}$ are the scattering time of an electron from spin up to spin down state and vice versa. Using the relation $N_\alpha^\uparrow/\tau_{\uparrow\downarrow} = N_\alpha^\uparrow/\tau_{\downarrow\uparrow}$ known as detailed balance [**61**] leads Eq. (2.73) and Eq. (2.74) to

$$\nabla^2(\sigma_\alpha^\uparrow \mu_\alpha^\uparrow + \sigma_\alpha^\downarrow \mu_\alpha^\downarrow) = 0 \tag{2.75}$$

and

$$\nabla^2(\mu_\alpha^\uparrow - \mu_\alpha^\downarrow) = (1/\lambda_\alpha^2)(\mu_\alpha^\uparrow - \mu_\alpha^\downarrow). \tag{2.76}$$

Here, the spin diffusion length is $\lambda_\alpha = \sqrt{D_\alpha \tau_\alpha}$, where $\tau_\alpha^{-1} = \frac{1}{2}(\tau_{\alpha\uparrow\downarrow}^{-1} + \tau_{\alpha\downarrow\uparrow}^{-1})$ and $D_\alpha^{-1} = (N_\alpha^\uparrow D_\alpha^{\uparrow -1} + N_\alpha^\uparrow D_\alpha^{\downarrow -1})/(N_\alpha^\uparrow + N_\alpha^\uparrow)$. The parameters for the normal metals are spin-independent, i.e., $\sigma_{\mathrm{N}}^\uparrow = \sigma_{\mathrm{N}}^\uparrow = \frac{1}{2}\sigma_{\mathrm{N}}$, $D^\uparrow = D^\downarrow$, etc., whereas they are spin-dependent for the ferromagnets, i.e., $\sigma_{\mathrm{F}}^\uparrow \neq \sigma_{\mathrm{F}}^\uparrow$, $D^\uparrow \neq D^\downarrow$. The general solution of Eq. (2.75) and Eq. (2.76) in F_i reads

$$\mu_{\mathrm{F}_i}^{\uparrow,\downarrow}(y) = \mu_{\mathrm{F}_i}(0) + \left(p_{\mathrm{F}_i} \pm \frac{\sigma_{\mathrm{F}_i}^{\downarrow,\uparrow}}{\sigma_{\mathrm{F}}} e^{-|y|/\lambda_{\mathrm{F}}} \right) \delta\mu_{\mathrm{F}_i}(0) + \frac{eI_i y}{\sigma_{\mathrm{F}} A_{\mathrm{F}}} \Theta(y) \tag{2.77}$$

with $I_1 = I$ and $I_2 = 0$. $\Theta(y)$ is the Heaviside function. Total conductivities $\sigma_{\mathrm{F}_i} = \sigma_{\mathrm{F}_i}^{\uparrow} + \sigma_{\mathrm{F}_i}^{\downarrow}$, cross-sections A_{F_i}, and spin-diffusion lengths λ_{F_i} are assumed to be identical for the wires F_1 and F_2 for simplicity, so I will drop the subscript i for the rest of this chapter. The magnitude of the polarity defined as $p_{\mathrm{F}_i} = (\sigma_{\mathrm{F}_i}^{\uparrow} - \sigma_{\mathrm{F}_i}^{\downarrow})/\sigma_{\mathrm{F}}$ is the same for $i = 1, 2$, while their sign is determined by the magnetization direction in F_i, $p_{\mathrm{F}_i} = \pm p_{\mathrm{F}}$. Here I take the $(+)$ sign for spin up being the majority carrier and the $(-)$ sign for spin down being the majority carrier in each ferromagnet. By using Eq. ((2.77)), the spin accumulation $\delta\mu_{\mathrm{F}_i}(0)$ at the $\mathrm{F}_i\mathrm{N}_i$ interface can be related to the drive current I_i and the spin current $I^s_{\mathrm{F}_i\mathrm{N}_i}$ flowing through the $\mathrm{F}_i\mathrm{N}_i$ interface as follows:

$$\delta\mu_{\mathrm{F}_i}(0) = \frac{1}{2} e R_{\mathrm{F}} \left(p_{\mathrm{F}_i} I_i - I^s_{\mathrm{F}_i\mathrm{N}_i} \right), \tag{2.78}$$

where $R_{\mathrm{F}} = \lambda_{\mathrm{F}}/[A_{\mathrm{F}}\sigma_{\mathrm{F}}(1 - p_{\mathrm{F}}^2)]$.

Meanwhile, the currents at the $\mathrm{F}_i\mathrm{N}_i$ interface may also be expressed in terms of the potential drops across the interface, and the interface tunnel conductance G^{σ}_{Ti}. By using $I_i^{\sigma} = \frac{G^{\sigma}_{Ti}}{e} \left(\mu^{\sigma}_{\mathrm{F_i}}|_{z=0^+} - \mu^{\sigma}_{\mathrm{N_i}}|_{z=0^-} \right) = \frac{G^{\sigma}_{Ti}}{e} \left(\mu^{\sigma}_{\mathrm{F_i}}(0) - \mu^{\sigma}_{\mathrm{N_i}}(0) \right)$ and neglecting the spin-flip scattering at the interface, I obtain

$$I_i = \frac{G_{T_i}}{e} \left(\mu_{\mathrm{F}_i\mathrm{N}_i} + p_{T_i} \delta\mu_{\mathrm{F}_i\mathrm{N}_i} \right), \tag{2.79a}$$

$$I^s_{\mathrm{F}_i\mathrm{N}_i} = \frac{G_{T_i}}{e} \left(p_{T_i} \mu_{\mathrm{F}_i\mathrm{N}_i} + \delta\mu_{\mathrm{F}_i\mathrm{N}_i} \right), \tag{2.79b}$$

where $G_{T_i} = G^{\uparrow}_{T_i} + G^{\downarrow}_{T_i}$ and $p_{T_i} = (G^{\uparrow}_{T_i} - G^{\downarrow}_{T_i})/G_{T_i}$ are related to the (tunnel) conductances $G^{\uparrow,\downarrow}_{T_i}$ of the $\mathrm{F}_i\mathrm{N}_i$ interface for spin up and spin down electrons. In addition, $\mu_{\mathrm{F}_i\mathrm{N}_i} = \mu_{\mathrm{F}_i}(0) - \mu_{\mathrm{N}_i}(0)$ and $\delta\mu_{\mathrm{F}_i\mathrm{N}_i} = \delta\mu_{\mathrm{F}_i}(0) - \delta\mu_{\mathrm{N}_i}(0)$. The sign of p_{T_i} is again dependent on the magnetization direction of the ferromagnet as mentioned before. We can rearrange the equations by inverting them to obtain

$$\mu_{\mathrm{F}_i\mathrm{N}_i} = eR_{T_i}\left(I_i - p_{T_i} I^s_{\mathrm{F}_i\mathrm{N}_i}\right), \tag{2.80a}$$

$$\delta\mu_{\mathrm{F}_i\mathrm{N}_i} = eR_{T_i}\left(-p_{T_i} I_i + I^s_{\mathrm{F}_i\mathrm{N}_i}\right), \tag{2.80b}$$

where $R_{T_i} = 1/[G_{T_i}(1-p^2_{T_i})]$.

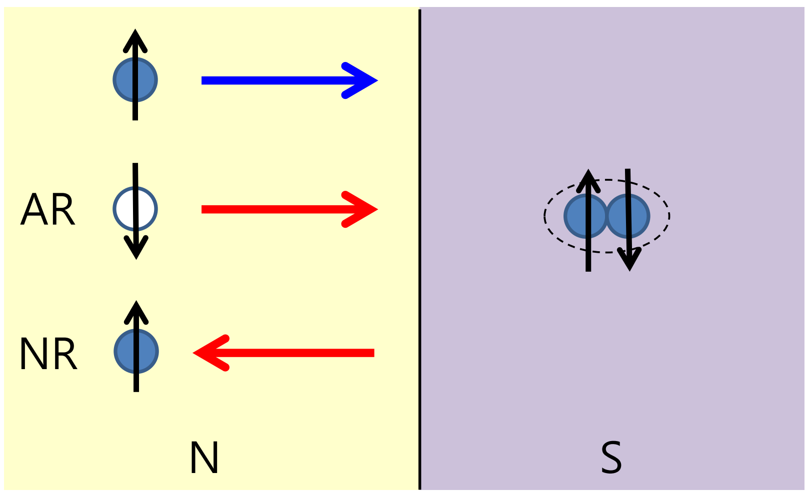

Figure 2.26. Local process occurring at an NS interface. Andreev reflection (AR) and normal reflection (NR) take place as a response to the injection of an electron. Blue and red solid arrows note injected electron flux and induced electron flux, respectively.

2.7. Processes occurring at NS interfaces due to pure spin current injection

Before considering the process occurring at NS interfaces, let us first take a look at the solution in the normal metals. The general solution of Eqs. (2.75) and (2.76) in N_i reads

$$\mu^{\uparrow,\downarrow}_{\mathrm{N}_i}(x) = \mu_{\mathrm{N}_i}(0) \pm \frac{1}{2} eR_{\mathrm{N}}\left(I^s_{\mathrm{F}_i\mathrm{N}_i} e^{-\frac{|x|}{\lambda_{\mathrm{N}}}} - I^s_{\mathrm{N}_i\mathrm{S}_i} e^{-\frac{|L_i - x|}{\lambda_{\mathrm{N}}}}\right) - \frac{eI_i x}{\sigma_{\mathrm{N}} A_{\mathrm{N}}}\theta(-x) \tag{2.81}$$

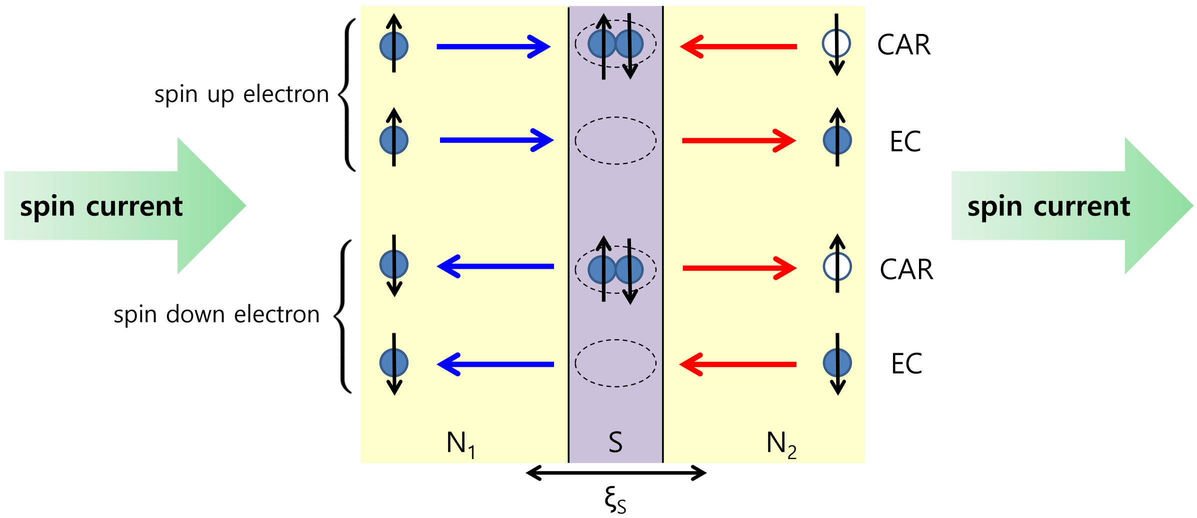

Figure 2.27. Nonlocal correlations in N_1SN_2 structure. A pure spin, represented by a spin up electron and a spin down electron flowing in the opposite direction, is injected from N_1 into S. By two nonlocal processes, CAR and EC, a pure spin current is induced in N_2. Blue and red solid arrows note injected electron flux and induced electron flux, respectively.

with $R_\mathrm{N} \equiv 1/G_\mathrm{N} = \lambda_\mathrm{N}/\sigma_\mathrm{N} A_\mathrm{N}$. As for the ferromagnets, here we also assume identical cross-sections A_N and spin-diffusion lengths λ_N, and conductivities σ_N in the wires N_1 and N_2. Furthermore, $\sigma_\mathrm{N}^\uparrow = \sigma_\mathrm{N}^\downarrow = \sigma_\mathrm{N}/2$. Using these equations, we find in particular

$$\delta\mu_{\mathrm{N}_i}(0) = \frac{1}{2} e R_\mathrm{N} \left(I^s_{\mathrm{F}_i\mathrm{N}_i} - I^s_{\mathrm{N}_i\mathrm{S}_i} e^{-L_i/\lambda_\mathrm{N}} \right), \tag{2.82a}$$

$$\delta\mu_{\mathrm{N}_i}(L_i) = \frac{1}{2} e R_\mathrm{N} \left(I^s_{\mathrm{F}_i\mathrm{N}_i} e^{-L_i/\lambda_\mathrm{N}} - I^s_{\mathrm{N}_i\mathrm{S}_i} \right). \tag{2.82b}$$

Figure 2.27 illustrates the processes taking place at the N_iS interfaces. A pure spin current, in terms of a spin up species, is injected from N_1 into S as a spin up electron and a spin down electron flow in the opposite direction. In addition to two local processes, local Andreev reflection (AR) and normal reflection (NR), occurring at an N_1S interface as illustrated in Figure 2.26, two nonlocal processes, crossed Andreev reflection (CAR) and elastic cotunneling (EC) take place at N_2S interface. Figure 2.27 is an extended version of

Figure 2.25 with the processes for a spin down electron added. Among these processes, only the nonlocal processes, CAR and EC, contribute to the nonlocal signal. It should be noted that a pure spin current is induced in N_2 by CAR and EC which make contributions to the spin current in the same direction. If the length of the superconducting link d between N_1 and N_2 is much longer than ξ_S, these processes are suppressed and only AR and NR occur at the N_1S interface, hence the detector voltage between N_2 and F_2 is zero. However, in the opposite regime where d is shorter than ξ_S, nonlocal processes such as CAR and EC can occur and generate a spin current in N_2, the process of which is schematically depicted in Figure 2.27. Then, the resulting spin imbalance at the N_2F_2 interface yields a finite voltage difference between N_2 and F_2 as explained before. There are a couple of important aspects that should be noted here. First, as can be seen in Figure 2.27, both CAR and EC contribute to a spin current in N_2 in the same direction, such that their contributions to the spin signal add up. This is completely different from the case of charge current, where one measures the difference between CAR and EC. In addition, due to the fact that the superconductor cannot support spin accumulation inside, the spin of an electron injected into the superconductor at the N_1S interface is transferred to N_2 leaving no net spin in the superconductor. Therefore, the spin current injected from N_1 into S, $I^s_{\mathrm{N_1S}}$, equals the spin current injected from S into N_2, $-I^s_{\mathrm{N_2S}}$, where $I^s_{\mathrm{N}_i\mathrm{S}} = I^{\uparrow}_{\mathrm{N}_i\mathrm{S}} - I^{\downarrow}_{\mathrm{N}_i\mathrm{S}}$.

The spin-resolved currents at the N_1S interface can be expressed in terms of G_{CAR} and G_{EC} in a similar way used for F_iN_i interface,

$$I^{\sigma}_{N_1S} = \frac{G_{\mathrm{CAR}}}{2e}\left[\mu^{\sigma}_{N_1}(L_1) + \mu^{\bar{\sigma}}_{N_2}(L_2) - 2\mu_S\right] + \frac{G_{\mathrm{EC}}}{2e}\left[\mu^{\sigma}_{N_1}(L_1) - \mu^{\bar{\sigma}}_{N_2}(L_2)\right] \tag{2.83}$$

where $\sigma =\uparrow,\downarrow$, $\bar{\sigma} =\downarrow,\uparrow$, and $\mu_S = \mu^{\uparrow}_{N_i}(L_i) + \mu^{\downarrow}_{N_i}(L_i)$. Therefore, the spin current through the superconductor, $I^s_{\mathrm{S}} = I^s_{\mathrm{N_1S}} = -I^s_{\mathrm{N_2S}}$, is related to the difference between the spin imbalances $\delta\mu_{\mathrm{N}_i}(L_i) = [\mu^{\uparrow}_{\mathrm{N}_i}(L_i) - \mu^{\downarrow}_{\mathrm{N}_i}(L_i)]/2$ at the two interfaces as follows:

$$I^s_{\mathrm{S}} = \frac{G^+_{\mathrm{S}}}{e}[\delta\mu_{\mathrm{N}_1}(L_1) - \delta\mu_{\mathrm{N}_2}(L_2)]. \tag{2.84}$$

Note that $\mu_{\mathrm{N}_1}(L_1) = \mu_{\mathrm{N}_2}(L_2)$, with $\mu_{\mathrm{N}_i}(L_i) = [\mu^{\uparrow}_{\mathrm{N}_i}(L_i) + \mu^{\downarrow}_{\mathrm{N}_i}(L_i)]/2$, in the absence of a charge current. Furthermore, $G^+_{\mathrm{S}} = G_{\mathrm{CAR}} + G_{\mathrm{EC}}$, where $G_{\mathrm{CAR/EC}}$ are the conductances due to CAR and EC, respectively. I combined Eqs. (2.83) and (2.84) to eliminate the spin currents and to express the imbalances at the NS interfaces as

$$\begin{aligned} \delta\mu_{\mathrm{N}_i}(0) \;&=\; \frac{eR_{\mathrm{N}}}{2}\left\{ I^s_{\mathrm{F}_i\mathrm{N}_i}\left[1 - \frac{G^+_{\mathrm{S}}}{2(G^+_{\mathrm{S}} + G_{\mathrm{N}})}e^{-2L_i/\lambda_{\mathrm{N}}}\right]\right. \\ &\left.\quad + I^s_{\mathrm{F}_{\bar{i}}\mathrm{N}_{\bar{i}}}\frac{G^+_{\mathrm{S}}}{2(G^+_{\mathrm{S}} + G_{\mathrm{N}})}e^{-(L_1+L_2)/\lambda_{\mathrm{N}}}\right\}. \end{aligned} \tag{2.85}$$

We are now ready to proceed to the final step of deriving the nonlocal voltage V_{nl} between F_2 and N_2. Since it is given by $V_{\mathrm{nl}} = \mu_{\mathrm{N}_2}(+\infty) - \mu_{\mathrm{F}_2}(-\infty)$, by using Eq. (2.77) and Eq. (2.82) we find $V_{\mathrm{nl}} = [\mu_{\mathrm{F_2N_2}} + p_{\mathrm{F}_2}\delta\mu_{\mathrm{F}_2}(0)]/e$ which is reduced to $V_{\mathrm{nl}} = -(p_{\mathrm{F}_2}/p_{\mathrm{F}})R_{\mathrm{NF}_i}I^s_{\mathrm{F_2N_2}}$ using Eqs. (2.78) and (2.80a). Here we defined $R_{\mathrm{NF}_i} = p_{\mathrm{F}}R_{\mathrm{F}}/2 + |p_{T_i}|R_{T_i}$ and used $p_{T_i}/|p_{T_i}| = p_{\mathrm{F}_i}/p_{\mathrm{F}}$ implying the same polarization in the ferromagnets and the $\mathrm{N}_i\mathrm{F}_i$ interfaces. Finally, combining Eqs. (2.78), (2.80a), and (2.85), we determine the spin current $I^s_{\mathrm{F_2N_2}}$ as a function of the injection current I to obtain the nonlocal spin resistance,

$$R_{\mathrm{nl}} = \pm\frac{R_{\mathrm{NF}_1}R_{\mathrm{NF}_2}R_0e^{-(L_1+L_2)/\lambda_{\mathrm{N}}}}{R_{\mathrm{NS}_1}R_{\mathrm{NS}_2} - R_0^2e^{-2(L_1+L_2)/\lambda_{\mathrm{N}}}}, \tag{2.86}$$

where $R_0 = G_S^+/[4G_N(G_S^+ + G_N)]$ and $R_{NS_i} = R_N/2 + R_F/2 + R_{T_i} - R_0 e^{-2L_i/\lambda_N}$. The overall sign of R_{nl} depends on whether the ferromagnets are aligned parallel (+) or antiparallel (−).

Equation (2.86), which is the main result of this section, predicts a finite nonlocal resistance generated by a pure spin current injected into a superconductor. The exponential dependence $\propto e^{-(L_1+L_2)/\lambda_N}$ of R_{nl} on the lengths of the normal wires clearly shows that it is due to the spin transport through the structure. In the case of fully polarized ferromagnets, where $|p_{T_i}| = p_F = 1$ and $R_F/2 + R_{T_i} \to \infty$, the result Eq. (2.86) simplifies to $R_{nl} = \pm R_0 e^{-(L_1+L_2)/\lambda_N}$.

A nonloncal spin signal can be observed also in the absence of superconductivity. In case of $G_S^+ \gg G_N$, when the contribution of the superconducting element to the nonlocal signal is negligible, Eq. (2.86) is similar to the result of Ref. [**61**]. The difference in the numerical factors is due to a different geometry of the normal part considered in the FNF spin valve. Since this case corresponds to temperatures above the superconducting transition temperature T_c, our spin valve geometry involves the superconductor as a normal metal. However, we expect the decay lengths of the nonlocal signal within the superconductor to be quite different below and above the transition. At $T \ll T_c$, our results yield $R_{nl} \propto e^{-d/\xi_S}$ since $G_{CAR/EC}$ decay exponentially on the scale ξ_S. On the contrary, at $T > T_c$, the nonlocal resistance should be proportional to e^{-d/λ_S}, where λ_S is the spin diffusion length of the superconductor in the normal state. Typically, λ_S for Al is $\sim 500 - 1000$ nm and ξ_S is $\sim 100 - 300$ nm. Thus, one would expect an abrupt change in the nonlocal resistance when the superconductor undergoes the transition, which may be observed in the experiment similarly as in Ref. [**1**].

The magnitude of the nonlocal resistance induced by the injection of a pure spin current may be estimated from the nonlocal resistance measured in the case of charge current injection. Based on the formalism suggested by Falci *et al.* [**48**], the nonlocal resistance can be written as $R_{\text{nl}}^{\text{NSN}} = (G_{\text{EC}} - G_{\text{CAR}})/G_{\text{AR}}^2$, where the conductance due to AR at a single NS interface $G_{\text{AR}} \gg G_{\text{CAR}}, G_{\text{EC}}$ is assumed to be the same for the both N_iS interfaces. Using the measured $R_{\text{nl}}^{\text{NSN}}$ as well as estimated values of G_{AR} from P. Cadden-Zimansky *et al.* [**3**] yields a rough estimate of $G_{\text{EC}} - G_{\text{CAR}} \sim 0.5\ \Omega^{-1}$. For copper wires with a spin diffusion length $\lambda_{\text{N}} \sim 1\ \mu$m and cross section A_{N} =100×50 nm^2, corresponding to $G_{\text{N}} \approx 0.3\ \Omega^{-1}$, the factor R_0 in Eq. (2.86) would be of the order of 0.5 Ω in this case. If G_{CAR} and G_{EC} are of the same order of magnitude, the nonlocal resistance due to the pure spin current would likely be much larger. As a final remark, it should be noted that this nonlocal signal arises from spin transport at energies far below the superconducting gap. By measuring the nonlocal resistance resulting from charge and spin injection on the same sample, it may be possible to determine the independent contributions due to CAR and EC.

CHAPTER 3

Experimental techniques

In this chapter I will discuss the experimental techniques used to perform the experiments presented in this thesis. As many of the techniques that I used have been developed and utilized by several generations of graduate students in the Mesoscopic Physics Group at Northwestern, I will briefly outline the processes already covered in the thesis of past students [**62, 63, 64, 65, 66, 67, 68, 69, 70**] while providing explanations of new techniques and procedures.

3.1. Sample Fabrication

The first step in the sample fabrication is to prepare the substrate, a polished silicon substrate with 300 nm SiO_2 on top, in a proper size. Typically, the substrate is cut by a hand-held diamond scriber into a size enough to cover 4 identical sets (each set is about 1 cm $\times$ 1 cm consisting of 3 $\times$ 3 pads for photolithography to be performed afterwards) in the photomask and cleaned to get rid of any residual contamination of the surface as follows: (i) Spray DI water over the sample for 1 minute, (ii) Ultrasonicate it in isopropyl alcohol (IPA) for 1 minute, (iii) Ultrasonicate in acetone for 3 minutes, (iv) Ultrasonicate in IPA for 1 minute immediately after step (iii) to remove any acetone residue (v) Blow dry N_2 gas to remove IPA from the surface. At this point, the substrate is ready for the lithography step which mainly consists of photolithography and electron beam lithography.

3.1.1. Photolithography

Photolithography is a prodecure for fabricating large area contact pads, which provide electrical connections between mesoscopic samples contained in the central area $\sim 1000\ \mu\text{m}^2$ and metal wire bonds connected all the way to the room temperature electronics. The method of photolithography used for this thesis was set up by a former graduate student Zhigang Jiang. It consists of a home-made mask aligner including a room for the mask to be placed and a halogen lamp on top whose details can be found in his thesis [**65**]. Here I briefly outline the procedure of photolithography.

(i) Having cleaned the substrate as described above, spincoat it with LOR-7B from MicroChem[1] at a speed of 4000 RPM for 30 seconds on a Headway Research spinner[2] to obtain a nominal thickness of 600 nm. Bake the substrate in an oven at 170 °C for 45 minutes.

(ii) After taking the sample out from the oven, spincoat it with photoresist S1813 from MicroChem at a speed of 3000 RPM for 40 seconds to obtain a nominal thickness of 700 nm and bake the sample at 110 °C for 30 minutes.

(iii) The sample is placed on a photomask in a way that the baked layers are facing the top surface of the photomask and they are put in the home-made metal mask aligner discussed in Ref.[**65**]. The space defined in between the sample and photomask is vacuumed out to ensure a tight contact. Then the sample is exposed to the halogen lamp for 7 minutes.

[1]Microchem Corp., Newton, MA, www.microchem.com.
[2] Headway Research, Inc., Garland, TX, www.headwayresearch.com.

(iv) To develop the exposed parts of the sample, MF-319 photodeveloper is sprayed on the surface of the sample for 55 seconds. Then the developer is washed off with DI water for 20 seconds followed by a dry jet of N_2 gas.

(v) The sample is loaded into an electron gun evaporator built by a former graduate student José Aumentado [**64**], equipped with a setup for *in situ* plasma etching. After the chamber of the evaporator is pumped down to a pressure lower than 1×10^{-6} Torr, the pumping is paused and 40 mTorr of O_2 gas is introduced into the chamber for 20 seconds of high voltage plasma etching to get rid of residue of resists left from earlier steps in the procedure.

(vi) After plasma etching, the chamber is pumped down for 2 minutes before the metal deposition. When the pressure reaches below 1×10^{-6} Torr, 4 nm of Ti of a purity 4N (99.99 %) is deposited first as a sticking layer. 40 nm of Au of a purity 3N5 (99.95 %) is deposited subsequently.

(vii) The sample is taken out of the chamber after waiting for the sample and the system to fully cool and soaked in acetone to lift off the S1813 photoresist for 10 - 15 minutes. The sample is ultrasonicated for 1 minute to ensure the removal of metal flakes sitting on unpatterned parts, and sprayed with acetone and IPA, dried with N_2 gas.

(viii) A separate procedure is required to get rid of LOR-7B layer in which the sample is soaked in 1165 Microposit remover for 10 minutes while maintaining the temperature of the remover between 60 and 70 °C. Afterwards, the sample is rinsed with 1165 remover at room temperature, acetone, and IPA, finally dried with N_2 gas.

3.1.2. Electron beam lithography

Electron beam lithography is performed on the central area of the photolithographic pads to fabricate the core parts of samples on a mesoscopic scale. For the samples designed for the experiments on NS heterostructures including Au and Al, I followed the procedure documented in the thesis of a former graduate student Paul Cadden-Zimansky [**67**], which I will summarize as follows.

(i) Spincoat the sample with 6.5% MMA (methylmetacrylate) from MicroChem at a speed of 3000 RPM for 1 minute to obtain a nominal thickness of 300 nm and bake the sample in an oven at 140 °C for 30 minutes.

(ii) Spincoat the substrate with 3% 950 PMMA (polymethyl methacrylate) from MicroChem at a speed of 3000 RPM for 1 minute to obtain a nominal thickness of 150 nm and bake the sample at 170 °C for 30 minutes.

(iii) The sample is loaded and exposed in the Tescan Mira field emission scanning electron microscope to make features designed in a ElectronScribe[3] file. The detailed description on the procedure of using Tescan Mira can be found in Ref. [**67**].

(iv) To develop the resist, a 1:3 mixture of MIBK (methyl isobutyl ketone) and isopropanol is sprayed on the sample for 1 minute while maintaining the temperature of the developer at 23 °C. Then the sample is rinsed with isopropanol for 20 seconds and dried with N_2 gas.

(v) The metal deposition can be performed in either the electron gun evaporator mentioned before or the thermal evaporator manufactured by Edwards. Inside the chamber of the thermal evaporator, a few pellets of material are placed in a tungsten “boat” connected

[3]Software written by Prof. Venkat Chandrasekhar.

to two electrical leads. As a current flowing through the boat heats up the material beyond its melting point, the material is evaporated. In our group, the thermal evaporator has been exclusively used for nonmagnetic materials such as Au, Al, and Cu in high purities to achieve a long phase coherence length. We used both electron gun evaporator and thermal evaporator to produce the samples used in the experiments presented in this thesis and qualitatively the same results were observed. In both evaporators, Au and Al of a purity 5N (99.999 %) were used and *in situ* plasma etching with O_2 gas was performed prior to the metal deposition. The materials are typically deposited at a pressure $\sim 6 \times 10^{-7}$ Torr. It should be pointed out that no sticking layer is used for the core parts of samples.

(vi) The sample is soaked in acetone for about 5 minutes to lift off MMA/PMMA bilayer. If the lift off process takes longer than expected and the surface of deposited metal does not exhibit any change, it can be helpful to gently heat up acetone to slightly higher than room temperature. However, if the sample already includes some structures consisting of gold, soaking in hot acetone for a while may start to diffuse and deform the shape of the structures. In addition, ultrasonication is not recommended as it may damage the features in nanoscale. Once the lift off is complete, the sample is rinsed with IPA and blown with N_2 gas.

On the other hand, for the samples utilized in the experiments on FS heterostructures including Ni and Al, as both Ni and Al are easily oxidized if they are exposed to air, repeated applications of the procedure outlined above is not suitable to realize a transparent interface between two materials. There are two ways to resolve this issue: i) Performing Ar plasma etching prior to the deposition of the second material to remove the oxide layer. ii) Using so called two-angle shadow mask technique where both materials are deposited without breaking the vacuum of the chamber of the evaporator. As i) is introduced in detail in Ref.

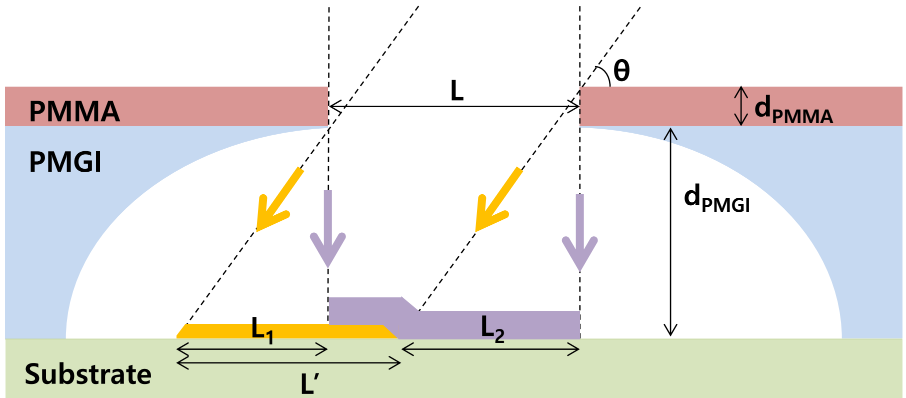

Figure 3.1. Schematic illustration of the two-angle shadow mask technique. The first material (yellow) is deposited at an angle θ followed by the second material (purple) deposited at $\theta = 90°$. Two materials form an overlap of $L - (d_{\mathrm{PMGI}} + d_{\mathrm{PMMA}})/\tan\theta$.

[**65**], here I explain the procedure of ii) which I used to fabricate the samples measured to obtain the data presented in the next chapter.

The principle of the two-angle shadow mask technique is schematically illustrated in Figure 3.1. First of all, it is essential to make a large size undercut as shown in the figure. For that purpose, the first layer of resist is replaced by Polymethylglutarimide (PMGI) SF8 from MicroChem while using 3% 950 PMMA for the second layer as before. As PMGI develops in aqueous base solution, e.g., MF-319 photodeveloper that PMMA is insensitive to, it is possible to develop two layers independently thus control the size of the undercut by varying the development time for PMGI layer [**71**]. After exposing the sample under a scanning electron microscope (SEM) and developing both layers of resists, the first material (yellow) is deposited at an angle θ, as depicted in the figure. By applying a simple trigonometric relation, it is straightforward to observe that the left and right end of the pattern appear at a positions shifted by $L_1 = d_{\mathrm{PMGI}}/\tan\theta$ and $L_2 = (d_{\mathrm{PMGI}} + d_{\mathrm{PMMA}})/\tan\theta$, respectively. Therefore, in case of $\theta = 45°$, the length L' of the deposited material turns out to be d_{PMMA}

shorter than the length of the pattern L, i.e., $L' = L - d_{\mathrm{PMMA}}$. The deposition of the second material (purple) follows at $\theta = 90°$ resulting in an overlap of $L - (d_{\mathrm{PMGI}} + d_{\mathrm{PMMA}})/\tan\theta$ with the first material already deposited. Therefore, in order to finalize the design for a sample in ElectronScribe file which determines important features of the sample such as the shift of position of a material deposited at an angle and the overlap between two materials deposited at different angles, it is necessary to set a desirable thickness of PMGI layer and optimize the speed of spinner to achieve the aimed thickness. Based on the datasheet provided by MicroChem,[4] I made a guess of 1500 RPM to realize the thickness of 1 μm for PMGI layer. Then to confirm the actual thickness, I ran a test using the following procedure.

(i) Spincoat the substrate with PMGI (Polymethylglutarimide) from MicroChem at a speed of 1500 RPM for 1 minute and bake the sample in an oven at 180 °C for 30 minutes.

(ii) Spincoat the sample with 3% 950 PMMA (polymethyl methacrylate) at a speed of 3000 RPM for 1 minute to obtain a nominal thickness of 150 nm and bake the sample at 170 °C for 30 minutes.

(iii) The sample is loaded and exposed in the Tescan Mira field emission scanning electron microscope to make features designed in a ElectronScribe file.

(iv) To develop PMMA, a 1:3 mixture of MIBK (methyl isobutyl ketone) and isopropanol is sprayed on the sample for 1 minute while maintaining the temperature of the developer at 23 °C. Then the sample is rinsed with isopropanol for 20 seconds and dried with N_2 gas.

(v) To develop PMGI, MF-319 photodeveloper is sprayed on the surface of the sample for 55 seconds. Then the developer is washed off by DI water for 20 seconds followed by dry jet of N_2 gas.

[4]Visit microchem.com.

(vi) The metal deposition can be performed in the electron gun evaporator equipped with a rotatable sample stage. Prior to the metal deposition, plasma etching is performed with 40 mTorr of O_2 to remove the residual resist. The sample stage is rotated until the angle θ reaches 45° for the deposition of Au. Then the sample state is rotated back to the original position at $\theta = 90°$ and Al is deposited.

(vii) For the lift off of the metals, the sample is soaked in acetone for about 5 minutes to lift off PMGI/PMMA bilayer. Once the lift off is complete, the sample is rinsed with IPA and blown with N_2 gas. PMGI layer should be removed separately by soaking the sample in 1165 Microposit remover for 10 minutes while maintaining the temperature of the remover between 60 and 70 °C. Afterwards, the sample is rinsed with 1165 remover at room temperature, acetone, and IPA, finally dried with N_2 gas.

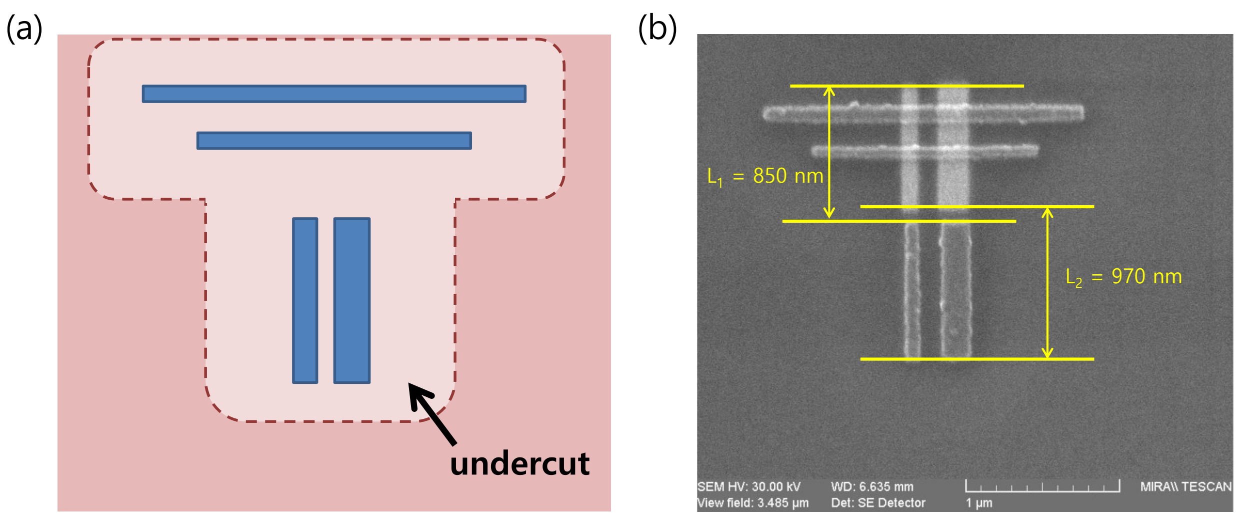

Figure 3.2. (a) Schematic drawing of the test pattern (in blue strips) with expected range of the undercut formed in PMGI layer. (b)Scanning electron microscope (SEM) image after the lift off of the material, Au (bright color) deposited at $\theta = 45°$ and Al (dark color) deposited at $\theta = 90°$.

Figure 3.2 (a) shows schematic drawing of the test pattern. Scanning electron microscope (SEM) image shows the result after the lift off of the metals as shown in (b). The bright color represents Au deposited at $\theta = 45^\circ$ and dark color corresponds to Al deposited at $\theta = 90^\circ$. The top-to-top distance between vertical strips of Au and Al is measured to be $L_1 = 850$ nm, corresponding to the thickness of the PMGI layer, and the bottom-to-bottom distance is measured to be $L_2 = 970$ nm. The difference between L_2 and L_1 is due to the thickness d_{PMMA} of PMMA, as explained above. If one aims to have a thinner/thicker PMGI layer, the procedure shown above can be repeated with higher/lower speed of the spinner until the aimed thickness is achieved.

3.2. Measurement techniques

In this section I describe the techniques used to measure the electrical transport properties of the samples at low temperatures. All of these techniques used to perform the experiments presented here have been utilized over decades by the members of the group, which spans from cryogenic techniques to operate dilution refrigerators to sensitive electrical measurement techniques. The details of these techniques can be found in the thesis of former students of the group [**62, 63, 64, 65, 66, 67, 68, 69, 70**].

3.2.1. Preparation for Cooldown

As we focus on physical phenomena occurring at NS interfaces, it is important to cool down the fabricated sample to liquid nitrogen temperatures as soon as possible in order to avoid degrading of the quality of the interface between Au and Al [**67, 72**]. Here I outline the required steps prior to the cooling down of the sample, which should be conducted without unnecessary delay.

i) After the lift off of the metal in the final layer, the image of the sample needs to be taken in SEM to decide suitable samples for the experiment.

ii) The selected sample is mounted on a homemade sample holder by a silver paste and aluminum wire-bonds are made between pins of the sample holder and photopads of the sample using a wire bonder manufactured by Kulicke and Soffa[5].

iii) The bonded sample is loaded on the sample stage of the fridge and initial check of electrical connections of the sample is performed.

While making wire-bonds and loading the sample on the fridge, one must be careful to avoid burning the nanoscale wires in the sample with static charges. Wearing grounding straps whenever making a contact to the sample, having a humidifier on and keeping it near bonder and refrigerator, and shorting the sample holder containing the bonded sample by inserting it into a metal piece can be helpful to prevent the discharge.

3.2.2. Cyrogenics

All the data presented in this thesis have been obtained in two dilution refrigerators in the group, an older Kelvinox-300 and a newer Kelvinox-MX100 both purchased from Oxford Instruments[6]. Both refrigerators are capable of reaching temperatures as low as 20 mK or below and are equipped with magnets: The Kelvinox-300 has a 12 T superconducting solenoid magnet and Kelvinox-MX100 has two superconducting magnets: a solenoidal magnet that

[5] Kulicke and Soffa Industries, Fort Washington, PA, www.kns.com.
[6] Oxford Instruments, Concord, MA, www.oxford-instruments.com.

can apply a 3 T axial field and a split coil magnet that can apply a 1 T in-plane field. In both refrigerators, the temperature is read by the resistance of RuO_2 thermometer mounted on the mixing chamber plate. In the Kelvinox-300, we used a commercial TRMC2 multi-probe regulator[7] and in the Kelvinox-100, the temperature is read by the "Femtopower" system from Oxford instruments. In order to prevent rf-radiation transmitted through the electrical connection from coupling into the dilution refrigerator and the sample, both fridges have rf-filters on each electrical line at the top, with the cut-off frequency of 5 MHz on the Kelvinox-300 and 800 kHz on the Kelvinox-MX100, respectively. Further information on the dilution refrigerators can be found in the theses of former students [**62, 63, 67**].

3.2.3. AC differential resistance measurement

Most of the data presented in later chapters of this thesis is the change of differential resistance dV/dI of the sample as a response to a change in external parameters such as temperature, dc current bias, or magnetic field. The measurement of this differential resistance is done by a four probe ac lock-in technique. As the details of this technique including circuit diagrams of instruments can be found in theses of earlier members of the group [**62, 63, 64**], here I only provide a brief explanation in the following.

For ac differential resistance measurement, an ac voltage with a low frequency f_{LIA} ($<$ 100 Hz) is sent from a Princeton Applied Research 124A[8] lock-in amplifier (LIA) to the input of either a home-built Adler-Jackson type bridge or a home-built current source with an AD549 chip[9] (See J. Eom's thesis [**62**] for a circuit diagram of the current source).

[7] AIR LIQUIDE, France.
[8] Ametek Princeton Applied Research Oak Ridge, TN, www.princetonappliedresearch.com/index.aspx.
[9] Analog Devices, Norwood, MA, www.analog.com/en/index.html.

In case of the bridge, MΩ resistors convert the ac voltage supplied from LIA into ac current, which flows through the sample and a resistor with variable resistance, called a balance resistor, in parallel. Before making measurements, the phase of the LIA should be adjusted so that the out-of-phase signal is independent of the change in the resistance of the balance resistor. The voltage difference across the sample and the balance resistance R_b, i.e., $V_s - V_b$, is sent to the LIA and the output of LIA is amplified by an instrumentation amplifier, either AD624[10] which has an input impedance of $\sim 10^9$ Ω or INA110[11] which has an input impedance of $\sim 10^{12}$ Ω.

A current source is useful to measure dV/dI as a function of dc current I_{dc}, one of most frequently performed measurements for this thesis. For this measurement, a homemade summer (See J. Eom's thesis [**62**] for a circuit diagram of the summer) is used to sum the ac voltage supplied from the LIA and dc voltage from either Keithley 230 voltage source[12] or HP 3345A function generator[13], as schematically presented in Figure 3.3. The output of the summer goes to the input of a home-built current source employing an AD549[14] chip with nominal input impedance of 10^{15} Ω which generates the sum of ac and dc currents $I_{\mathrm{ac}} + I_{\mathrm{dc}}$ sourced to the sample. The value of I_{dc} is read by probing the voltage across the sense resistor R_{sens} of the current source. The voltage across the sample is given by

(3.1)

$$V(I_{\mathrm{dc}} + I_{\mathrm{ac}}\sin(\omega_{\mathrm{LIA}}t)) = V(I_{\mathrm{dc}}) + \left[\frac{dV}{dI}\right]_{I_{\mathrm{dc}}} I_{\mathrm{ac}}\sin(\omega_{\mathrm{LIA}}t) + \frac{1}{2}\left[\frac{d^2V}{dI^2}\right]_{I_{\mathrm{dc}}} (I_{\mathrm{ac}}\sin(\omega_{\mathrm{LIA}}t))^2 + \cdots$$

[10] Analog Devices, Norwood, MA, www.analog.com/en/index.html.
[11] Texas Instruments, Inc., Dallas, TX, www.ti.com.
[12] Keithley Instruments Inc., Cleveland, OH, www.keithley.com.
[13] Keysight Technologies, Inc., Santa Rosa, CA, www.keysight.com.
[14] Analog Devices, Norwood, MA, www.analog.com/en/index.html.

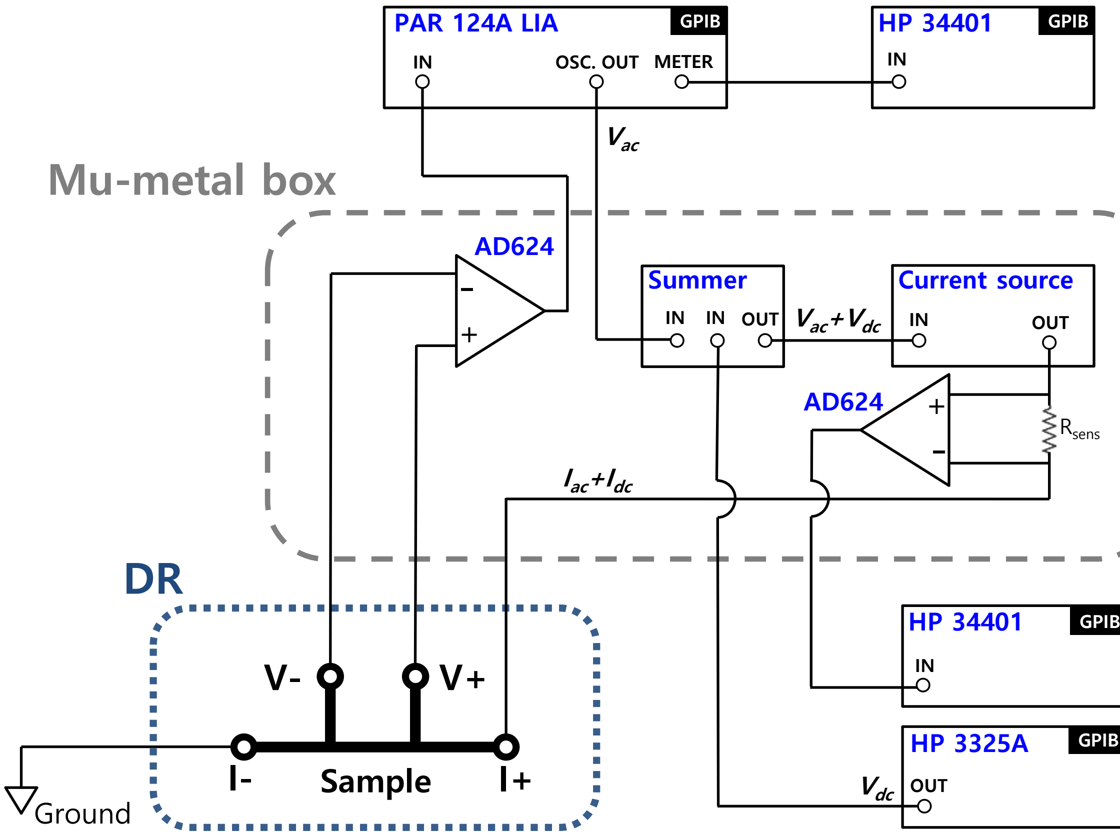

Figure 3.3. Schematic diagram for a typical measurement setup used for dV/dI vs $I_{\rm dc}$ measurements. Home-built instruments including a current source, summer, instrumentation amplifier are placed inside a mu-metal shielding box.

where $\omega_{\rm LIA} = 2\pi f_{\rm LIA}$ and is amplified by an instrumentation amplifier and probed by HP 34401A digital multimeter[15]. As the LIA picks up the signal at the same frequency as the sourced ac voltage from the LIA oscillator for the differential resistance dV/dI, the measured voltage corresponds to the differential resistance at dc bias $I_{\rm dc}$ multiplied by the amplitude of ac current $I_{\rm ac}$ and the gain of the instrumentation amplifier $G_{\rm inst}$. In this way, dc current dependence of the differential resistance dV/dI can be measured as the dc voltage from the voltage source is swept to vary the dc current $I_{\rm dc}$ applied to the sample.

[15]Keysight Technologies, Inc., Santa Rosa, CA, www.keysight.com.

Before making measurements, the magnitude of the background noise and its spectral distribution should be characterized by using an SR760 spectrum analyzer[16]. In order to minimize the noise that may add to the noise from the sample, the ground of the dilution refrigerator and all the measurement instruments installed on measurement racks are electrically connected by copper straps leaded to a single earth ground outside. In addition, all the home-made instruments including the bridge, the current source, the summer, and the instrumentation amplifier are powered by rechargeable batteries not by power lines to remove possible line noise and placed in a mu-metal shielded box as depicted in Figure 3.3. Then a nearly flat spectral distribution of the noise is observed with a typical magnitude measured to be 6-8 $\mathrm{nV_{rms}}/\sqrt{\mathrm{Hz}}$.

In order to measure the differential resistance dV/dI as a function of an external magnetic field B, a dc current flowing through the magnet is controlled by a power supply such as Kepco BOP 20-20M bipolar power supply[17] which is capable of sourcing 20 A or Kepco BOP 100-1M[18] bipolar power supply which is capable of sourcing 1 A, depending on the range of magnetic field needed to be applied in the experiment. As we operate the magnets, a finite amount of noise is inevitably introduced by additional instruments on the measurement set up, in particular, the KEPCO power supply. Aiming to observe a small change in the differential resistance dV/dI in the order of a few tens of mΩ, a transformer is used to enhance the signal to noise ratio. The output of the bridge is sent to the input of a home-made transformer box. A typical transformer consists of two sets of coils, primary and secondary. Depending on the number of windings of primary and secondary coils, the transformer can either increase (step-up transformer) or decrease (step-down transformer) the voltage on its

[16]Stanford Research Systems Inc., Sunnyvale, CA, www.thinksrs.com.
[17]Kepco, Inc., Flushing, NY, www.kepcopower.com.
[18]Kepco, Inc., Flushing, NY, www.kepcopower.com.

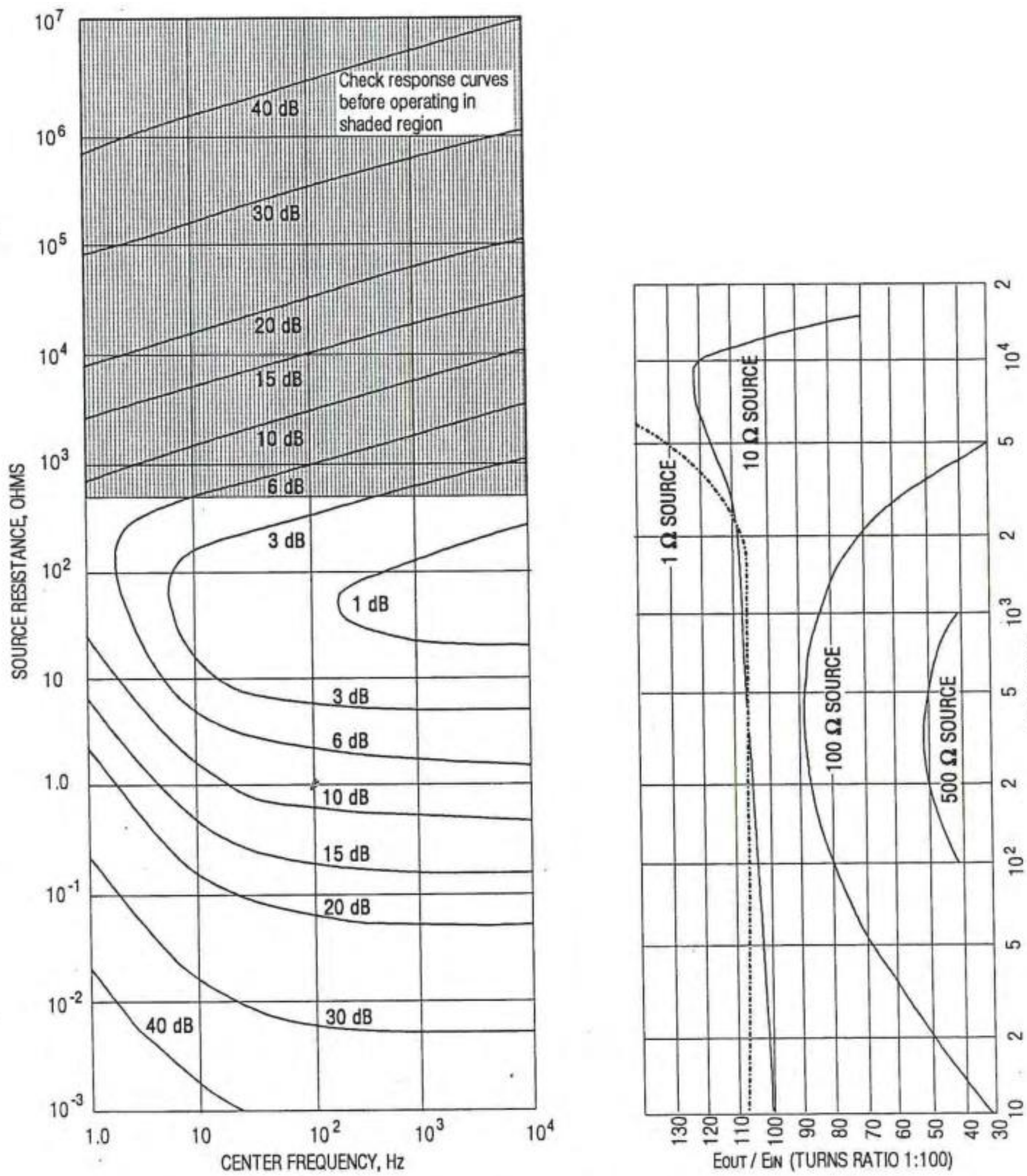

Figure 3.4. Typical noise figure and amplitude transfer curves for pre-amplifier (model 116) operating in transformer mode. Figure taken from PAR 124A manual.

secondary coil. Therefore, a step-up transformer essentially acts as an additional amplifier and it enhances the signal to noise ratio (SNR) via "impedance matching" between the output impedance of the signal coming from the sample and the input impedance of the next amplifier stage AD624 where the gain G_{tr} of the transformer is dependent on the frequency f_{LIA} at the LIA. For example, the noise figure of pre-amplifier 116 utilizing a transformer embedded in PAR 124A is shown in Figure 3.4 to present the dependence of the gain on the frequency. It should be noted that a "sweet spot" in the frequency domain for the maximum gain is dependent on the source resistance.

For the measurements, a home-built box UTC A-11 transformer[19] was used along with the bridge for the impedance matching of a sample and AD624 instrumentation amplifier. UTC A-11 is a step-up transformer where the resistance of primary coil is $R_P = 500\ \Omega$ and secondary coil is $R_S = 50\ \mathrm{k}\Omega$ which provides the turn ratio $n = \sqrt{R_S/R_P} = 100$. As the gain G_{tr} of the transformer is dependent on the frequency as mentioned above, it should be calculated experimentally by comparing the voltages measured by the LIA at two different modes: direct (D) mode and transformer (T) mode. At D mode, the output of the bridge bypasses the transformer and results in V_D after the amplification by the AD624 while the the output goes through the transformer at T mode and results in V_T. By taking the ratio between V_T and V_D, we obtain the gain $G_{\mathrm{tr}} = V_T/V_D$ of the transformer where the maximum gain is achieved at $f_{\mathrm{LIA}} \sim 100$ Hz. Figure 3.5 shows the dV/dI of a sample as a function of an external magnetic field B measured without a transformer at LIA frequency $f_{\mathrm{LIA}} = 40.5$ Hz (red trace) and with a transformer at $f_{\mathrm{LIA}} = 103$ Hz (black trace) where the gain is obtained as $G_{\mathrm{tr}} = 30$. A clear enhancement of the signal to noise ratio can be observed demonstrating that the transformer plays a crucial role in the measurements.

[19]United Transformer Corporation, New York, NY.

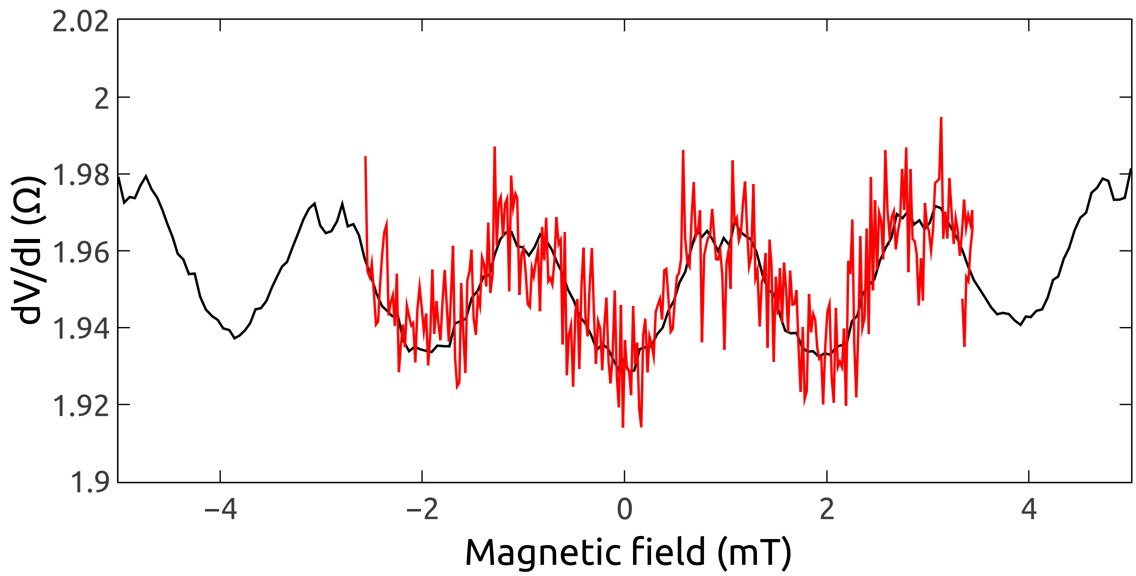

Figure 3.5. dV/dI as a function of an external magnetic field B. Red trace represents the result obtained without a transformer at LIA frequency of 40.5 Hz while the black trace is with a transformer at LIA frequency of 103 Hz (black trace).

The data are taken by utilizing the home-made data acquisition program[20] which reads and controls all the commercial instruments via GPIB. The sweep rate of an input instrument, such as an HP 3325A synthesizer to provide a dc voltage supplying the dc current I_{dc} for the dV/dI vs I_{dc} measurement or a KEPCO power supply to provide the current controlling the magnet for the dV/dI vs I_{dc} measurement, should be determined by considering the time constant t_c at LIA. The time constant t_c comes from the output filter installed in LIA and is a controllable parameter which should be set to provide an optimal balance between responsiveness and stability of the measurement. For a single data point, the output from LIA should be averaged over a time corresponding to at least three times of the t_c.

[20]Written by Prof. Venkat Chandrasekhar

CHAPTER 4

Experimental results: Nonlocal correlations mediated by proximity-coupled normal metal

In this chapter, I present the experimental results of the measurements performed to study the nonlocal correlations mediated by a proximity-coupled normal metal. I will start with experiments on samples in a linear geometry, followed by the results obtained on samples including a loop which forms a SQUID (superconducting quantum interference device). Here I provide the experimental data along with discussion based on the numerical calculation, which provides insights into the physics behind the observed results.

4.1. Linear geometry

In order to experimentally investigate the nonlocal correlations mediated by a proximity-coupled normal metal, we fabricated a sample consisting of a normal metal (N) and a superconductor (S) as shown in Figure 4.1 (a). Au of a purity 5N (99.999%) and Al of 4N (99.99%) were used as the normal metal and the superconductor, respectively. The left part of the sample forms a NSN structure where two normal wires are connected by a superconductor. This structure of the sample is analogous to the ones studied in Ref. [**3**]. On the other hand, the right part of the sample, the main sample, has a part of superconductor replaced by a proximity-coupled normal metal. We decided the length L of the normal metal wire between the two superconductors so that the two superconductors are Josephson-coupled in the temperature range of interest in the experiment. Due to the nature of the samples

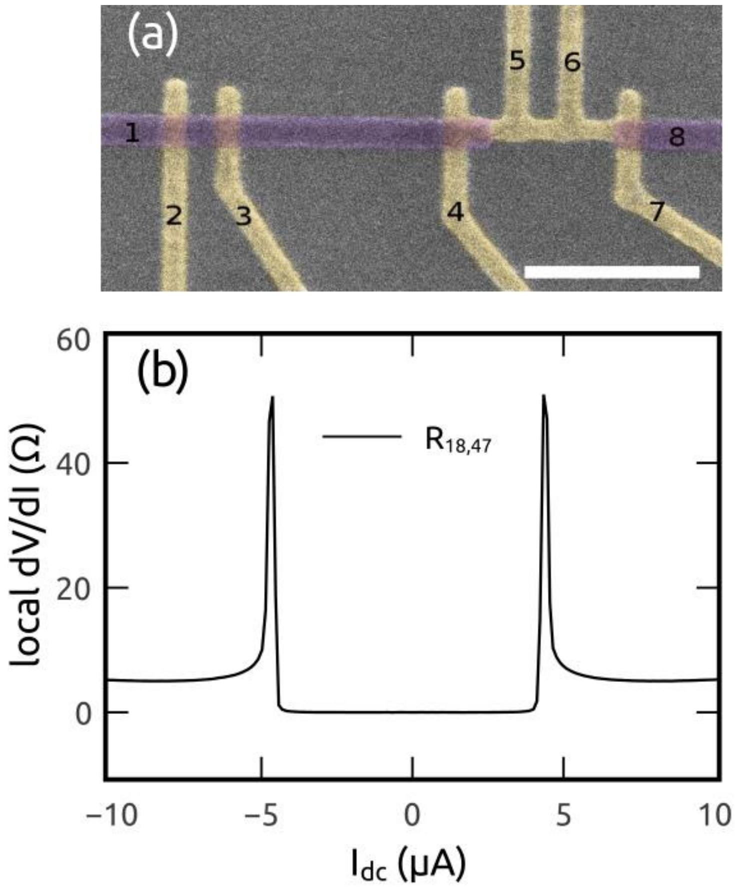

Figure 4.1. (a) False color scanning electron microscope (SEM) image of the sample consisting of a normal metal (Au: yellow) and a superconductor (Al: purple). The numbers denote the contacts used for four-terminal differential resistance measurements. The size bar is 500 nm. (b) The local differential resistance as a function of bias current I_{dc} measured at 24 mK.

including multiple wires, the notation $R_{ij,kl} = dV_{kl}/dI_{ij}$ will be used to denote the 4-terminal differential resistance with $k \rightarrow$ I+, $l \rightarrow$ I-, $i \rightarrow$ V+, and $j \rightarrow$ V-. For example, Figure 4.1 (b) shows the local differential resistance of the main sample $R_{18,47}$ as a function of dc current I_{dc}. The notation denotes that the differential resistance is measured by biasing a current from a superconducting lead (labelled as "1") to the other suerperconducting lead ("8") and by probing the voltage between two normal leads ("4" and "7"). The bias current consists of a small ac excitation current $I_{\mathrm{ac}} \sim 50$ nA and dc current I_{dc} which is swept in the range of ± 10 μA. The results show that at $T = 24$ mK the differential resistance $R_{18,47}$ remains zero within a finite range of the dc current I_{dc} demonstrating that a finite amount of dissipationless supercurrent I_s can flow through the proximity-coupled normal metal. Therefore two superconductors are Josephson-coupled at this temperature with the maximum amount of the supercurrent, called the critical current $I_c \sim 3.6$ μA for this sample. At I_{dc} beyond the critical current, the differential resistance presents a sharp peak and then relaxes to its normal state value $R_N = 4.6$ Ω.

Having confirmed the Josephson-coupling between two superconductors, we move onto the nonlocal differential resistance. Figure 4.2 shows the results of the nonlocal differential resistance as a function of dc bias current I_{dc} on different parts of the sample. Before discussing the results obtained from the main sample, let us first take a look at the results from the left part of the sample as shown in (a). The nonlocal differential resistance $R_{21,38}$ was measured by injecting both ac and dc currents from a normal metal lead ("2") into a superconducting lead ("1") and by probing the voltage between another normal metal lead ("3") and another superconducting lead ("8"). It should be noted that the normal metal lead used to measure the voltage is spatially separated about 200 nm from the one used for the injection of the current. The result shows a finite resistance $R_{21,38} \sim 20$ mΩ at $I_{\mathrm{dc}} = 0$ as shown in the inset, which is consistent with the result reported in Ref. [**3**]. This finite zero-bias nonlocal differential resistance is attributed to the two processes CAR and EC, as introduced earlier in Chapter 2. These two processes give rise to opposite contributions to the zero-bias nonlocal differential resistance in case of injection of the charge current and additive contributions in case of injection of the spin current.

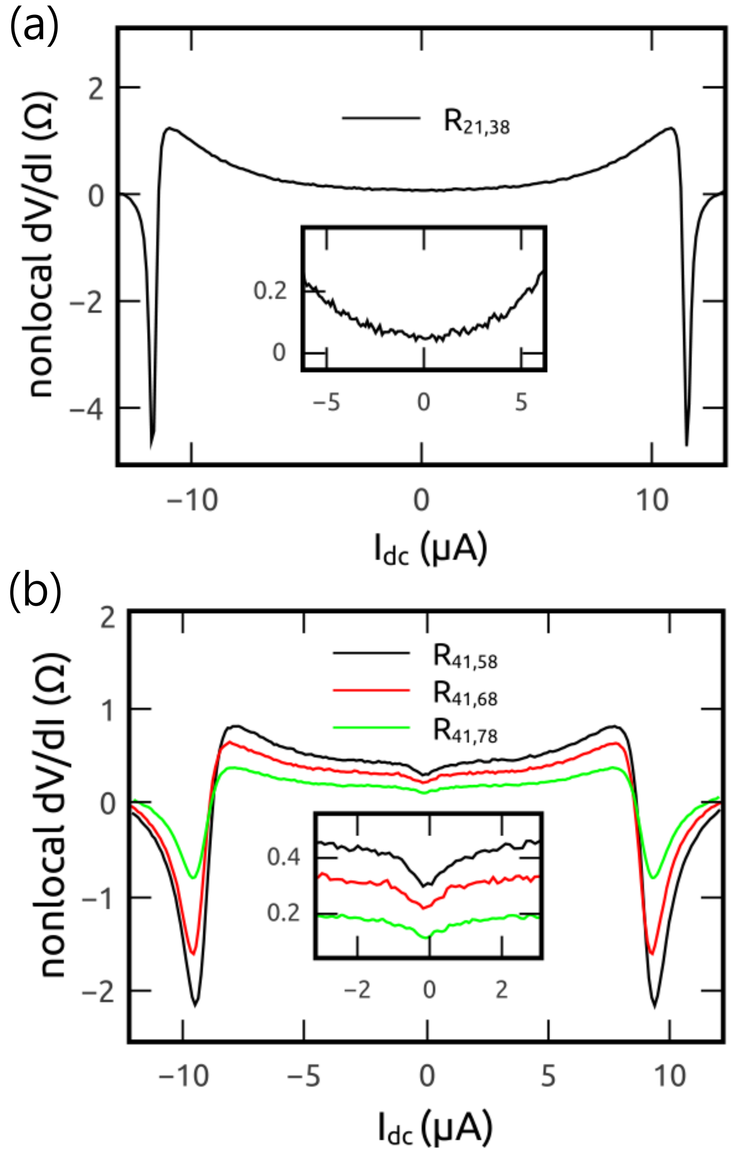

Figure 4.2. Nonlocal differential resistance of (a) the left part (b) the right part of the sample shown in the previous figure as a function of I_{dc}. Inset: Expanded view of the zero bias region. All measurements shown here were performed at 24 mK.

As I_{dc} increases, the differential resistance gradually increases until it shows a peak at $|I_{\mathrm{dc}}| \sim 12$ μA followed by a drop to a negative value. The origin of such a dependence is known as charge imbalance (CI), which occurs if one branch of the quasiparticle spectrum, either an "electron-like" or a "hole-like" quasiparticle, is more populated than the other [**52, 53, 73**]. As CI is attributed to the nonequilibrium distribution of quasiparticles, it is more pronounced at high temperatures near the critical temperature T_c of the superconductor or under the injection of large bias current I_{dc}. The set of a peak and a dip appears as I_{dc} exceeds the critical current of superconducting wire. Since no nonlocal voltage is observed above this value of I_{dc}, the integration of the curve over the entire range of I_{dc} becomes zero. In addition to the fact that the effects of CAR/EC and CI appear in different ranges of I_{dc}, they also exhibit different dependences on the distance between two normal metal N_1 and N_2. Ref. [**3**] demonstrated that while the zero bias resistance decays on the order of a few hundred nm, in the order of the coherence length ξ_S, the peak resistance decays on the order of micron as CI diffuses into the superconductor and the quasiparticles go through recombination processes with their counterpart quasiparticles to relax into the condensate as pairs.

Figure 4.2 (b) shows the result on the main sample. The nonlocal differential resistance $R_{41,\mathrm{i}8}$ ($i = 5, 6, 7$) is measured by injecting a current from a normal metal lead ("4") into a superconducting lead ("1") and probing the voltage between another normal metal ("i") and the other superconducting lead ("8"). The overall shape of the curves is very similar to that of the curve in (a). A finite positive differential resistance is observed at $I_{\mathrm{dc}} = 0$, and a peak appears at $|I_{\mathrm{dc}}| \sim 8\ \mu\mathrm{A}$, followed by a drop to a negative value at higher $|I_{\mathrm{dc}}|$. Furthermore, the nonlocal differential resistance also decreases as the distance of the $V+$ voltage lead ("i") from the lead used for the injection of current ("4") increases. However, there is a clear distinction between plots in (a) and (b): There is a small dip at $I_{\mathrm{dc}} = 0$ in the nonlocal differential resistance in (b), which is absent in the NSN structures including the one presented in (a). As can be clearly seen in the inset, the zero-bias dip exists in all three different measurement configurations.

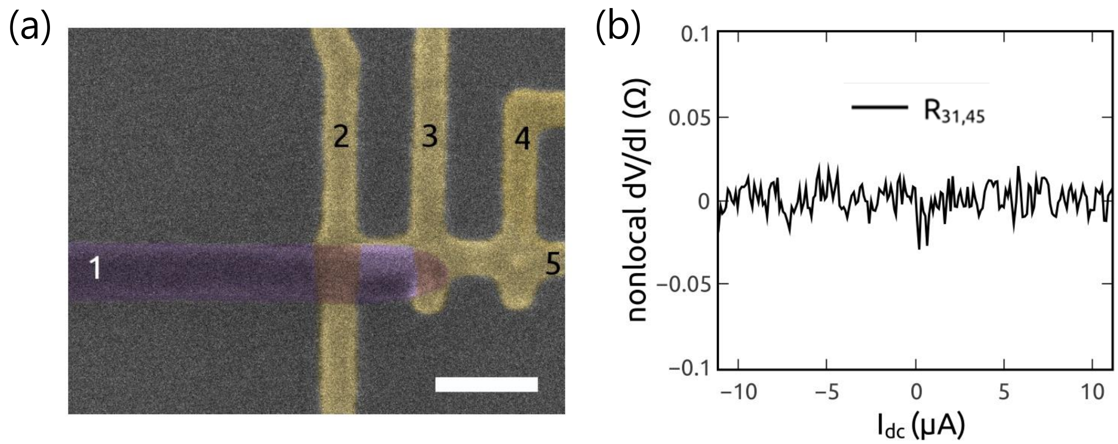

Figure 4.3. (a) False color scanning electron microscope (SEM) image of control sample with no second superconductor. Size bar is 200 nm. (b) The nonlocal differential resistance measured at 24 mK. There is no nonlocal signal in the absence of the second superconductor.

In order to confirm that the nonlocal resistance is observed only if there is Josephson-coupling between two superconductors, the nonlocal differential resistance has been measured on a control sample that has been fabricated at the same time with the sample shown above. Figure 4.3 shows the SEM image of the sample which does not involve the second superconducting contact. The result shows that the nonlocal resistance is zero regardless of the value of I_{dc} demonstrating that the presence of the Josephson-coupling between two superconductors is essential to see the effect.

We fabricated a different set of samples for further investigations. In order to perform a more detailed examination of the length dependence of the nonlocal differential resistance in this configuration, we designed devices such that they include more normal leads extended from the proximity-coupled normal metal. An image of one of these devices is shown in Figure 4.4 (a). For this sample, the electronic diffusion coefficient of Au is $D = (1/3)v_F l = 110$

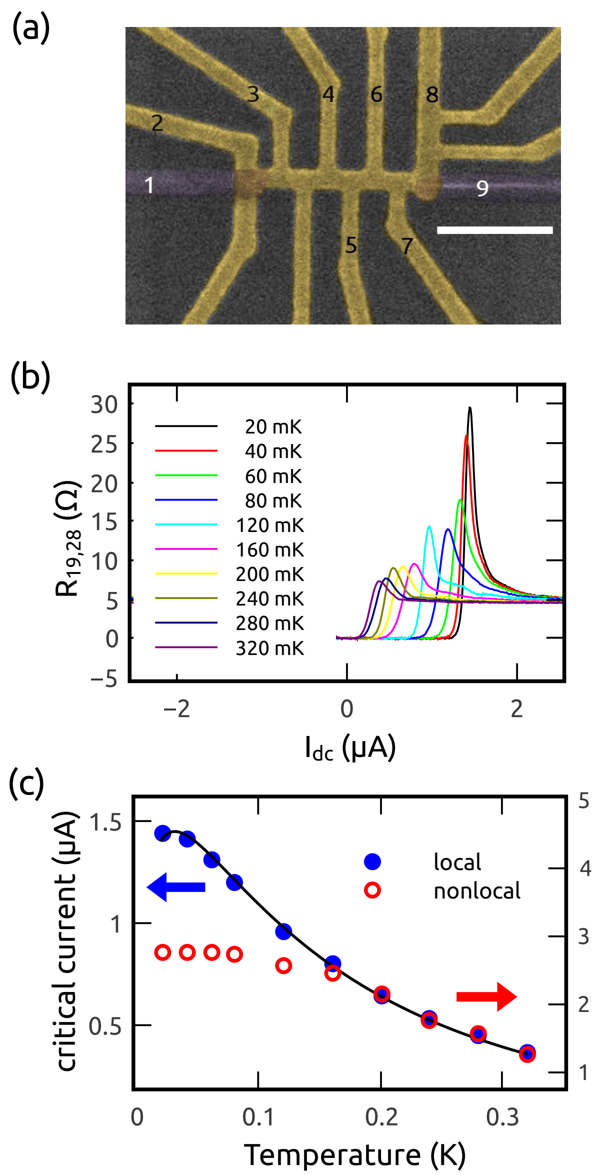

Figure 4.4. (a) False color scanning electron microscope (SEM) image of the sample consisting of Au (yellow) and Al (purple). The size bar is 500 nm. (b) The local differential resistance $R_{19,28}$ as a function of bias current I_{dc} at various temperatures. (c) Temperature dependence of the local and the nonlocal critical currents. Black solid line shows a fit to the expected temperature dependence for a SNS junction in the long junction limit [**42**]. See the text for the definition of the nonlocal critical current.

cm^2/s, as determined from the resistance of the normal metal wires above the measured critical temperature $T_c \sim 1.15$ K of the Al (here v_F is the Fermi velocity and l is the elastic scattering length in Au). The distance $L = 0.75$ μm between the two NS interfaces gives the Thouless energy $E_T = \hbar D/L^2$ of 11.7 μeV, with a corresponding Thouless length $L_T = \sqrt{\hbar D/k_B T} = 293/\sqrt{T}$ nm. This corresponds well with the fact that a finite supercurrent was observed below $T \sim 0.7$ K. Figure 4.4 (b) shows the local differential resistance $R_{19,28}$ as a function of dc bias current I_{dc} at various temperatures between 20 mK and 320 mK. From this set of measurements, temperature dependence of the critical current I_c was found, shown as blue circles in Figure 4.4 (c), where I_c is defined as the position of the peak in the plot in (b). The temperature dependence of the critical current I_c can be fit to a function $I_c = BT^{3/2}\exp(-A/L_T)$ (where A and B are constants) which is expected to be valid for a SNS junction in the long junction limit ($\Delta \gg E_T$) [**42**]. While the overall fit is quite good as shown in Figure 4.4 (c), I_c at the base temperature is much smaller than the expected value $I_{c0} = 10.82 E_c/eR_N$ from the theory presented in Ref. [**42**]. For our sample, $eR_N I_{c0}/E_c \sim 0.56$ with $R_N = 4.56$ Ω. This discrepancy may stem from the difference in the geometry of the samples: In our sample, mutiple normal metal wires extended from normal reservoirs are connected to the proximity-coupled normal metal wire embedded between two superconductors while samples in a simple SNS junction structure were measured in Ref. [**42**]. Results of numerical calculations presented in Chapter 2 show that the critical current I_c of SNS junction is reduced in the geometries similar to our sample used in the experiment and the magnitude of the reduction is enhanced as the number of normal metal wires connected to the proximity-coupled normal metal wire is increased. In addition, a deviation from the perfect transparency of the interfaces also contributes to the amplitude of I_c by lowering it from the theoretical value based on the assumption of perfect NS interfaces.

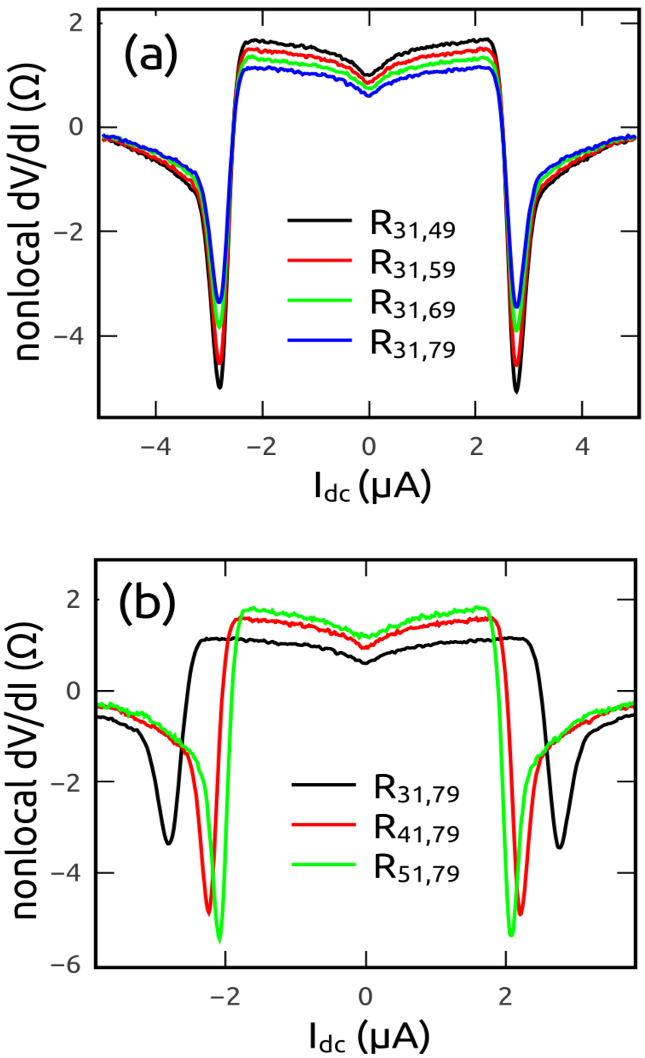

Figure 4.5. (a) Nonlocal differential resistances as a function of dc bias current for 4 nonlocal configurations, $R_{31,49}$, $R_{31,59}$, $R_{31,69}$ and $R_{31,79}$, the current injection lead remain the same. (b) Nonlocal differential resistances $R_{31,79}$, $R_{41,79}$ and $R_{51,79}$, where the current injection lead is changed, but the voltage leads remain the same. All the measurements shown here were performed at 20 mK.

Let us now discuss the nonlocal measurement. Figure 4.5 (a) shows the nonlocal differential resistance $R_{31,\mathrm{i}9}$ ($i = 4, 5, 6, 7$) as a function of dc bias current I_{dc} at 20 mK. The overall shape of the resulting traces is similar to what was observed in the first sample, shown in Figure 4.1. At $I_{\mathrm{dc}} = 0$, nonlocal differential resistance is finite and grows with I_{dc} resulting in a peak at a finite current of 2.3 μA, followed by a sharp drop to negative values before it goes to zero at high bias. The nonlocal differential resistance also decreases as the distance of the V+ lead from the current path increases. Finally, there is a sharp dip near $I_{\mathrm{dc}} = 0$ that is not present in NSN samples. A similar trace is observed if the normal metal lead used to inject the current is changed while the leads for probing the voltage stay the same ("7" and "9"). Figure 4.5 (b) shows these data where the magnitude of the nonlocal differential resistance increases with decreasing distance from the V+ probe to the current path, as before. However, unlike the data in (a), the position of the negative resistance dips also changes.

In order to trace the temperature dependence of the zero bias nonlocal differential resistance that we are interested in, we performed a continuous sweep of the temperature while measuring zero bias differential resistance for the first three configurations, $R_{31,49}$, $R_{31,59}$, and $R_{31,69}$ shown in Figure 4.5 (a). The results are shown in Figure 4.6: the nonlocal differential resistance is essentially zero above 0.8 K and increases below this temperature. This increase is related to the establishment of Josephson coupling between the two superconductors, which is essential to observe the nonlocal differential resistance, as explained before. While the exact mechanism for the gradual increase of the resistance below 0.8 K is not clear, it should be mentioned that this increase has nothing to do with the reentrant behavior of the resistance of the proximity-coupled normal metal introduced earlier. For the rest of the thesis, I will focus on the temperature below 0.3 K where the Josephson-coupling is fully established. The decrease in resistance in this range of temperature is associated with the development of the dip observed in the nonlocal dV/dI at low temperatures, which is our main interest in the experiment.

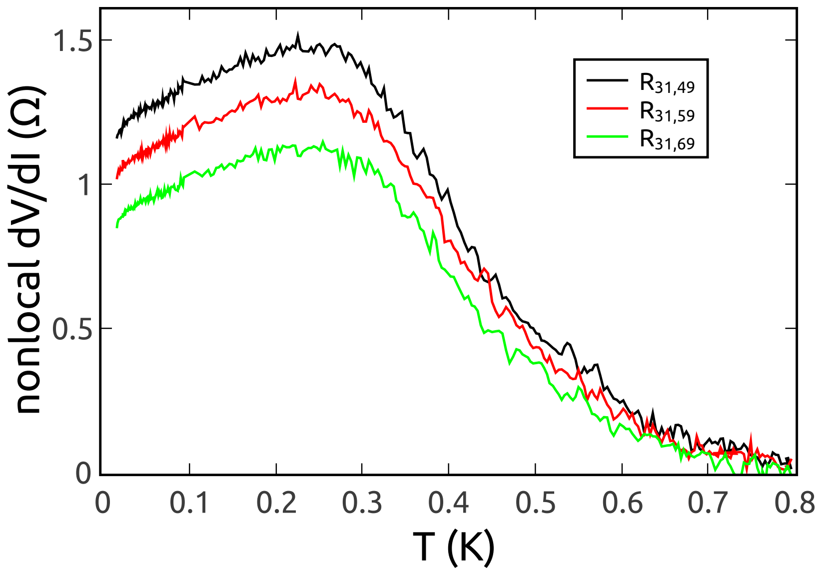

Figure 4.6. Temperature dependence of the zero bias nonlocal resistance of the main sample shown in Figure 4.4.

Let us first attempt to qualitatively understand the origin of nonlocal differential resistance observed in samples measured by other groups. An earlier experiment by Crosser [**45**] provides a simple explanation on the origin of nonlocal differential resistance in a sample with a similar geometry. They fabricated a 3-terminal device which consists of SNS sample with an extra "dangling" normal metal wire extended from the proximity-coupled normal metal and connected to a normal reservoir, as shown in Figure 4.7 (a). The resistances R_1, R_2, and R_N are labelled for different sections of normal metal wires in the sample. They measured the resistance R between the normal reservoir N and one of superconducting reservoirs S_1 by sending a quasiparticle current I_{qp} from N to the grounded S_1 while leaving the other superconducting reservoir S_2 electrically floating. Although one might think that the resistance would be simply $R = R_1 + R_N$, it turned out to be a different value due to the separation of the injected quasiparticle current I_{qp}: I_{qp1} flowing to S_1 and I_{qp2} flowing to S_2. The separation occurs as the voltages at S_1 and S_2 are maintained to be the same due to the Josephson coupling between them. Hence the voltages at both S_1 and S_2 are zero if either of the two superconductors is grounded, which effectively makes the sections with resistance R_1 and R_2 form a parallel circuit and results in $R = R_N + R_1R_2/(R_1 + R_2)$. As a fraction of the current $I_{qp2} = I_{qp}R_1/(R_1 + R_2)$ flows to S_2, an electrically floating reservoir, there should be a counter-flowing supercurrent that makes the total current into S_2 zero. The supercurrent can be generated by a finite phase difference $\Delta\phi$ between S_1 and S_2 while the maximum supercurrent is limited by the critical current I_c of the SNS junction, I_c^{SNS}. Therefore, the separation of the injected current can be sustained until I_{qp2} reaches I_c^{SNS}, which results in the maximum quasiparticle current $I_c^{NS_1} = I_c^{SNS}(R_1 + R_2)/R_1$. Beyond this maximum value of $I_{qp} = I_c^{NS_1}$, the resistance between N and S_1 becomes $R_1 + R_N$ as separation of the injected current can no longer be sustained, as shown in Figure 4.7 (b).

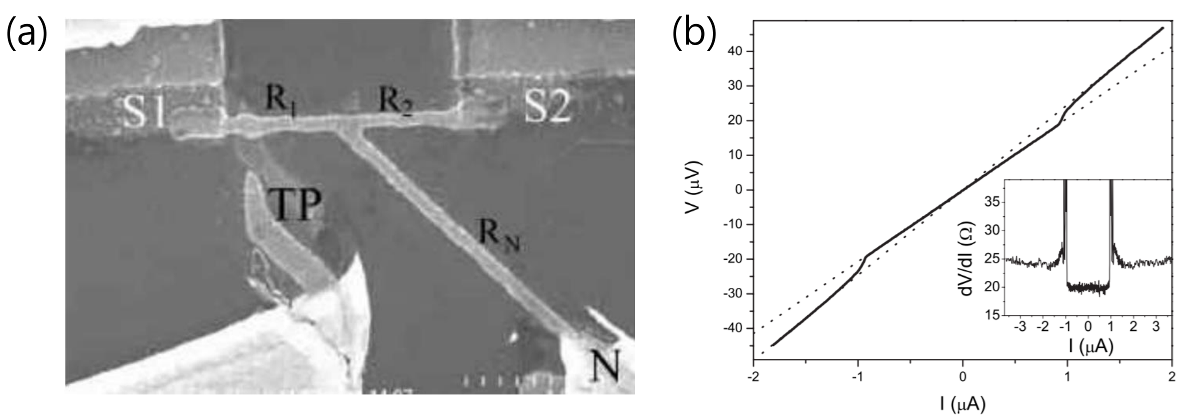

Figure 4.7. (a) Scanning Electron Microscope (SEM) image of sample studied in Ref. [**45**]. The sample consists of two superconducting reservoirs, labeled S1 and S2, normal reservoir labeled N, and a tunnel probe, labeled TP. (b) Voltage versus current measured between reservoir N and S1 with S2 floating. Dotted lines represent slopes of 20.7 and 24.6 Ω corresponding to the resistances R in the text and $R_N + R_1$, respectively. Inset: Differential resistance as a function of current in the same measurement configuration. Figures are taken from Ref. [**45**].

A similar discussion can be made to understand the traces shown in Figure 4.5: For example, injecting a quasiparticle current $I_{\rm qp}$ from a normal metal lead ("3") to a superconducting lead ("1") results in the separation of the current into $I_{\rm qp1}$ flowing to ("1") and $I_{\rm qp2}$ flowing to ("9"). Therefore, $I_{\rm qp2}$ gives rise to a finite voltage drop across the proximity-coupled normal metal which can be probed by measuring the voltage between one of the normal metal leads ("i = 4, 5, 6, 7") and the superconducting lead ("9"). This provides a qualitative explanation of the origin of a finite differential resistance in nonlocal measurements. Meanwhile, $I_{\rm qp2}$ induces a counter-flowing supercurrent between the two superconductors and results in a negative differential resistance dip where it exceeds the critical current of the SNS junction. We denote the value of $I_{\rm qp}$ that results in the dip in the nonlocal measurement configuration as the nonlocal critical current I_c'. The temperature dependence of I_c' is plotted in Figure 4.4 (c) along with the local critical current I_c. With a proper scaling factor, I_c and I_c' can be placed on top of each other at relatively high temperatures over 150 mK while a clear deviation is observed at lower temperatures, consistent with the observation made in Ref. [**45**]. By using a tunnel contact on the normal metal between two superconductors as shown in Figure 4.7, they demonstrated that the deviation at low temperatures occurs as the critical current I_c of the SNS junction is reduced due to a finite voltage applied to the proximity-coupled normal metal as a finite dc current is applied from the normal reservoir.

The change in nonlocal critical current I_c' as we change the path of quasiparticle current can be easily understood from this simple model. As the path changes, the fraction of the injected current that flows into the floating superconducting lead which gives rise to a counter-flowing supercurrent changes. Therefore, the magnitude of the injected current where the negative resistance dips appears is modified accordingly. To be more specific, as the normal metal lead for the injection of the current is changed as "3" $\rightarrow$ "4" $\rightarrow$ "5" in our measurements, the fraction of the current flowing into "9" that needs to be cancelled by the supercurrent increases. Then it becomes easier to reach the critical current of the SNS junction, which explains the reduction of I_c' where the negative resistance dips appear in Figure 4.5 (b).

Based on the discussion so far, it seems that the experiment by Crosser and the analysis therein provide a good qualitative explanation of the origin of a finite resistance and its overall dependence on the magnitude of the injected quasiparticle current in our nonlocal measurement configuration. However, it is still far from a full explanation since i) a detailed study and analysis of the bias dependence that lead us to observe the appearance of the central dip near zero bias is missing in Ref. [**45**]; and ii) the central dip shows qualitatively different behavior from the nonlocal differential resistance at finite bias as a function of distance and temperature. These differences will be discussed in detail below.

As briefly mentioned before, earlier nonlocal NSN experiments [**67**] revealed that the zero bias differential resistance and the peak at finite I_{dc} decayed as the distance from the current injection lead is increased, but with different length scales: While the zero bias resistance due to CAR and EC decayed exponentially with ξ_S, the peak associated with charge imbalance was found to decay almost linearly with the charge imbalance length λ_Q^* as the quasiparticle potential μ_{qp} has the spatial dependence $\mu_{qp} = e\lambda_{Q^*}\rho_S I \tanh(x/\lambda_{Q^*})$, where x is the distance from the current lead and ρ_S is the resistance per unit length of the superconducting wire in its normal state. In our experiment, zero bias resistance and the peak resistance also scale differently with distance. Figure 4.8 (a) shows the curves of Figure 4.5 (a) scaled along the y-axis so that their peaks at ± 2.3 μA match. With this scaling, the curves match over most of the range of current, except near zero bias. This clearly shows that the zero bias resistance and the finite bias resistance scale differently with length, as was found for the

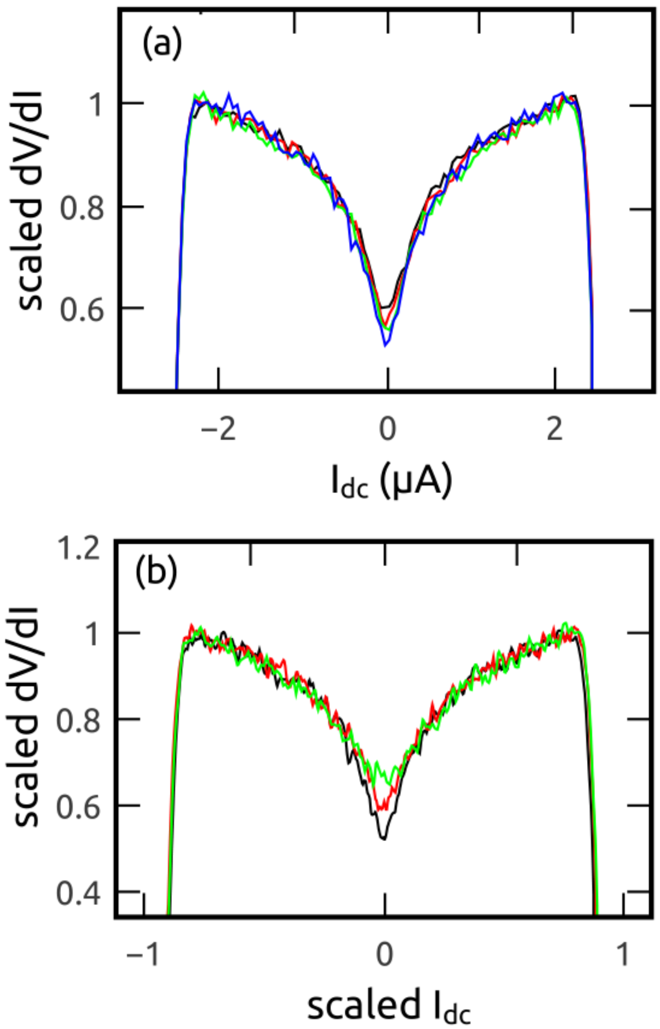

Figure 4.8. (a) The nonlocal differential resistance in Figure 4.5 (a), $R_{31,49}$, $R_{31,59}$, $R_{31,69}$ and $R_{31,79}$, scaled so that their normalized peaks at ± 2.3 μA match. (b) The nonlocal differential resistance in Figure 4.5 (b), $R_{31,79}$, $R_{41,79}$, and $R_{51,79}$ with both x and y axes scaled as described in the text.

NSN samples. In addition, Figure 4.8 (b) shows the curves of Figure 4.5 (b) with x-axis scaled so that the position of the dips match, and the y-axis independently scaled so that the magnitude of the resistance peaks at finite bias match. Again, this demonstrates that the resistance dip at zero bias scales differently with length in comparison to the finite bias part of the differential resistance. The difference in the distance dependence between the zero bias resistance and the resistance peak suggests that their origin may stem from something fundamentally different, as in the case of CAR/EC and CI.

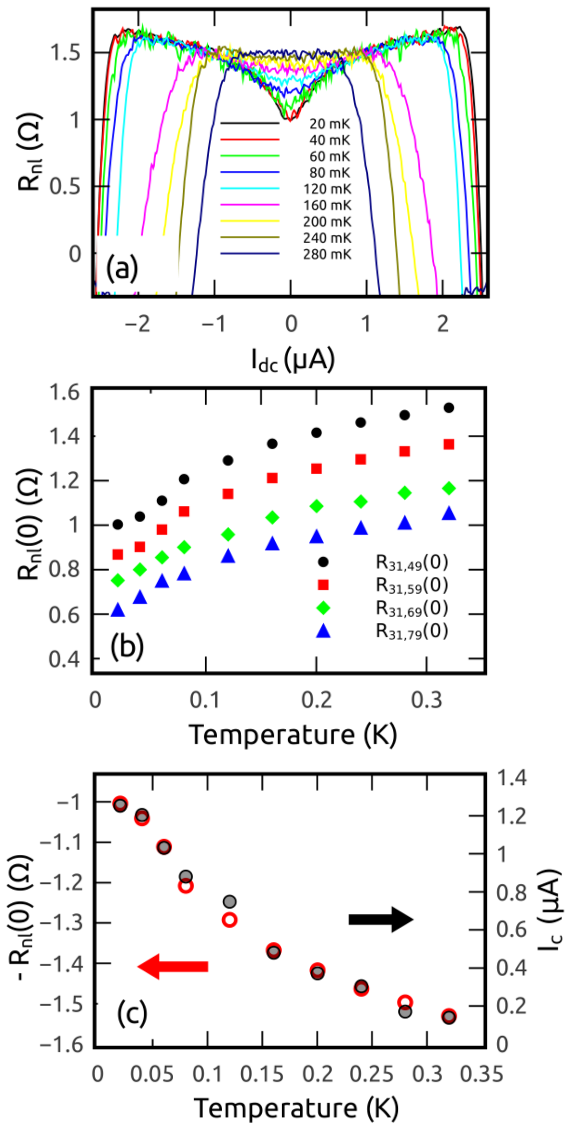

Figure 4.9. (a) Nonlocal differential resistance $R_{31,49}$ as a function of dc bias current $I_{\rm dc}$ at various temperatures. (b) Temperature dependence of zero bias nonlocal differential resistance $R_{\rm nl}(0)$ for four nonlocal resistance configurations $R_{31,49}$, $R_{31,59}$, $R_{31,69}$ and $R_{31,79}$. (c) Temperature dependence of $-R_{\rm nl}(0)$ for the configuration $R_{31,49}$ and temperature dependence of the local critical current I_c.

Qualitative differences in zero bias resistance and finite bias resistance including the peak resistance can be observed in the temperature dependence as well. Figure 4.9(a) shows the nonlocal differential resistance as a function of $I_{\rm dc}$ at various temperatures ranging from 20 mK up to 280 mK. While the traces for different temperatures match at a finite dc bias above $I_{\rm dc} \sim 1\ \mu$A except the increase of the critical current with the decrease of temperature, there is a clear distinction in the traces at small bias $I_{\rm dc}$ with a further development of the dip with decreasing temperature. The temperature dependence of the zero bias resistance extracted from the traces in (a) is shown in (b). Therefore, the zero-bias dip exhibits qualitative differences in the decay length and the temperature dependence from the finite bias resistances. A clue to the origin of the zero-bias dip can be seen in the comparison of the temperature dependence of the depth of the zero-bias dip and the local critical current I_c along the proximity-coupled normal metal, as shown in (c).

With a proper scaling factor along the y-axis, the depth of the zero-bias dip characterized by $-R_{\rm nl}(0)$ shows a good agreement in the temperature dependence with the critical current I_c, which suggests that the development of the zero-bias dip at low temperatures may be related to the pair correlations in the proximity-coupled normal metal.

In order to further elucidate our understanding of the origin of the zero-bias dip, let us discuss the results for the numerical calculations. Initially, we used a package of codes written by P. Virtanen based on the quasiclassical theory, available online at `http://ltl.tkk.fi/~theory/usadel1/`. The schematic diagram for the sample used in the calculation is shown in Figure 4.10 (a). As explained in Chapter 2, the nonlocal resistance was calculated as follows: For each value of a voltage V applied on N1, current along each path of the sample is calculated with two independent parameters, the phase difference $\Delta\phi$ between two superconducting reservoirs and the response voltage $V_{\rm nl}$ on N2. $\Delta\phi$ and $V_{\rm nl}$ are adjusted

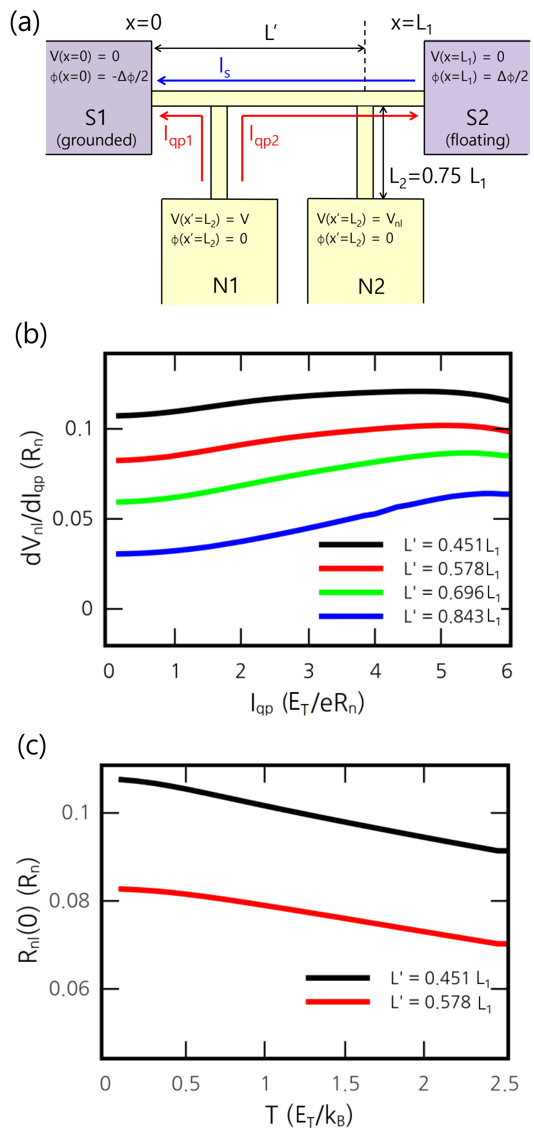

Figure 4.10. (a) Schematic diagram of the geometry considered in the calculation. L' is the distance between the superconducting reservoir S1 and the normal metal lead used to probe the nonlocal voltage V_{nl}. (b) Results of the nonlocal resistances as a function of injected current $I_{\mathrm{qp}} = I_{\mathrm{qp1}} + I_{\mathrm{qp2}}$. The distance L' is 0.451 L_1, 0.578 L_1, 0.696 L_1 and 0.843 L_1, where L_1 is the length of the proximity-coupled normal metal between S1 and S2. The position of N1 is fixed at 0.196 L_1 from S1. (c) Calculated zero bias resistance $R_{\mathrm{nl}}(0)$ as a function of temperature.

iteratively until the currents going into N2 and S2 become zero simultaneously. After obtaining the nonlocal voltage V_{nl} and the injected quasiparticle current $I_{\text{qp}} = I_{\text{qp1}} + I_{\text{qp2}}$ for various values of the applied voltage V, the nonlocal differential resistance can be calculated by taking $R_{\text{nl}} = dV_{\text{nl}}/dI_{\text{qp}}$. Figure 4.10 (b) shows the result of the nonlocal resistance as a function of I_{qp} at various values of the distance $L' = 0.451\ L_1$, $0.578\ L_1$, $0.696\ L_1$ and $0.843\ L_1$, where L_1 is the length of the proximity-coupled normal metal between S1 and S2. The position of N1 is fixed at $0.196\ L_1$ from S1 to match the geometry of the sample measured in the experiment. It is observed that the central dip at zero bias is absent and the nonlocal resistance only gradually increases due to the development of the phase difference $\Delta\phi$ between two superconductors arising from the increase of I_{qp}. In addition, the temperature dependence of the zero-bias nonlocal resistance $R_{\text{nl}}(0)$ shown in Figure 4.10 (c) exhibits an increase as the temperature is lowered in the range of temperature up to 2.5 E_T corresponding to $T \sim 300$ mK for the sample with the Thouless energy $E_T = 11.7\ \mu$eV shown in Figure 4.4, which is the reentrance effect explained earlier. Therefore, the results of these numerical calculations for the nonlocal differential resistance are inconsistent with the observed experimental dependence on both bias and temperature.

For further investigation of the numerical calculation, we started using the codes initially written by Prof. V. Chandrasekhar in IDL (Interactive Data Language) to produce the results presented in Ref. [**19**] and translated by the author to Python to obtain all the numerical results except the ones shown Figure 4.10. In addition, we employed a local configuration to calculate the resistance of the normal metal wire between N1 and N2 including the resistance of the proximity-coupled normal metal between S1 and S2. This was done by setting voltages $V/2$ and $-V/2$ on N1 and N2, respectively, as shown in Figure 2.14 for the following reasons: i) Knowing that a part of the injected quasiparticle current flows to the floating superconducting reservoir if the two superconducting reservoirs are Josephson-coupled in the nonlocal measurement configuration in the experiment, the resulting nonlocal differential resistance is essentially a fraction of the resistance of a part of the proximity-coupled normal metal that can be calculated in the local configuration as well. The central dip at zero bias associated with the decrease of the resistance at lower temperatures has been experimentally observed [**44**] with a sample in a similar geometry in a local configuration. ii) It is much more time-efficient to perform numerical calculations in local configurations than nonlocal configurations where two independent parameters $\Delta\phi$ and V_{nl} should be optimized simultaneously by multiple iterations of the code to satisfy the boundary conditions, which sometimes fails to converge.

Figure 2.18(a) shows the temperature dependence of the calculated resistance in the configuration explained above which exhibits a clear distinction from the experimental results shown in Figure 4.9(b). Again, the reentrance effect is observed, which is consistent with the numerical results obtained for the nonlocal differential resistance shown in Figure 4.10. The competition between the leakage of pair correlations and the proximity-induced gap in the DOS of the proximity-coupled normal metal results in a minimum of the resistance at T_{min}, which turns out to be dependent on the distance L_2 from the normal reservoirs to the proximity-coupled normal metal. As we extended L_2 such that the dephasing effect from the normal reservoirs diminishes, T_{min} saturates at $\sim 2.9\ E_T$ where $E_T = \hbar D/L_1^2$ is the Thouless energy of the proximity-coupled normal metal between S1 and S2 with length L_1, as shown in Figure 2.18. With the Thouless energy $E_T = 11.7\ \mu$eV of the sample, the minimum of the resistance is expected to appear at $T \sim 340$ mK, a much higher temperature than the base temperature of 20 mK reached in the experiment.

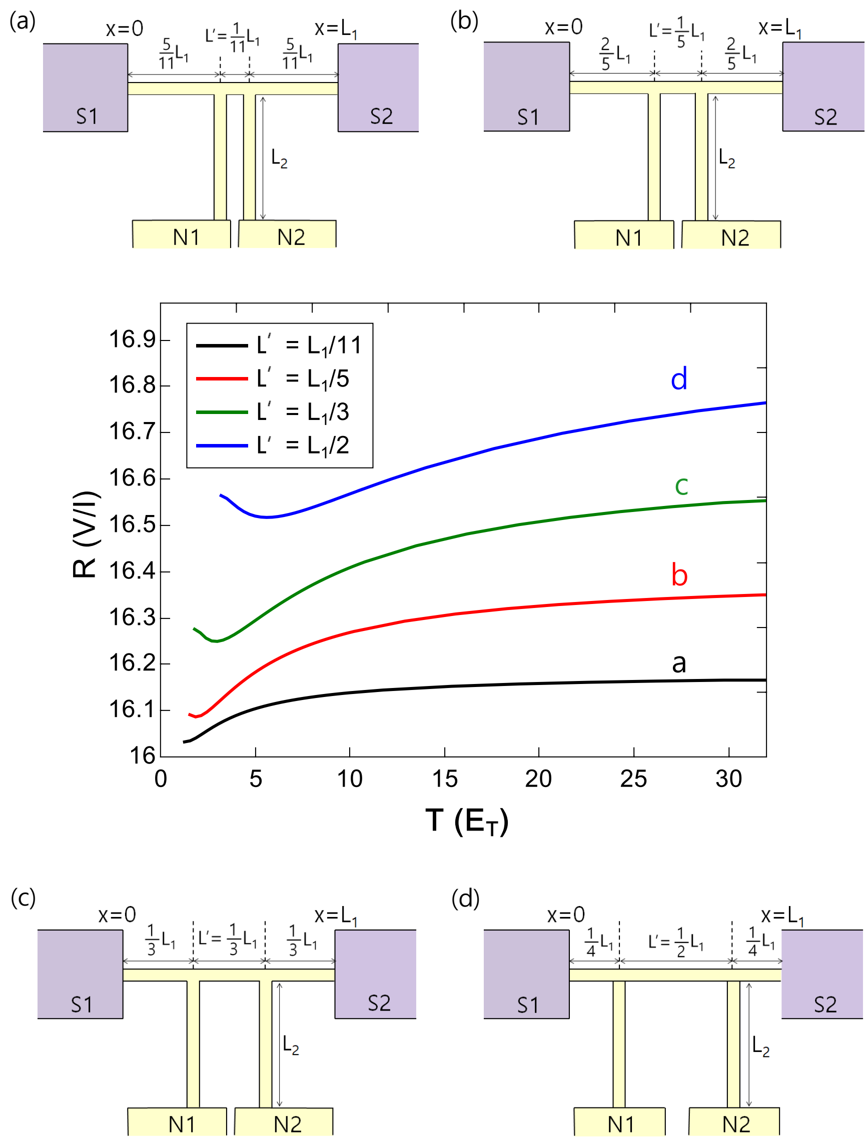

Figure 4.11. Resistance through normal metal wire between N1 and N2 as a function of temperature where the section of the proximity-coupled normal metal between two normal metal wire L' is varied as (a) $L' = L_1/11$, (b) $L' = L_1/5$, (c) $L' = L_1/3$, and (d) $L' = L_1/2$. The temperature is scaled with respect to the Thouless energy E_T of the proximity-coupled normal metal wire between S1 and S2 whose length is L_1. For the calculation of the resistance voltage +V/2 and -V/2 are applied to N1 and N2, respectively.

There are important factors that need to be considered to account for the discrepancy between the experimental results and the numerical calculations: First, the interfaces between the normal metal and the superconductor are assumed to be perfect in the numerical calculation whereas they are not in the sample used in the experiment. According to Ref. [**19**], the reduction of the NS interface transparency leads to the shift-down of T_{min} at which the minimum in resistance occurs in addition to a smaller decrease in the resistance due to the reduced leakage of pair correlations from the superconductor into the normal metal. Second, it should be noted that the geometry used in the numerical calculation employs a proximity-coupled normal metal wire embedded between two superconducting reservoirs in which the boundary condition for a bulk superconductor is applied. In the experiment, however, both ends of the proximity-coupled normal metal wire are connected to superconducting "wires", which extend over a few microns until they reach superconducting pads with larger dimensions that can be considered as reservoirs. In order to modulate the effective length between the proximity-coupled normal metal and the superconducting reservoirs, we repeated the calculation by varying the length L' of the section between two nodes where the normal wires coming from normal reservoirs meet the proximity-coupled normal metal as $L' = \frac{L_1}{11}, \frac{L_1}{5}, \frac{L_1}{3}$ and $\frac{L_1}{2}$ while maintaining the total length L_1 of the proximity-coupled normal metal, as shown in Figure 4.11. Shortening the length L' leads to the increase of the distance from the superconducting reservoir to the part of the proximity-coupled normal metal included in section to be calculated. The resulting traces exhibit the shift-down of T_{min} to lower temperatures as L' decreases. The origin of the shift of T_{min} can be found from the modification of the DOS in the proximity-coupled normal metal. Figure 4.12 shows the normalized DOS calculated at the center of the proximity-coupled normal metal for the same values of L' as in Figure 4.11. It should be noted that the T_{min} is determined by the broadness of the trace of the normalized DOS. As the distance from the superconductor is increased the broadness of the normalized DOS is narrowed and T_{min} is lowered.

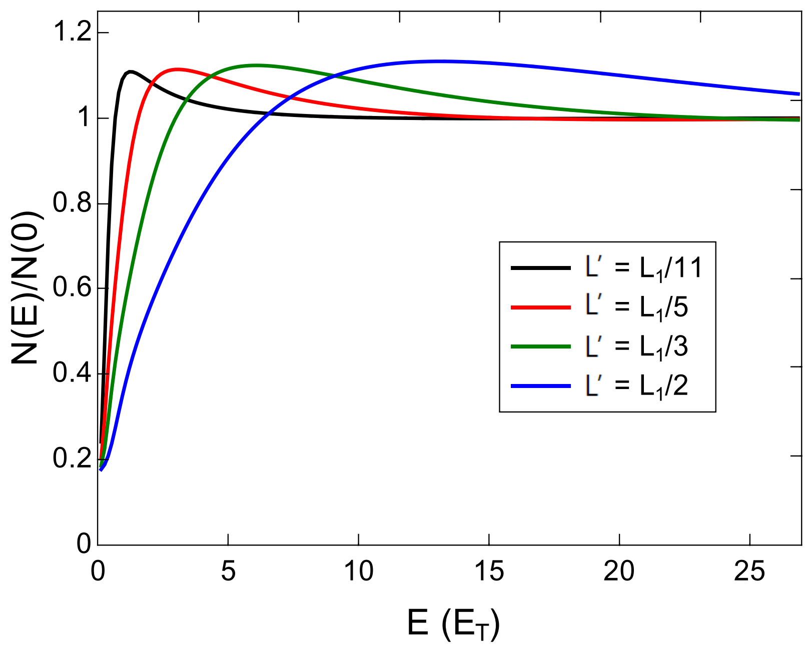

Figure 4.12. Normalized DOS $N(E)/N(0)$ as a function of energy at the center of the proximity-couled normal metal for various length L' as shown in Figure 4.11.

To summarize, in this section I presented the results of the experiments that we performed to observe the nonlocal correlations in the proximity-coupled normal metal. The nonlocal differential resistance exhibited overall bias dependence analogous to the results obtained from NSN samples, except a peculiar dip observed within a small range of bias current near zero. Our analysis suggests that the nonlocal differential resistance in the configurations employed in the measurements inevitably includes a partial resistance of the proximity-coupled normal metal due to the separation of the injected quasiparticle current mediated by the Josephson coupling between two superconductors. However, the origin of the detailed dependence on the bias current and the temperature which gives rise to the zero-bias dip could not be understood by this simple scenario. In addition, while the numerical calculations based on the quasiclassical theory predicted that the resistance of the proximity-coupled normal metal should exhibit the reentrance behavior with the minimum appearing at T_{min} within the range of temperature accessible in the experiment, only the decrease of the resistance has been observed in the experiment. Further quantitative analysis leads us to conjecture that the T_{min} may have been shifted down to much lower temperatures due to i) non-ideal interface quality and ii) reduced proximity-effect as the effective distance between the superconducting reservoir and the proximity-coupled normal metal is extended, which may need to be confirmed by further experimental attempts.

4.2. Loop geometry

In order to examine the phase coherence of the processes which give rise to the observed results discussed in the previous section, we fabricated a sample forming a loop structure, as shown in Figure 4.13 (a). Two SNS junctions, denoted as the upper and lower junction in this section, are placed in parallel and share the superconducting wire on each side. Such a hybrid device consisting of a normal metal and a superconductor is known as a SQUID in which the phase of the superconductor can be modulated by applying an external magnetic field through the loop.

Figure 4.13 (b) presents the local differential resistance $R_{15,96}$ as a function of dc bias current I_{dc} at various temperatures. A finite amount of supercurrent flows across the SNS junction including the loop as we increase the dc current until the amplitude of the current reaches the critical current of the junction, which is $I_c \sim 3.8$ μA at the lowest temperature $T = 30$ mK. For this sample, the length of the normal metal is $L = 550$ nm and the diffusion coefficient of Au is $D = 170$ cm^2/s, which results in the Thouless energy $E_T = 37$ μeV.

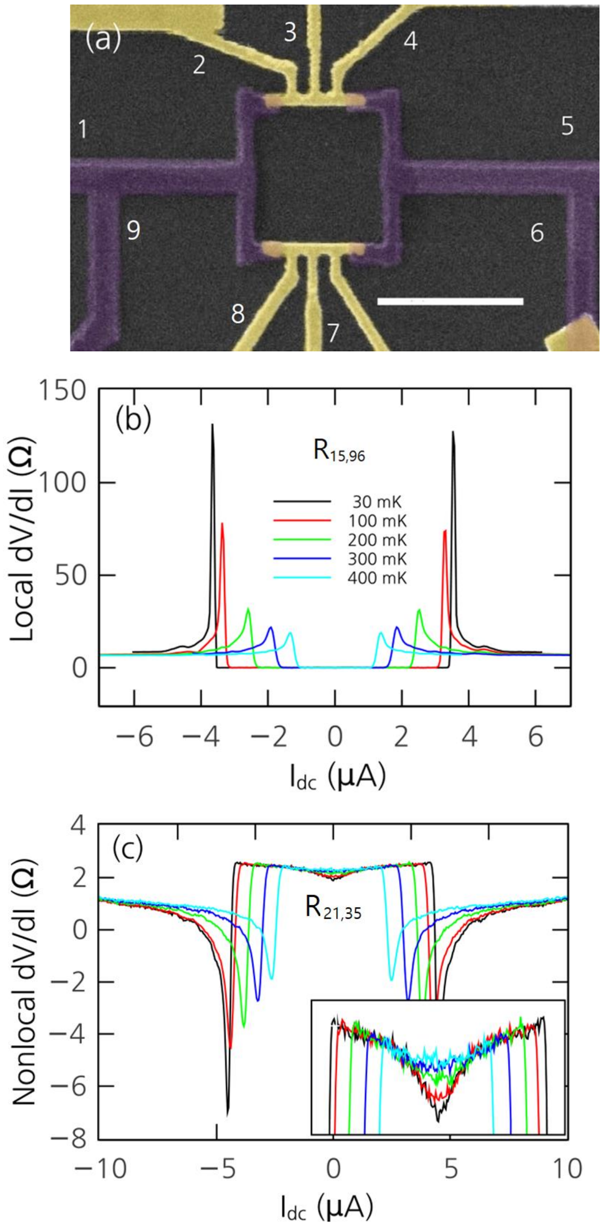

Figure 4.13. (a)False color scanning electron microscope (SEM) image of the sample consisting of Au (yellow) and Al (purple). The size bar is 1 μm. (b) The local differential resistance $R_{15,96}$ and (c) the nonlocal differential resistance $R_{21,35}$ as a function of dc bias current $I_{\rm dc}$ at various temperatures. Inset of (c): The same plot zoomed-in near zero bias.

With the normal resistance $R_N = 6.6\ \Omega$, $I_{c0}eR_N/E_T$ is 0.62 which is much smaller than the value expected for the long SNS junction limit ($E_T \ll \Delta$) [**42**]. As discussed in the previous section, it is attributed to the normal metal wires attached to the proximity-coupled normal metal between two superconductors.

Figure 4.13 (c) shows the nonlocal differential resistance $R_{21,35}$ as a function of dc bias current $I_{\rm dc}$ at the same temperatures as in (b), which exhibits qualitatively the same dependence on $I_{\rm dc}$ as discussed earlier: i) The central dip appears at zero bias. ii) $\frac{dV}{dI}$ increases as a function of $I_{\rm dc}$, reaching a peak followed by a sharp negative resistance dip. iii) At various temperatures, the traces sit on top of one another in the range of a large $I_{\rm dc}$ except for the critical current being dependent on the temperature, whereas the zero bias resistance reveals a significant dependence on the temperature. These results confirm that the sample in a loop geometry behaves in qualitatively the same manner as the samples in a linear geometry in the absence of an external magnetic field.

A similar qualitative analysis can be made on the origin of the nonlocal differential resistance based on the separation of injected quasiparticle current. However, the model becomes slightly more complicated due to the complexity of the geometry of the sample as well as the existence of the screening current which arises in response to an applied magnetic field. To be more specific, Figure 4.14 schematically depicts the currents in a loop sample. In the measurement configuration for the nonlocal differential resistance on the upper normal metal wire of the SNS junction, a quasiparticle current $I_{\rm qp}$ is injected from N1 to S1 through the node "A" while measuring the voltage between N2 and S2. Due to the Josephson coupling between the two superconductors S1 and S2, $I_{\rm qp}$ is separated into $I_{\rm qp1}$ and $I_{\rm qp2}$ satisfying $I_{\rm qp} = I_{\rm qp1} + I_{\rm qp2}$. Unlike the linear sample considered before, however, although S2 is again electrically floating, the total current flowing through the node "B" into S2 is not required

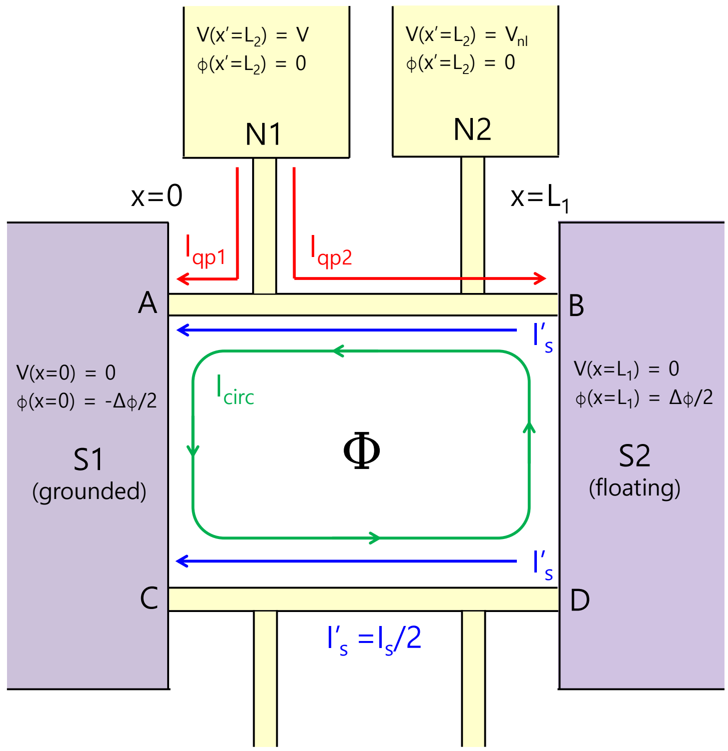

Figure 4.14. Current separation model in a loop sample. A screening current I_{circ} circulating around the loop arises due to an external magnetic flux Φ. The measurement configuration is for the nonlocal differential resistance to observe the nonlocal correlations in the proximity-coupled normal metal between the nodes "A" and "B".

to be zero. This is due to the existence of the other SNS junction where a finite amount of supercurrent can flow through the node "D" from S2 to S1. In the absence of an external magnetic flux, $\Phi = 0$, if the upper and lower junctions are assumed to be identical, the same amount of supercurrent $I_s' = I_s/2$ flows through the upper and lower normal metal wire. Here, I_s is the total supercurrent flowing from S2 to S1 by generating a phase difference $\Delta\phi$ between them as a response to the separation of the quasiparticle current I_{qp}. In the presence of a small external magnetic flux, $\Phi \neq 0$, a screening current I_{circ} begins to circulate through the loop as shown in Figure 4.14. Therefore, the total supercurrents in the upper normal metal wire and the lower normal metal wire are $I'_s + I_{\rm circ}$ and $I'_s - I_{\rm circ}$, respectively. It should be noted that the gradient of the phase ϕ in the superconducting reservoirs is considered to be negligible even in the presence of the screening current $I_{\rm circ}$, assuming that the critical current of the superconducting reservoir itself I_c^{Al} is much larger than $I_{\rm circ}$. The separation of injected quasiparticle current continues until the total supercurrent through either upper or lower normal metal wire reaches the critical current of its respective junction. The relation between the fraction of the injected quasiparticle current $I_{\rm qp2}$ flowing into S2 and the resulting supercurrent can be found by requiring the total current injected from N1, $I_{\rm qp1} + I_{\rm qp2}$, to be equal to the total current drained into S1 through the nodes "A" and "C", $I_{\rm qp1} + 2I'_s = I_{\rm qp1} + I_s$, which results in $I_{\rm qp2} = I_s$. This condition is equivalent to the one obtained by requiring the total current into S2 through the nodes "B" and "D" to be zero.

As the external flux is increased, the amplitude of the circulating screening current $I_{\rm circ}$ is increased until the flux reaches $\Phi_0/2$, half of the magnetic flux quantum $\Phi_0 = h/2e$. When the flux exceeds the half a flux quantum, the system energetically prefers encompassing one flux quantum by switching the direction of the screening current. The amplitude of the screening current now is decreased as the external field is increased and becomes zero when the flux is exactly Φ_0. Then the screening current again reverses direction as the external field is further increased. Therefore, the direction of the screening current periodically changes at every multiple of the half a flux quantum, $\Phi = \frac{n\Phi_0}{2}$ $(n = 0, \pm1, \pm2, \cdots)$. Such a periodic modulation of the screening current by an external magnetic flux can be observed in the measurement of the local differential resistance $R_{28,37}$ where the current is sent from one of the normal metal leads connected to the upper normal metal wire and drained through one of the normal metal leads connected to the lower normal metal wire. These data are shown in Figure 4.15. Since the area of the loop is $A_{loop} \sim 1.04\ \mu\text{m}^2$ for the current sample, the external magnetic field corresponding to the flux quantum is $B = \Phi_0/A_{loop} \sim 1.97$ mT.

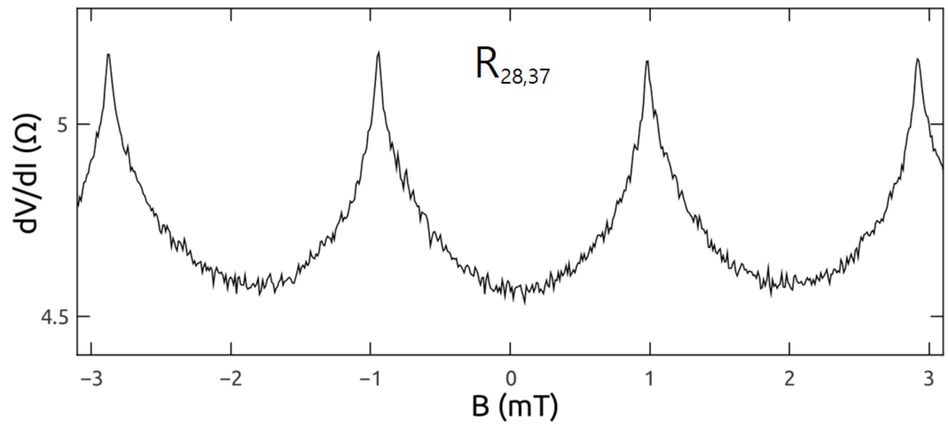

Figure 4.15. The local differential resistance $R_{28,37}$ as a function of the external magnetic field B.

Before turning back to the configuration for the nonlocal differential resistance, let us discuss the critical current I_c^{SNS} across the SNS junction including the loop in the presence of an external magnetic flux Φ. This critical current is the maximum amplitude of the supercurrent that arises in response to the injection of quasiparticle current in nonlocal configurations. In order to do that, one needs to adopt the gauge-invariant phase difference following the discussion found in Ref. [**73**], which is defined as

$$\gamma = \Delta\phi - \frac{2\pi}{\Phi_0}\int \mathbf{A}\cdot d\mathbf{s} \tag{4.1}$$

where $\Delta\phi$ is the intrinsic phase difference and $\mathbf{A}$ is the vector potential of the magnetic field $\mathbf{B} = \nabla \times \mathbf{A}$ which is integrated along $d\mathbf{s}$. Therefore, the gauge-invariant phase differences along the upper and the lower normal metal wires are given by $\gamma_{\mathrm{AB}} = \phi_{\mathrm{AB}} - \frac{2\pi}{\Phi_0}\int_{\mathrm{A}}^{\mathrm{B}} \mathbf{A}\cdot d\mathbf{s}$, $\gamma_{\mathrm{BD}} = \frac{2\pi}{\Phi_0}\int_{\mathrm{B}}^{\mathrm{D}} \mathbf{A}\cdot d\mathbf{s}$, $\gamma_{\mathrm{DC}} = \phi_{\mathrm{DC}} - \frac{2\pi}{\Phi_0}\int_{\mathrm{D}}^{\mathrm{C}} \mathbf{A}\cdot d\mathbf{s}$, and $\gamma_{\mathrm{CA}} = \frac{2\pi}{\Phi_0}\int_{\mathrm{C}}^{\mathrm{A}} \mathbf{A}\cdot d\mathbf{s}$. With $\phi_{\mathrm{AB}} = -\phi_{\mathrm{DC}}$, we obtain $\oint \nabla\gamma\cdot d\mathbf{s} = \gamma_{\mathrm{AB}}+\gamma_{\mathrm{BD}}+\gamma_{\mathrm{DC}}+\gamma_{\mathrm{CA}} = \frac{2\pi}{\Phi_0}\oint \mathbf{A}\cdot d\mathbf{s} = \frac{2\pi\Phi}{\Phi_0}$. It should be noted that there is a finite change in the gauge-invariant phase difference along the superconductors due to the external magnetic field. Since the supercurrent across the SNS junction including the loop is the sum of the supercurrents along the upper and lower junctions, the flux dependence of the critical current I_c^{SNS} of the SNS junction including the loop can be found by numerically solving $I_c^{SNS}(\Phi) = \max|I_s(\gamma_{\mathrm{AB}}) + I_s(\gamma_{\mathrm{CD}})|$. For the simplest case of the critical currents along both upper and lower junctions being identical to I_{c0}, the critical current of the SNS junction is reduced to $I_c^{SNS}(\Phi) = 2I_{c0}\left|\cos\left(\pi\frac{\Phi}{\Phi_0}\right)\right|$, which becomes zero when Φ corresponds to odd multiples of the half flux quantum.

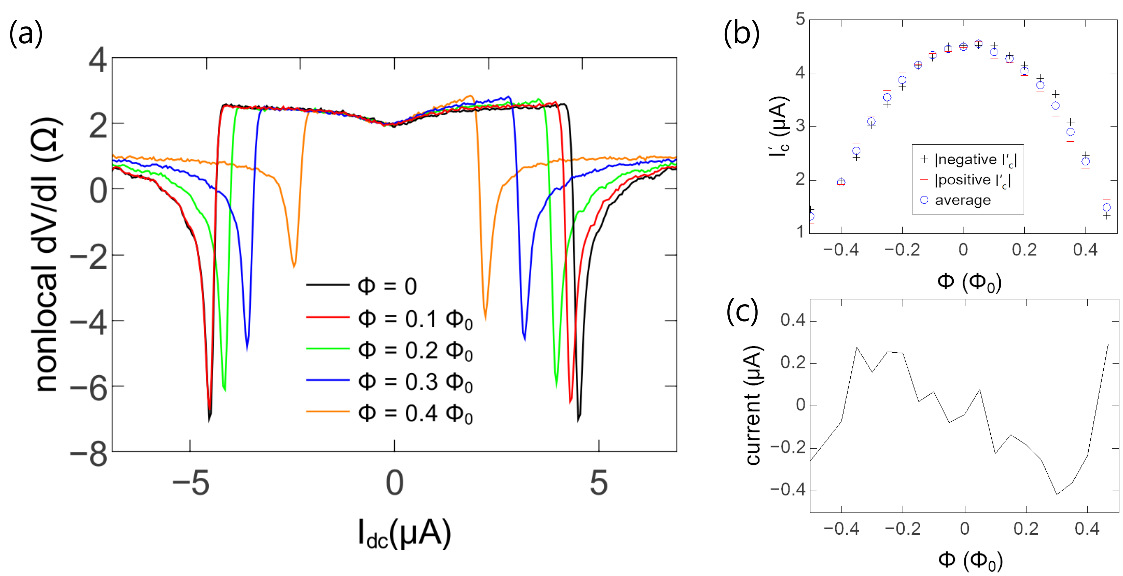

Figure 4.16. (a) The nonlocal differential resistance $R_{21,35}$ as a function of I_{dc} at various external magnetic fluxes Φ measured at 30 mK. (b) Nonlocal critical current I_c' as a function of external flux. (black: magnitude of positive I_c', red: magnitude of negative I_c', blue: average of magnitudes of positive and negative I_c'. (c) Difference of magnitudes of positive and negative I_c'.

Figure 4.16 (a) shows the nonlocal differential resistance $R_{21,35}$ as a function of I_{dc} at various external magnetic fluxes Φ. It can be observed that an asymmetry is introduced in the differential resistance at finite biases and the size of dips as an external magnetic flux is applied, which becomes more prominent as the amplitude of the flux increases. It should also noted that the nonlocal critical current I_c' where a negative resistance dip appears is highly dependent on the external field. Figure 4.16 (b) presents the magnitude of the positive and negative nonlocal critical currents. While the average of the two shows the trace expected for the critical current $I_c^{SNS}(\Phi)$ across the SNS junction, there is a small difference between the magnitude of the positive and negative nonlocal critical current which is attributed to the screening current I_{circ}, as shown in (c).

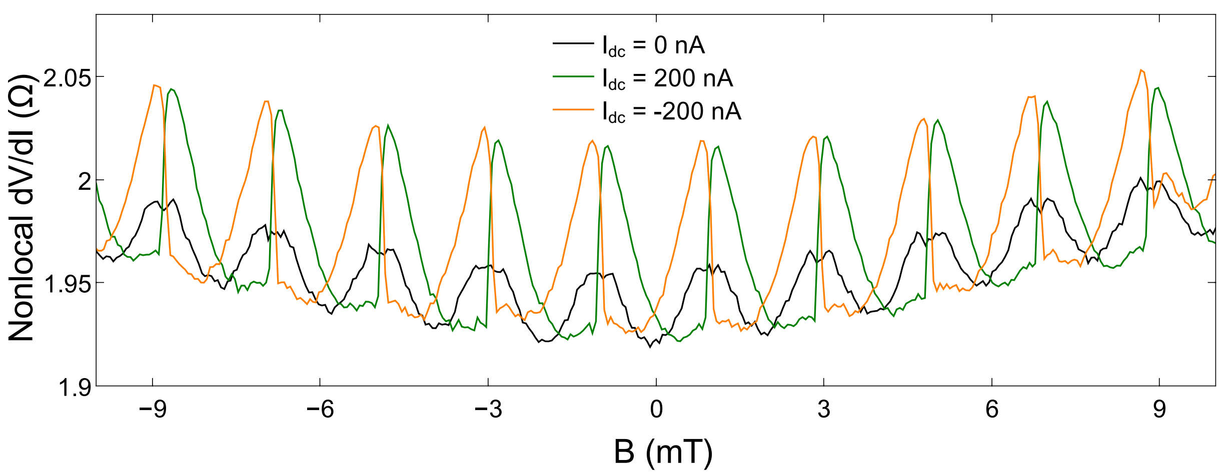

Figure 4.17. The nonlocal differential resistance $R_{21,35}$ as a function of external magnetic field, with different amplitudes (black: 0 nA, green: 200 nA, and orange: -200 nA) of dc current added.

The asymmetry of the nonlocal differential resistance in the bias dependence can be further examined by continuously sweeping the magnetic field with a finite amount of dc current I_{dc} added. Figure 4.17 presents three traces of nonlocal differential resistance $R_{21,35}$ as a function of external magnetic field, with different amplitudes of added I_{dc}. The black trace was obtained with no added dc current. Overall, the nonlocal differential resistance is periodically modulated by the field, which suggests that the leakage of pair correlations from both superconductors due to the proximity effect contributes to the zero-bias dip in the nonlocal differential resistance where the phase difference between them is adjusted by the external field. A gradual increase of the resistance at a finite external field can be explained as the result of the generated phase difference between the two superconductors by the field which would give rise to a destructive interference, leading to the suppression of the proximity effect. In addition, while the overall periodic dependence is due to the periodic switching of the direction of screening current I_{circ} as explained before, a series of small dips which appear as the external flux reaches $\Phi = (n + \frac{1}{2})\Phi_0$ $(n = 0, \pm 1, \pm 2, \cdots)$ is associated with the diminishing of the critical current $I_c^{SNS}(\Phi)$ of the SNS junction at odd multiples of half a flux quantum. It should be noted that such a series of dips is absent in the measurement configuration shown in Figure 4.15. This is due to the fact that the relevant critical current that may play a role in that configuration is the critical current I_c^{Al} of the superconducting wires connecting upper and lower normal metals, not the critical current of the SNS junction including the loop I_c^{SNS}, with a much larger magnitude than I_c^{SNS}, i.e., $I_c^{Al} \gg I_c^{SNS}$ that does not vanish at odd multiples of magnetic flux quantum.

On the other hand, with a finite amount of I_{dc} added in the measurement configuration, the field dependence of the same differential resistance is drastically modified. A finite I_{dc} added in the nonlocal configuration gives rise to a finite supercurrent I_s which leads to a finite phase difference $\Delta\phi_0$ between the two superconductors. As shown in the schematic diagram presented in Figure 4.14, the generated phased difference $\Delta\phi_0$ gives rise to a supercurrent either in a parallel or antiparallel direction to the screening current arising as a response to the external flux, which leads to an effective shift of the trace in the field dependence. Therefore, adding $I_{\mathrm{dc}} = 200$ nA and -200 nA result in two traces antisymmetric with each other due to the opposite sign of ϕ_0 depending on the direction of the added dc current.

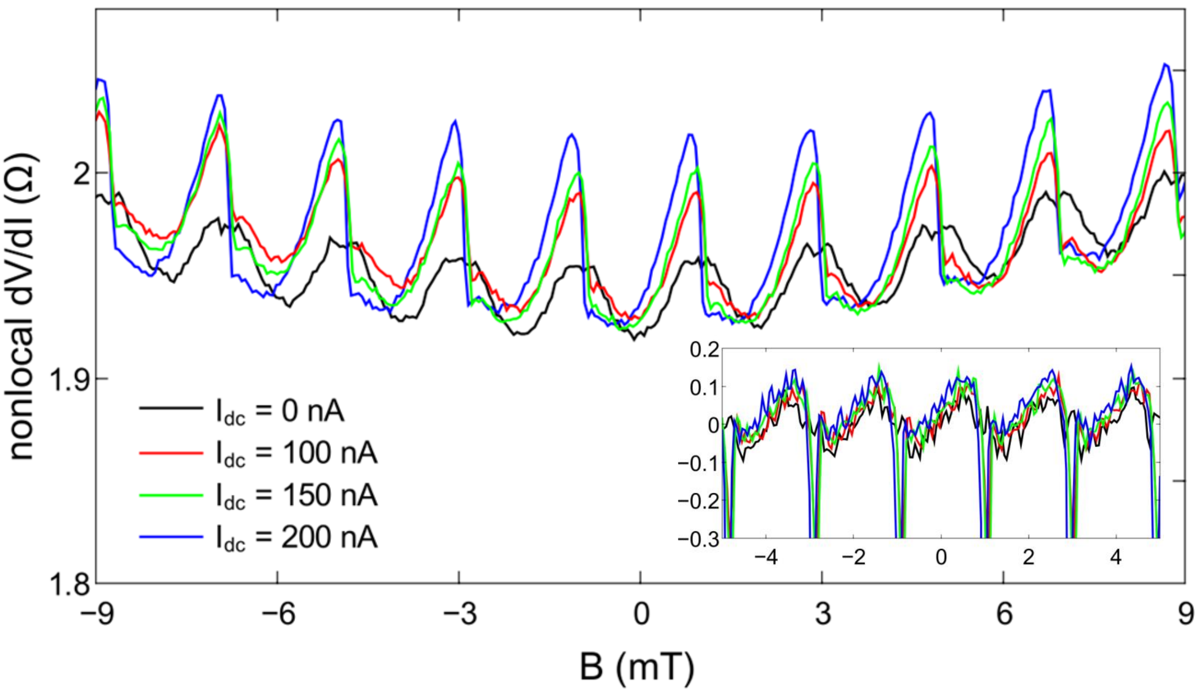

Figure 4.18. The nonlocal differential resistance $R_{21,35}$ as a function of external magnetic field, with different amplitudes (black: 0 nA, red: 100 nA, green: 150 nA, and blue: 200 nA) of dc current added. Inset: Derivative of the traces with respect to magnetic field.

Figure 4.18 shows the results with various amplitudes of I_{dc} added along the same direction. It can be observed that as the amplitude of I_{dc} increases the nonlocal differential resistance increases at zero field and the shift of the trace becomes more significant, which is due to the increase of the generated phase difference $\Delta\phi_0$ in accordance with the increase of the amplitude of I_{dc}. This leads to a more pronounced asymmetry with a larger magnitude of the oscillation of the resistance. It can be inferred that it is due to the shift of the traces by I_{dc}, which results in the recovering of the part of oscillation that was buried near $\Phi = (n + \frac{1}{2})\Phi_0$ $(n = 0, \pm 1, \pm 2, \cdots)$ due to the diminishing of the critical current I_c^{SNS} of the SNS junction including the loop. In order to confirm this conjecture, we compare the local differential resistance $R_{28,37}$ and the nonlocal differential resistance $R_{21,35}$ in Figure

4.19. With a proper scaling factor applied to the trace of the local differential resistance, the traces of $R_{28,37}$ and $R_{21,35}$ as a function of the external magnetic field are aligned with each other except a small range of the field near odd multiples of the half flux quantum as shown in (a). This suggests that the origin of the oscillation of resistance is the same for the local and nonlocal configuration of the measurement. For the traces with increased amplitude of $I_{\rm dc}$ shown in (b)-(d), the traces of $R_{28,37}$ and $R_{21,35}$ can be aligned with each other as well. For doing this, a finite shift B_0 in the field B_0 = -0.22, -0.31, and -0.46 mT should be applied for $I_{\rm dc}$ = 100, 150, and 200 nA, respectively. Knowing that $B \sim 1.97$ mT corresponds to $\Delta\phi = \pi$, this can be interpreted as finite phase differences $\Delta\phi_0/\pi$ = 0.11, 0.16, and 0.23 established by the injection of respective $I_{\rm dc}$. It should be noted that while the traces are shifted the abrupt change due to the switching of the screening current $I_{\rm circ}$ always occurs at odd multiples of the half flux quantum regardless of the amplitude of $I_{\rm dc}$, which can be seen in the inset of Figure 4.18.

We also measured $R_{21,35}$ as a function of an external magnetic field at various temperatures. Figure 4.20 presents the results at T = 30, 100, 200, 300, and 400 mK with added dc current (a) $I_{\rm dc}$ = 0 and (b) $I_{\rm dc}$ = 500 nA. The traces indicate that the as the temperature is lowered, the magnitude of oscillations in the field dependence as well as the reduction of the nonlocal differential resistance at zero field are increased by enhanced leakage of pair correlations from the superconductors. Again, the drastic difference caused by the addition of $I_{\rm dc}$ is due to the shift of the traces by the finite phase difference $\Delta\phi_0$ between the two superconductors, which is generated by the counter-flowing supercurrent arising in response to the injected quasiparticle current.

So far, we discussed the experimental results obtained from samples in SQUID structure. Qualitatively, the nonlocal differential resistance exhibited consistent results with the

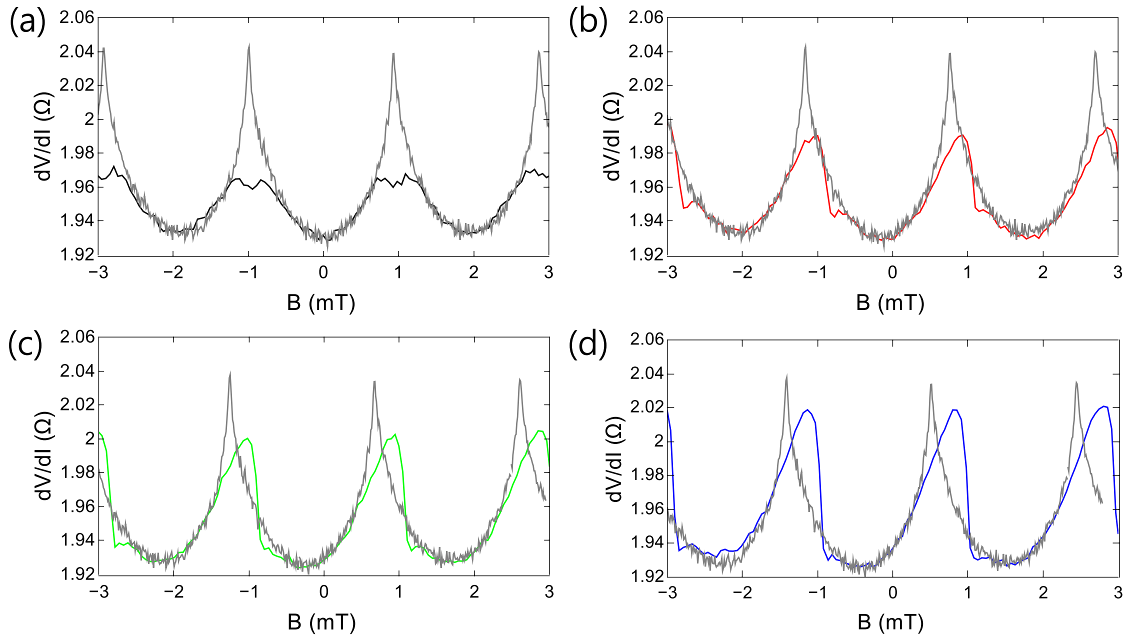

Figure 4.19. Comparison of traces of the local differential resistance $R_{28,37}$ and the nonlocal differential resistance $R_{21,35}$ as a function an external magnetic field. With a proper scaling factor applied to the trace of the local differential resistance, two traces can be aligned to each other with a finite shift B_0 in the field $B_0 = 0$, -0.22, -0.31, and -0.46 mT for $I_{\mathrm{dc}} =$ (a) 0, (b) 100, (c) 150, and (d) 200 nA, respectively.

samples with linear structure including a peculiar dip near zero bias in the dc bias current dependence. As the phase difference between the two superconductors is modulated by an external magnetic field, the zero-bias dip exhibited a periodic oscillation. This supports that the central dip is associated with the leakage of pair correlations from both superconductors connected to the proximity-coupled normal metal in a coherent manner, hence it is reduced as external parameters as temperature or magnetic field that destroy the coherence of the process are applied. In addition, the dependence on the external magnetic field turned out to be significantly affected by both the direction and the amplitude of the injected dc current I_{dc}. Therefore, the experimental results suggest that in order to understand the underlying

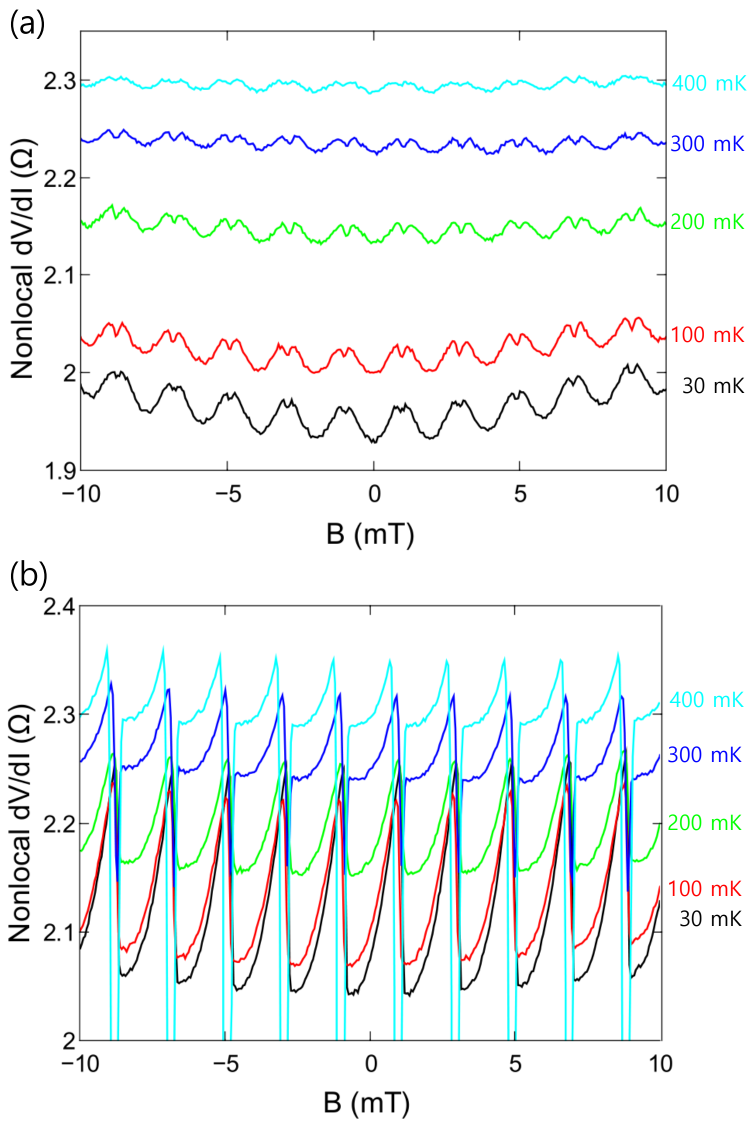

Figure 4.20. The nonlocal differential resistance $R_{21,35}$ as a function of an external magnetic field at various temperatures, with (a) $I_{\mathrm{dc}} = 0$ and (b) $I_{\mathrm{dc}} = 500$ nA.

physics that determines the nonlocal differential resistance, the interplay between the quasiparticle current and the supercurrent including the screening current through the SQUID should be properly taken into account.

CHAPTER 5

Experimental results: Spin-polarized transport through double ferromagnet/superconductor junction

Recently, several experiments [**55, 58, 59**] investigating spin transport in a superconductor have been performed in the presence of large Zeeman splitting. The key in those experiments is the creation of spin imbalance in a superconductor due to the generation of a difference in the density of states (DOS) for spin up and spin down quasiparticles by applying a magnetic field to the superconductor. Before introducting these experiments, it should be emphasized that the experimental regime realized there is different from that of our theoretical work presented in Chapter 2 where the nonlocal resistance arises due to the subgap transport, not due to the quasiparticles with energies above the gap. In this chapter, I will first explain the spin transport mediated by the spin-polarized quasiparticles observed in Refs. [**55, 58, 59**], followed by an analysis of our experimental results in similar structures, which reveals an interesting feature in a low bias current regime in addition to the results reported in the references.

5.1. Spin imbalance

Hübler *et al.* [**55**] reported long-range spin-polarized transport in a mesoscopic superconductor observed in the sample shown in Figure 5.1. Ferromagnet (F: Fe) leads form tunnel contacts (I) with the superconductor (S: Al), leading to a FISIF structure, which makes it possible to focus on the transport of quasiparticles with energies above the gap of the superconductor. In the experiment, as an injection voltage $V_{\rm inj}$ is applied, the nonlocal differential conductance is measured by probing the nonlocal current $I_{\rm det}$ with leads spatially separated from the leads used for the injection.

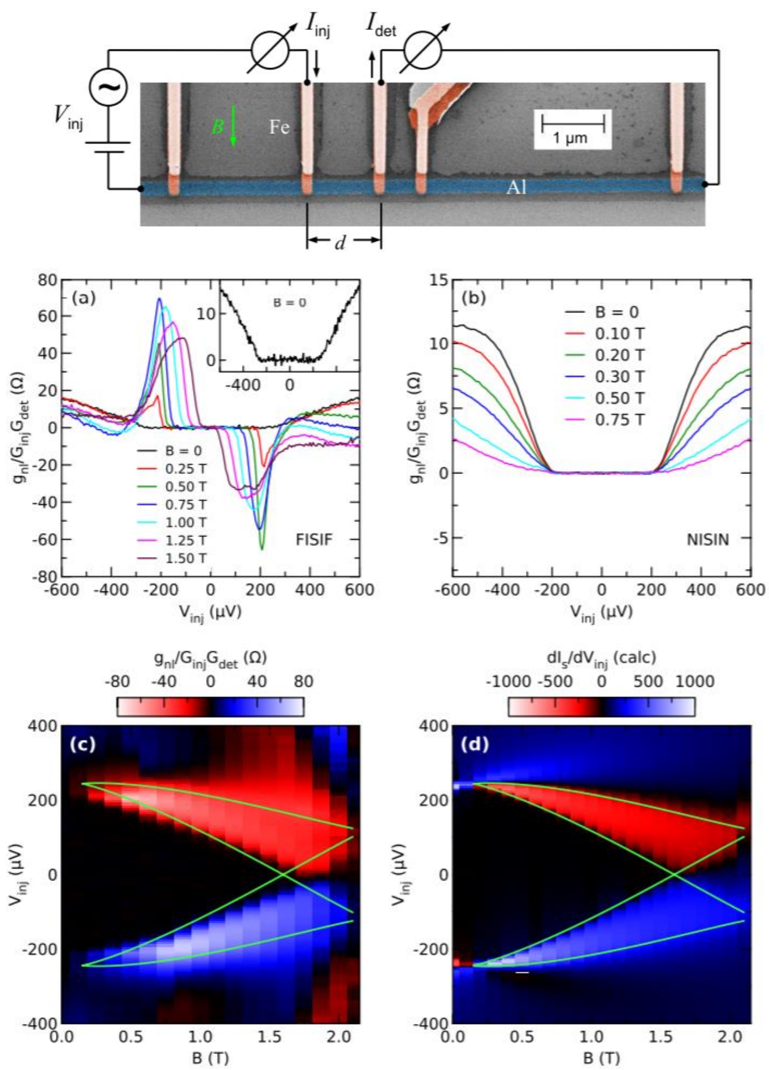

Figure 5.1. Normalized nonlocal differential conductance $g_{\rm nl}/G_{\rm inj}G_{\rm det}$ as a function of injector voltage $V_{\rm inj}$ for different applied magnetic fields B for (a) FISIF sample and (b) NISIN sample. (c) The data from panel (a) plotted on a color scale. (d) The calculated differential spin current. Figure is taken from Ref. [**55**].

Figure 5.1 (a) and (b) exhibit the main results of the experiment. In the FISIF sample, a distinct antisymmetric dependence of nonlocal differential conductance on the injection voltage V_{inj}, in addition to a symmetric background, is observed in the presence of a finite magnetic field. It should be noted that there is a gap near zero bias which occurs due to the suppression of the conductance through the tunnel contact and the size of the gap is reduced as the amplitude of the magnetic field increases. On the contrary, when the ferromagnet leads are replaced by normal metal (Cu) leads, the antisymmetric dependence disappears, only leaving the symmetric background. Hübler *et al.* attributed the antisymmetric dependence of the differential conductance to the transport of spin imbalance carried by spin-polarized quasiparticles which was only detected in FISIF sample. They explained the antisymmetric feature by noting that the amount of spin imbalance should be independent of the polarity of the injection voltage. On the other hand, they attributed the symmetric background to charge imbalance that was commonly detected in both FISIF (Figure 5.1 (a)) and NISIN (Figure 5.1 (b)) samples. They further investigated the bias dependence of the nonlocal differential conductance in NISIF and FISIN samples [**58**] and demonstrated that in order to observe the antisymmetric feature, the ferromagnet lead is required only for the detection part. These experimental results confirm that the spin imbalance is mainly generated due to the Zeeman splitting of the density of states for up and down spin quasiparticles in the superconductor, not due to the spin-polarized injection from the ferromagnet lead. They also investigated the dependence of the transport of spin imbalance on the distance between the injector and detector. The results revealed that the antisymmetric dependence persisted up to the distances of several μm, which exceeds other length scales such as the coherence length and the normal state spin-diffusion length. They argued that such a long relaxation length may be associated with the recombination length of the quasiparticles rather than a spin-diffusion length.

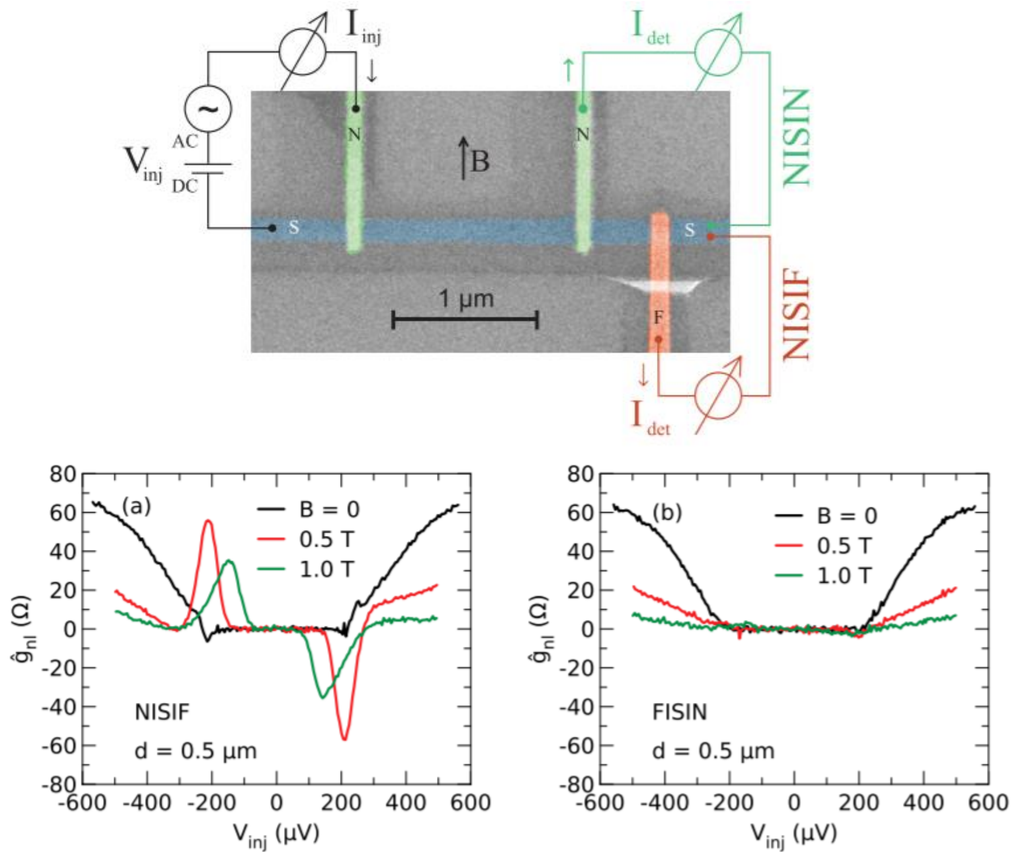

Figure 5.2. (a) Normalized nonlocal differential conductance $\hat{g}_{\rm nl}$ with N as injector and F as detector (NISIF) for several magnetic fields. (b) $\hat{g}_{\rm nl}$ for the same contacts and magnetic fields, but with F as injector and N as detector (FISIN). Figure is adopted from Ref. [**58**].

A similar experiment has been performed in another group and reported by Quay *et al.* [**59**] who measured a mesoscopic sample shown in Figure 5.3, where two ferromagnet (Co/Pd) leads form tunnel contacts with a superconductor (Al). They measured the nonlocal differential resistance instead of conductance by injecting a bias current and probing the nonlocal voltage with respect to the superconductor. The result is similar to what was

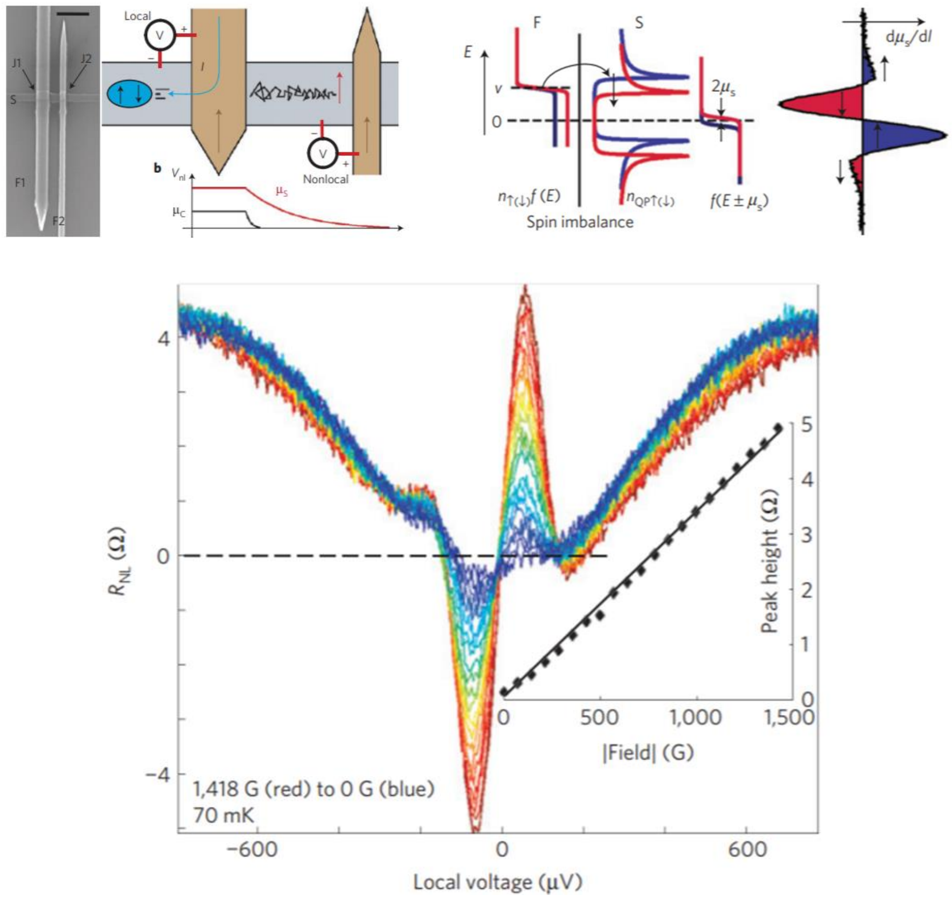

Figure 5.3. Top left: Scanning electron microscope (SEM) image of the sample and the measurement scheme. Inset: Schematic diagram for spatial dependence of charge potential μ_C and spin potential μ_S. Top right: A schematic representation of the theoretical model showing densities of states and distribution functions in F1 and S, and expected dependence of spin imbalance on the bias voltage. Bottom: Nonlocal differential resistance as a function of local voltage at different magnetic fields from -1418G (red) to 0G (blue). Inset : Peak height as a function of magnetic field. Figure is taken from Ref. [**59**].

observed in the work of Hübler: With a finite magnetic field applied, antisymmetric differential resistance on the bias voltage is observed in addition to a symmetric background. The magnitude of the antisymmetric feature is proportional to the amplitude of the applied magnetic field within a certain range. They further investigated the dependence of the nonlocal differential resistance on the relative magnetization configuration of two ferromagnet leads. Figure 5.4 (a) shows the results for two different configurations, parallel and antiparallel, from which the spin imbalance (antisymmetric) and charge imbalance (symmetric) components are extracted.

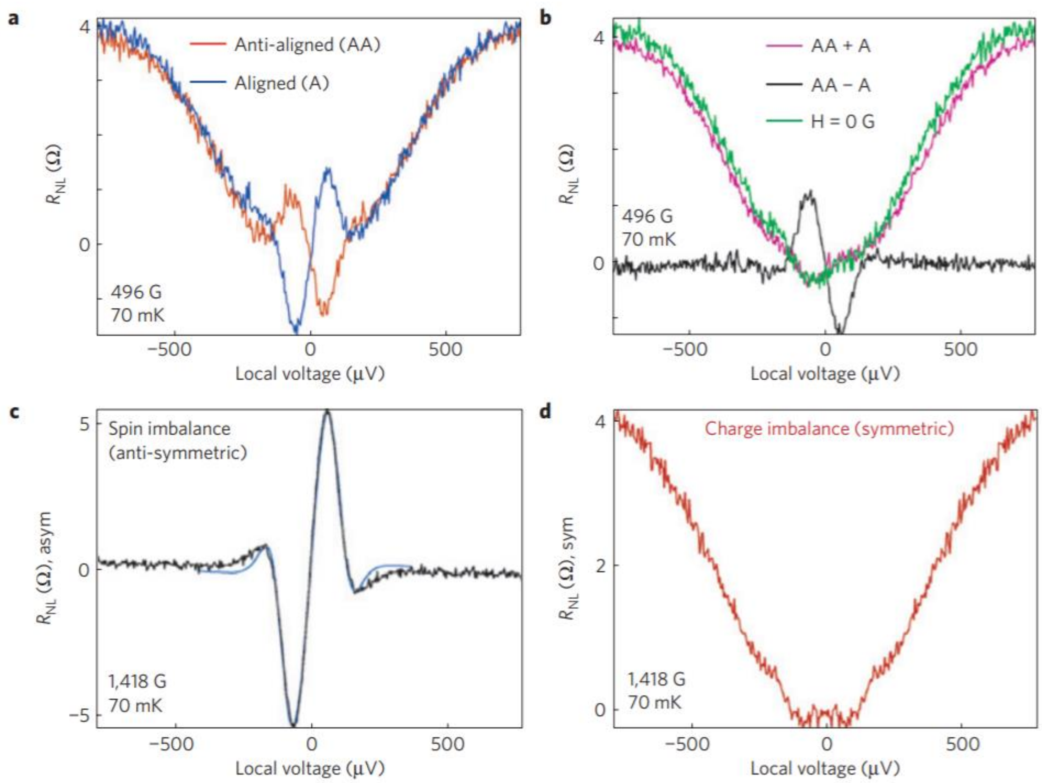

Figure 5.4. (a) Nonlocal differential resistance as a function of local voltage at 496 G with the detector electrode aligned (blue line) then anti-aligned (red line) with the injector electrode and the magnetic field. The spin imbalance signal changes sign while the charge imbalance signal remains the same. (b) The sum and difference between the two traces divided by two. Note that the sum trace is almost identical to a trace taken at zero applied field. (c) The antisymmetric and (d) symmetric part of the trace (a). Figure is taken from Ref. [**59**].

Despite some quantitative differences in the results, overall, the results from both research groups support the conclusion that spin imbalance can be generated in a superconductor by the Zeeman splitting in the density of states of up and down spin quasiparticles due to applied magnetic field. Such a spin imbalance can transport over distance of several μm in the superconductor and is detected by a ferromagnet lead spatially separated from the injector.

5.2. Transport through double FS junctions

While a tunnel barrier between a ferromagnet and a superconductor was realized in the references introduced in the previous section in order to suppress the subgap transport, we intended to form a transparent interface between them. For that reason, I used the shadow mask two-angle deposition technique, explained earlier in Chapter 3, to deposit 30 nm of Ni at 40 degrees followed by 80 nm of Al at 90 degrees without breaking the vacuum. The widths of two ferromagnets are designed to be different to achieve different respective coercive fields so that it is possible to realize parallel and antiparallel configurations of magnetization.

Before discussing the experimental results, let us take a look at the geometry of the sample. As shown in Figure 5.5 (a), two parallel ferromagnets (Ni: purple) aligned along the Y-axis form four interfaces with two parallel superconductors (Al: green) aligned along the X-axis. The reason why the sample involves two sets of ferromagnets and superconductors lies in the initial purpose of the experiment. As introduced earlier in this thesis, a proximity-coupled normal metal wire with length L between two superconductors is able to carry a finite supercurrent if the Thouless energy $E_T = \hbar D/L^2$ becomes lower than the thermal energy k_BT. This is translated into the length scale of $L_T = \sqrt{\hbar D/k_BT}$ which can be up to an order of a micron at low enough temperatures. However, this is not the case when the normal metal wire is replaced by a ferromagnet wire. Due to a large exchange field in the ferromagnet, up and down electrons forming a Cooper pair experience a splitting of the energy leading to a much shorter length scale on which the pair amplitude decays [**75**].

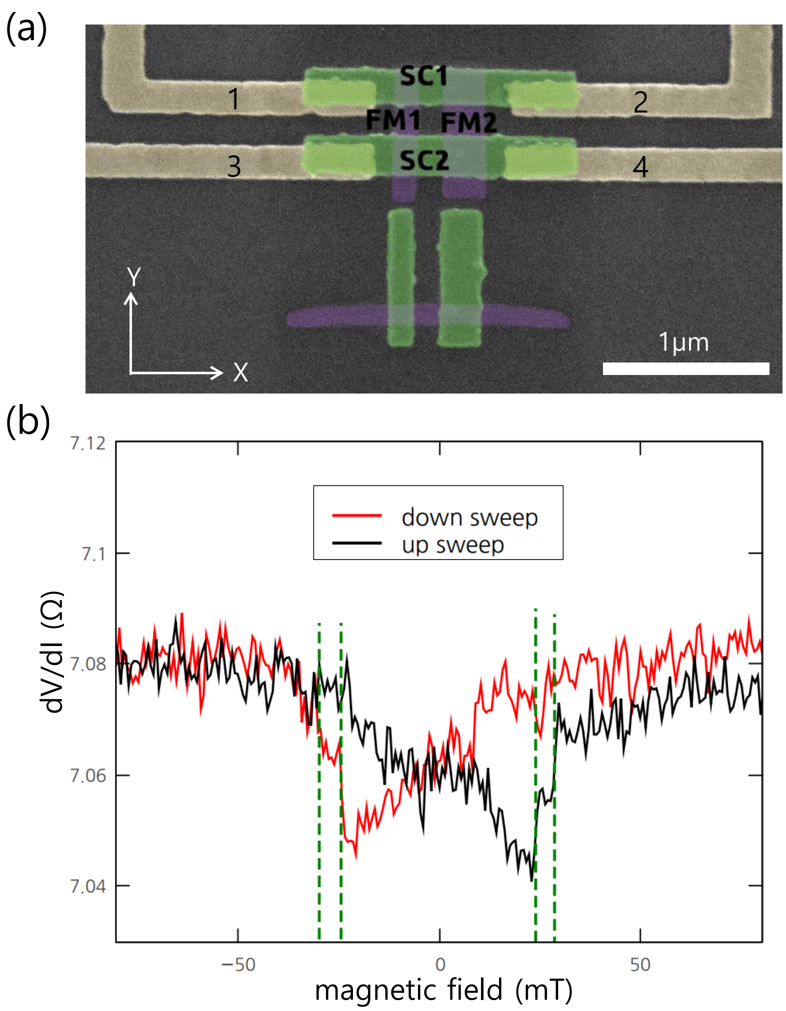

Figure 5.5. (a) False color scanning electron microscope (SEM) image of the "short" sample. The green wires are superconductors (Al), the purple wires are ferromagnets (Ni), and the yellow wires are normal metal (Au) leads. (b) Differential resistance $R_{13,24}$ of the sample as a function of applied magnetic field measured at 4.4 K. The measurement configuration if shown in the top figure. The result exhibits anisotropic magnetoresistance (AMR) with a double-step feature. Green dashed lines are added as a visual guide.

Experimental works [**76, 77**] realized by fabricating a SFS junction in a stack structure revealed a very short decay length of supercurrent, an order of a few nm, in addition to an oscillatory dependence of the critical current I_c on the thickness of ferromagnet, called π-*junction*. Such distinct differences observed in SFS junctions compared to SNS junctions lead us to a question: If such a short decay length is associated with the energy splitting between the electrons forming a Cooper pair, might it be reconciled if the electrons forming the pair are split before entering the ferromagnet that exerts a finite exchange field and combined later? In order to answer this question, I fabricated a sample in the geometry shown in Figure 5.5 where two ferromagnets separated by 150 nm form a parallel circuit of two SFS junctions (named as "short" sample), as well as another sample in the same geometry but with a much longer separation of 750 nm between two ferromagnets as a control sample ("long" sample).

First we measured anisotropic magnetoresistance (AMR) at 4.4 K to investigate the response of the ferromagnets upon the application of external magnetic field. As shown in Figure 5.5 (b), the differential resistance $R_{13,24}$ exhibits clear double-step features as a function of the applied magnetic field, which confirms that the respective coercive fields of two magnets are different. This shows that it is possible to realize parallel and antiparallel configurations of magnetization. However, due to the natural hysteresis of the ferromagnet, care should be taken to keep track of the field sweep history to determine the magnetization configuration properly. We then cooled the samples further down to 30 mK and measured the differential resistance of both "short" and "long" samples as a function of bias current in several different measurement configurations. However, no finite supercurrent was observed in any configuration in both samples. Nonetheless, some interesting features have been observed in the experiment, which I believe are worth mentioning in this section.

Among various measurement configurations possible in the sample, we will discuss the differential resistance $R_{34,12}$ of the "short" sample measured by sending a current along a superconductor SC2 from lead "3" to "4" and probing the voltage difference between lead "1" and "2" across the other superconductor SC1. One might expect to observe zero resistance

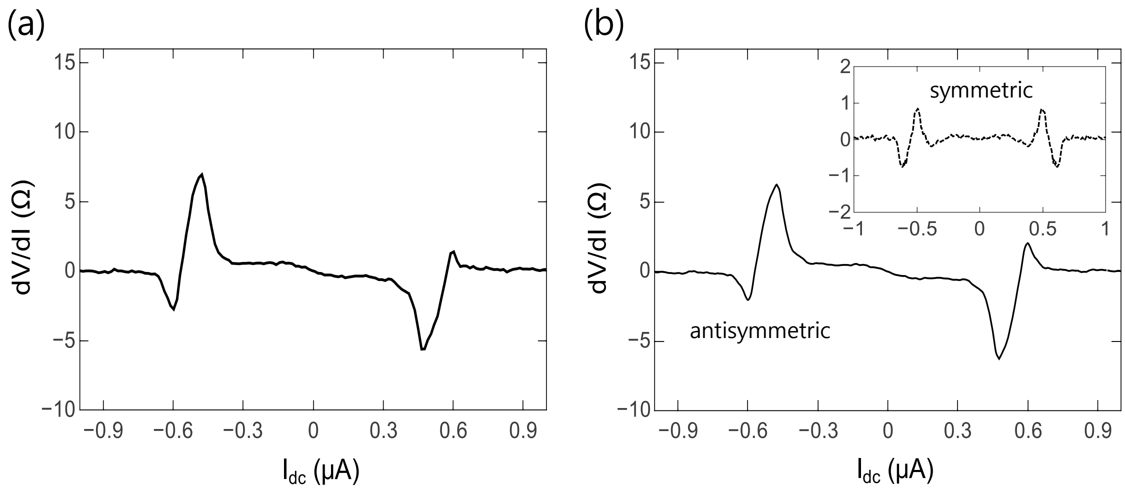

Figure 5.6. (a) Differential resistance $R_{34,12}$ of "short" sample as a function of bias current at zero field. The magnetization configuration of two ferromagnets are aligned along one direction denoted as $\uparrow\uparrow$. (b) Antisymmetric part (solid line in main figure) and symmetric (dashed line in inset) of the data shown in (a).

simply assuming that all the current flows through SC2. However, the experimental results show a significant bias dependence implying that there may be more complicated processes going on. For example, Figure 5.6 shows $R_{34,12}$ as a function of bias current at zero applied magnetic field. Before making measurements, the magnetic field was ramped up to 100 mT to align the magnetization of two ferromagnets in the same direction which we denote as $\uparrow\uparrow$. There are a few features worth describing: First of all, $R_{34,12}$ is highly antisymmetric in bias current I_{dc}, which can be confirmed by numerically extracting the antisymmetric and symmetric parts. As shown in (b), the antisymmetric part is almost an order of magnitude larger than the symmetric part. Second, there is a set of pronounced peaks and dips at $I_{\mathrm{dc}} \sim \pm 0.5\ \mu\mathrm{A}$ in both the antisymmetric and symmetric parts. Third, there is a clear bias dependence in a smaller range of the bias. Before moving on to the examination of the dependence of theses features on the external magnetic field, we first discuss the results of the measurements with different configurations of magnetization of two ferromagnets.

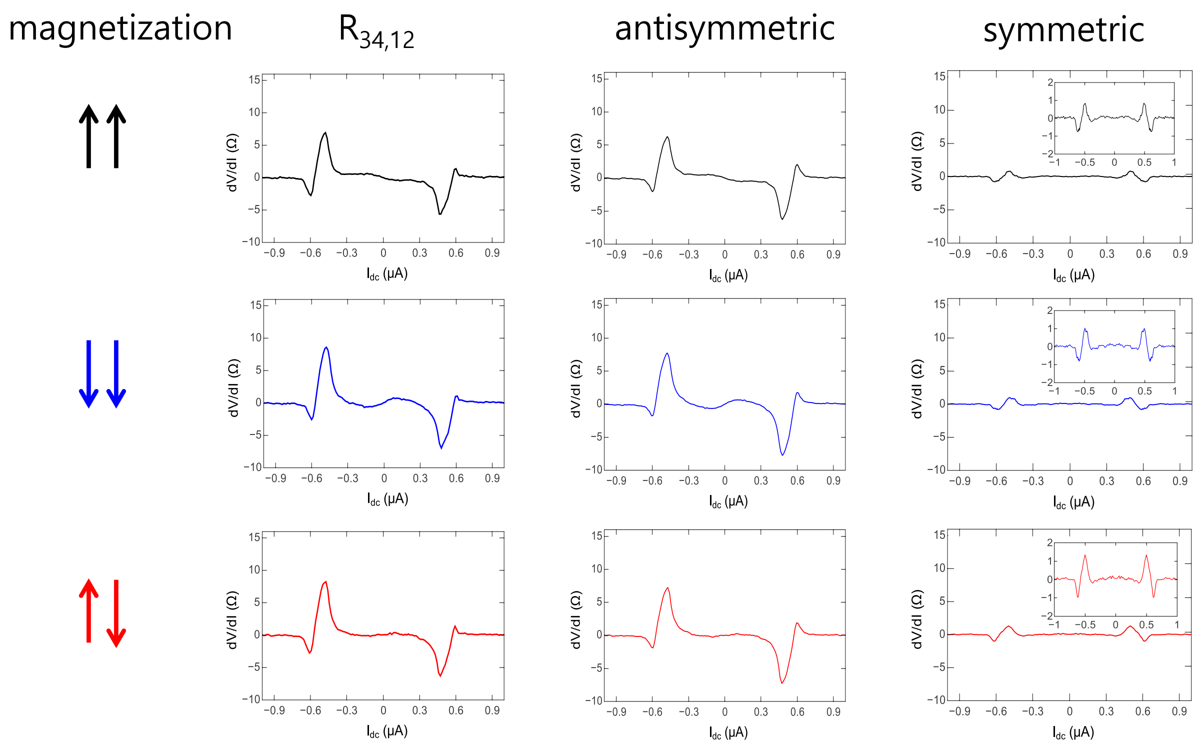

Figure 5.7. Differential resistance $R_{34,12}$ of the "short" sample as a function of bias current with three different configurations of magnetization, ↑↑ (black), ↑↓ (red), and ↓↓ (blue). The antisymmetric and symmetric parts are presented along with the raw data.

Figure 5.7 shows $R_{34,12}$ as a function of bias current with three different configurations of magnetization all at zero external magnetic field. The black trace is for the parallel configuration ↑↑ aligned by external magnetic field 100 mT, and the blue trace is for the parallel configuration ↓↓ aligned in the opposite direction by -100 mT. Finally, the red trace is for the antiparallel configuration ↑↓ which is achieved by ramping down the magnetic field from 100 mT to -27 mT where only the wider ferromagnet (FM2) changes the direction of the magnetization from ↑ to ↓. The trace for the other antiparallel configuration ↓↑ is omitted as it reveals the same dependence on the bias current as $\uparrow\downarrow$. From the data, it should be noted that not only the magnitude of the large peaks and dips at $I_{\rm dc} \sim \pm 0.5$ μA but also the feature in a smaller range of the bias are dependent on the configuration of magnetization. Moreover, the dependence on the configuration of magnetization is found only in antisymmetric parts, while no significant difference is observed in the traces of symmetric parts.

Figure 5.8 shows $R_{34,12}$ as a function of bias current at different values of the applied magnetic field where the configuration of magnetization of the two ferromagnets is specified for each value of the field. Again we extract the antisymmetric and symmetric parts, which exhibit distinctly different dependences upon the application of the magnetic field. The symmetric part maintains the shape of the trace except the positions of small peaks and dips move inward as the amplitude of the applied field increases. However, the antisymmetric parts exhibit rather complicated behavior: First, the set of large peak and dip appearing at $I_{\rm dc} \sim 0.5$ μA at zero field not only moves inward as the amplitude of the applied field increases but also clearly changes its magnitude. Second, another set of peak and dip in a smaller range of the bias is significantly dependent on the applied field as well and even changes the polarity of the peak and dip depending on the direction of the applied field.

In order to further investigate the field dependence of $R_{34,12}$ in the small bias current range, we measured the differential resistance at a finite bias $I_{\rm dc} = -0.15$ μA as a function of the applied field continuously swept between ± 90 mT, as shown in Figure 5.9. The value of bias $I_{\rm dc}$ is selected to measure the minimum value of the differential resistance in the small bias regime, which appears at $I_{\rm dc} \sim -0.15$ μA, nearly independently of the amplitude of applied field in the range of ± 30 mT. The blue solid line is the trace starting from -90 mT to saturate the magnetization of two ferromagnets into $\downarrow\downarrow$. As the field is swept from negative to positive direction, the differential resistance corresponding to the minimum in the small

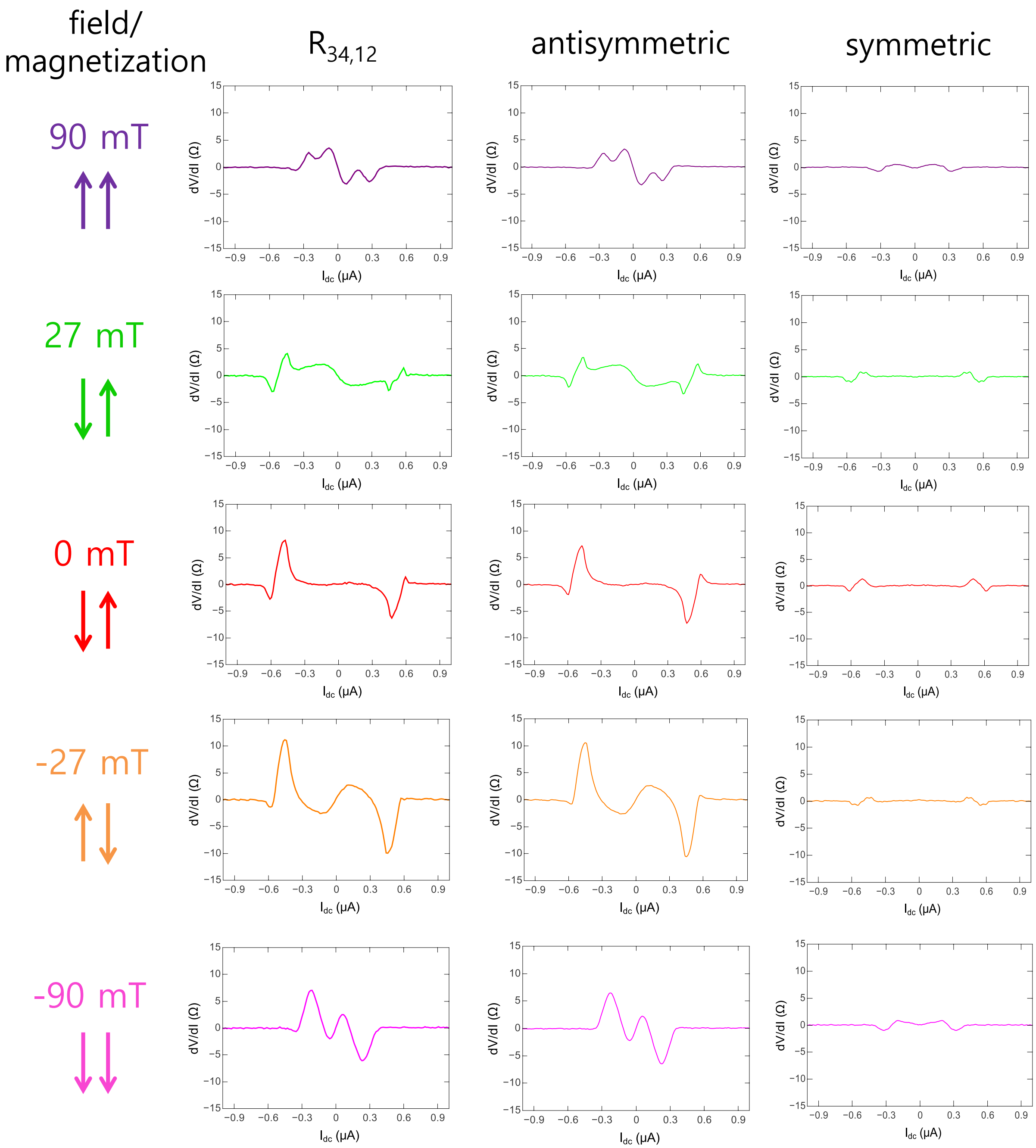

Figure 5.8. Differential resistance $R_{34,12}$ as a function of bias current at different values of the applied external magnetic field. The antisymmetric and symmetric are presented along with the raw data.

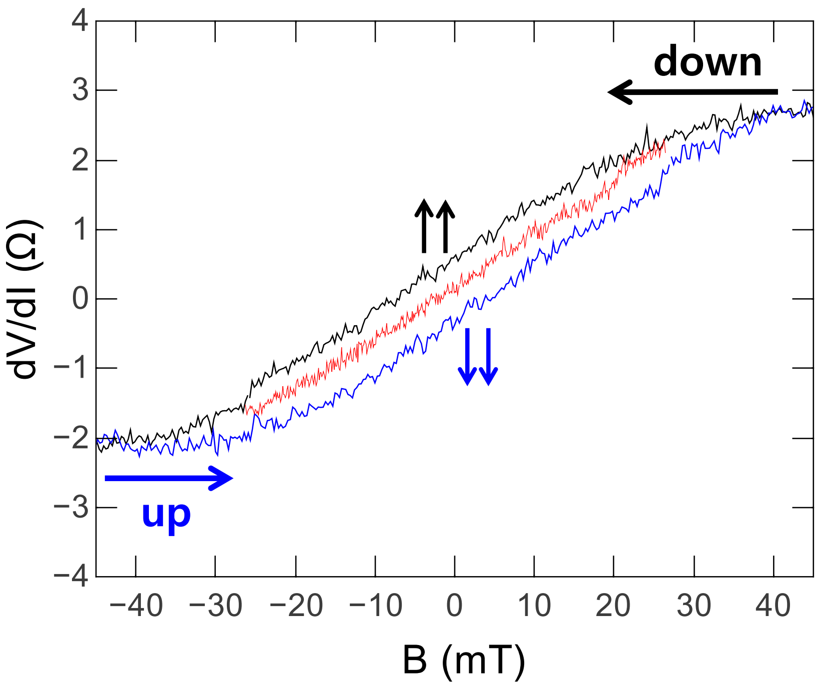

Figure 5.9. The differential resistance of "short" sample at $I_{dc} = -0.15\ \mu$A. Magnetic field is continuously swept from −90 mT to 90 mT (blue solid line), from 90 mT to −90 mT (black solid line), and from −27 mT to 27 mT (red solid line).

bias regime increases, almost proportionally to the amplitude of applied field. An abrupt increase at ∼27 mT should be noticed which occurs due to the change of the magnetization of the wider ferromagnet (FM2). Once the field reaches all the way to 90 mT, the magnetization of the two ferromangets is now aligned as ↑↑. The black solid line is the trace swept from 90 mT, which exhibits a clear distinction from the blue trace. Evidently, this is attributed to the different magnetization configurations, which is consistent with the results presented in Figure 5.7. For confirmation, another trace has been obtained by sweeping the field between ±27 mT to maintain the magnetization configuration as ↑↓, which falls in between the trace for ↓↓ and ↑↑ shown by the blue solid line. Therefore, the result shown in Figure

5.9 demonstrates that the feature in the small range of the bias is dependent both on the applied magnetic field and the configuration of magnetization of the ferromagnets.

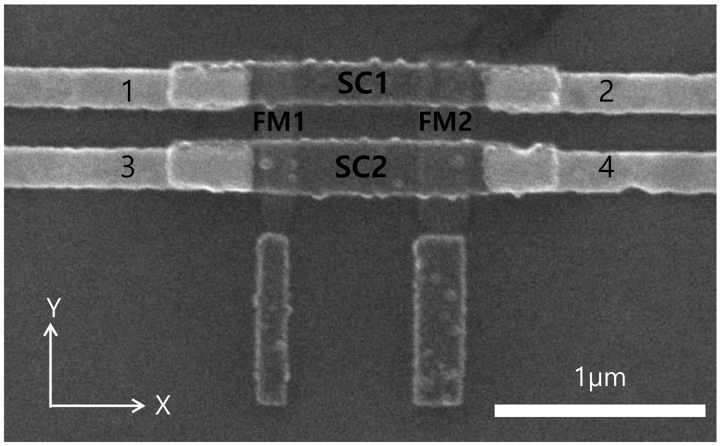

Figure 5.10. Scanning electron microscope (SEM) image of the "long" sample.

Now we move on to the result obtained from the "long" sample shown in Figure 5.10. Figure 5.11 shows the differential resistance $R_{34,12}$ of the "long" sample as a function of bias current at zero magnetic field with three different configurations of magnetization, $\uparrow\uparrow$, $\uparrow\downarrow$, and $\downarrow\downarrow$. Unlike that of the "short" sample, the differential resistance is highly symmetric in bias current $I_{\rm dc}$, which can be confirmed by the antisymmetric and symmetric parts shown separately. While a set of large peak and dip appears at $I_{\rm dc} \sim 1.6$ μA, another set of peak and dip in a smaller range of the bias is almost fully suppressed. In addition, there is no clear distinction between the traces for three different configurations of magnetization, in contrast to the case of the "short" sample.

Figure 5.12 presents $R_{34,12}$ as a function of bias current at different values of the applied magnetic field. Similar to the results obtained from the "short" sample, a set of large peak and dip change the positions and the magnitudes as a response to the application of the magnetic field. In addition, a set of peak and dip develops in a smaller range of the bias

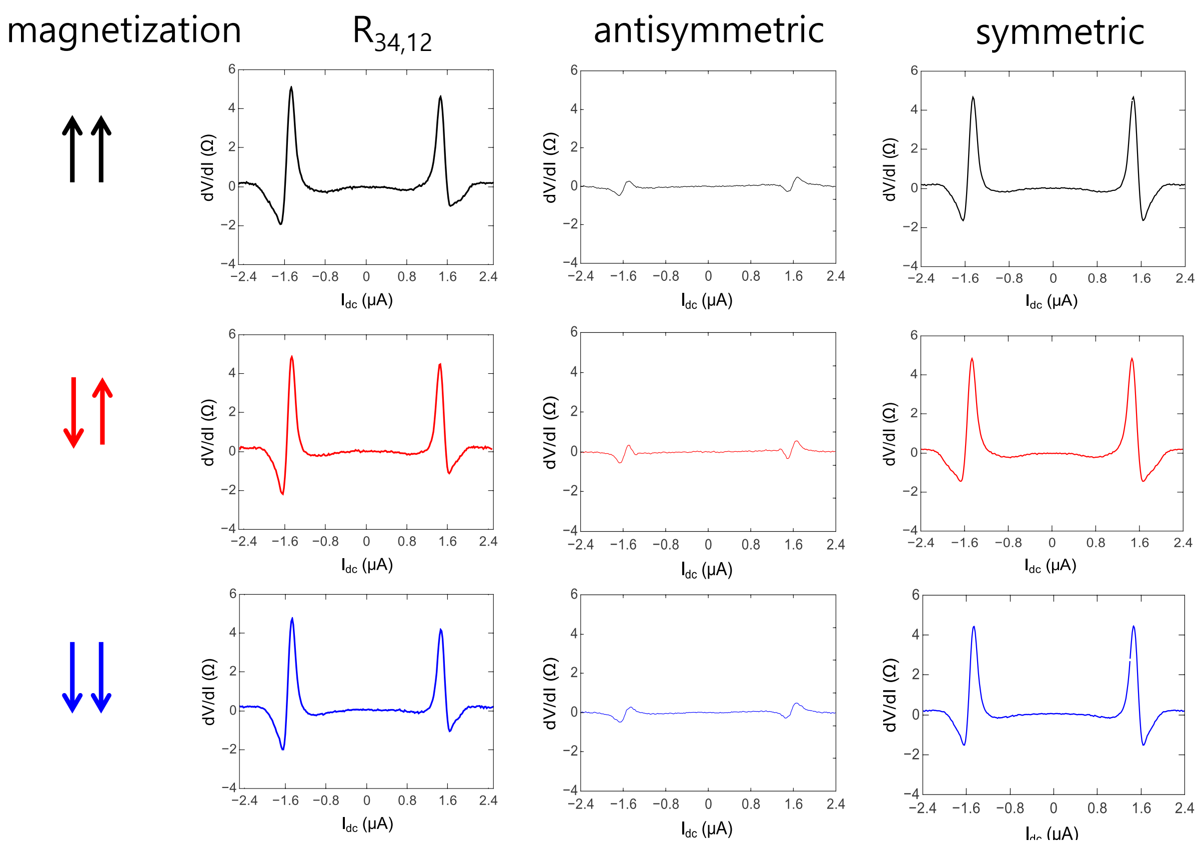

Figure 5.11. Differential resistance $R_{34,12}$ of "long" sample as a function of bias current with three different configurations of magnetization, ↑↑ (black), ↑↓ (red), and ↓↓ (blue). The antisymmetric and symmetric are presented along with the raw data.

although the magnitude is not comparable to that observed in the "short" sample, as shown in Figure 5.8.

Up to this point, we presented the experimental results on two samples including double FS junctions. While there are some noticeable differences in the data obtained from the two samples, the "short" sample and "long" sample, with different separations between two ferromagnets, a few interesting features are observed in common. i) The differential resistance of a specific measurement configuration, sending a current along a superconductor (SC2) and probing the voltage difference across the other superconductor (SC1), exhibits an

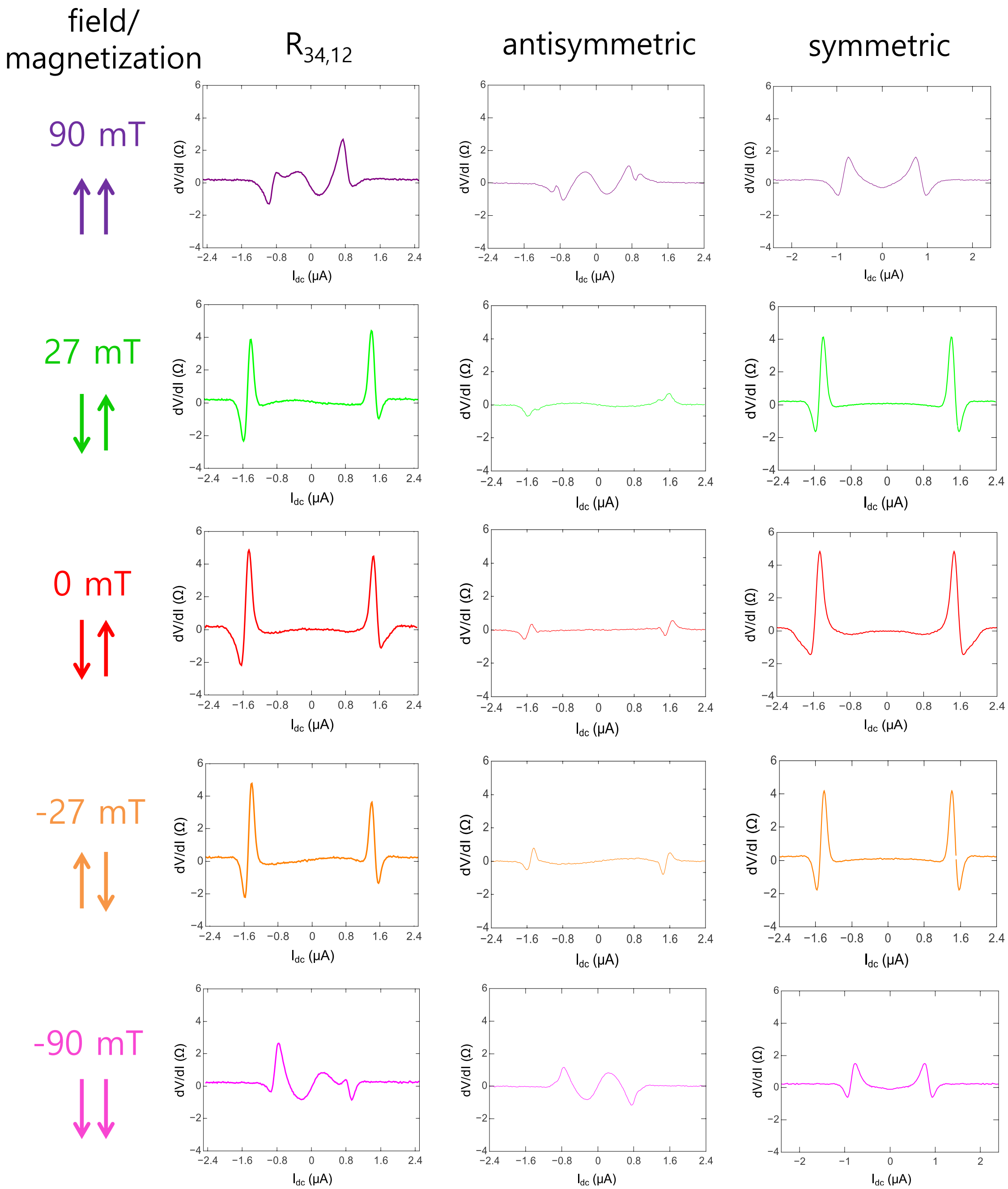

Figure 5.12. Differential resistance $R_{34,12}$ of "long" sample as a function of bias current at different values of the applied external magnetic field. The antisymmetric and symmetric are presented along with the raw data.

unexpected non-trivial dependence on the bias current. ii) The antisymmetric parts of the data show a set of a large peak and dip at a finite bias whose magnitude is highly dependent on the amplitude and the direction of the applied magnetic field. iii) In a smaller range of the bias in the antisymmetric parts, there is another set of a small peak and dip whose magnitude is modulated by the applied magnetic field as well. In case of the "short" sample, in particular, a clear dependence on the configuration of magnetization of this feature is observed.

Based on the discussion made ealier in this chaper on the experiments reported in the references [**55, 58, 59**], we may be able to associate the feature described in ii) with spin imbalance due to the Zeeman splitting in the DOS of quasiparticles in the superconductor by the applied magnetic field. However, unlike the results reported in the references, a set of a peak and a dip with a finite magnitude is present even at zero field in our result, which suggests that there might be a residual magnetic field generating spin imbalance even in the absence of the applied magnetic field. More interestingly, it should be noted that the feature explained in iii) was not observed in the references, which may be attributed to the fact that the ferromagnet and the superconductor formed a tunneling contact in the samples used in the references, not a transparent junction as in our samples. Since the mechanism that gives rise to the observed result in a small bias current is not understood yet, further study is required to examine if it is related to the phenomena occurring at FS interfaces, such as Andreev bound states (ABS) [**78**]. As it is difficult to further analyze what brings these interesting features in the differential resistance due to the complicated geometry of the sample, I believe that it might be worth fabricating samples with a simpler geometry with a single superconductor in future for further investigation in order to elucidate the origin of the observed features.

CHAPTER 6

Conclusion and Future directions

Several earlier studies [**1, 2, 3**] experimentally demonstrated that two nonlocal processes, crossed Andreev reflection (CAR) and elastic cotunneling (EC), attributed to nonlocal correlations mediated by a superconductor that manifest themselves as a finite nonlocal differential resistance near zero bias. Inspired by these previous works, we have experimentally investigated the nonlocal correlations in a proximity-coupled normal metal. Embedded between two Josephson-coupled superconductors, the proximity-coupled normal metal exhibits a finite nonlocal differential resistance whose bias dependence presents an overall resemblance to that observed in conventional NSN structures, except for a dip appearing in a small range of the bias near zero. However, a qualitative analysis revealed that the origin of the nonlocal differential resistance is rather different from what gives rise to the nonlocal differential resistance in NSN structures. The splitting of injected current into two paths due to the Josephson-coupling between two superconductors mainly contributes to the nonlocal differential resistance observed in the proximity-coupled normal metal even though the origin of the zero-bias dip is still not clarified in the simple analysis.

The zero-bias dip was of particular interest in our experiments as the nonlocal differential resistance in this range of bias showed a distinct dependence on the distance from the lead used for the injection of the current and the temperature. This led us to perform a quantitative analysis based on the quasiclassical theory of superconductivity in order to elucidate the origin of the zero-bias dip. Numerical calculations we performed have shown that the resistance of the proximity-coupled normal metal was expected to exhibit the reentrance behavior where a minimum of the resistance appears at a finite temperature T_{min} determined by two competing phenomena due to the proximity effect, the leakage of pair correlations and the opening of the gap in the density of states (DOS). While the numerical calculations showed that the zero-bias dip was associated with the decrease of the resistance due to the pair correlations in the proximity-coupled normal metal, the reentrance effect has not been observed in the experiments. In fact, further investigations suggested that the T_{min} may have been lowered below the temperatures accessible in the experiment due to i) non-ideal interface quality and ii) reduced proximity-effect as the effective distance between the proximity coupled normal metal and the superconducting reservoir is extended.

We further investigated the nonlocal correlations mediated by the proximity-coupled normal metal with a sample in a superconducting quantum interference device (SQUID) structure. In addition to a qualitative agreement with the experimental results obtained by the linear structure, the SQUID structure exhibited periodic oscillations as the phase between the two superconductor was modulated by an external magnetic field. This supports our argument that the zero-bias dip is associated with the leakage of pair correlations from both superconductors, more importantly, in a coherent manner. In addition, the design of the sample with multiple normal metal leads connected to the proximity-coupled normal metal provided us a capability of systematically studying the interplay between the quasiparticle current and the supercurrent in SNS junction, including the screening supercurrent generated in the presence of an external magnetic field. As a finite quasiparticle current I_{dc} is added, a finite phase difference is generated by the counter-flowing supercurrent occuring as a response to the injection of the current. This shifts the trace of the magnetic field dependence of the nonlocal differential resistance while an abrupt change of the resistance always occurs at odd multiples of the half flux quantum due to the switching of the screening supercurrent.

While the experimental results along with the analysis based on the numerical calculation helped us understand the physics behind the nonlocal correlations mediated by the proximity-coupled normal metal, there is still room for further exploration. For example, the superconducting wires in the samples can be replaced by a superconducting reservoir to observe if the strength of the proximity effect indeed affects the dependence of the nonlocal differential resistance on both bias and temperature. In that way, we might be able to finally confirm whether processes analogous to CAR and EC mediated by the proximity-coupled normal metal exist or not.

Additionally, the experiment on the transport through a heterostructure including double superconductor-ferromagnet (FS) interfaces exhibited interesting features. In addition to a set of a large peak and dip at finite bias current similar to the signature of spin imbalance due to the Zeeman splitting in the density of states (DOS) of the quasiparticles in a superconductor observed in recent experiments [**55, 58, 59**], an interesting feature was revealed in a small range of dc bias current, which might be related to spin-dependent phenomena such as Andreev bound state (ABS) recently observed in FS interfaces [**78**]. Due to the complexity of the geometry of the device in our experiment, further investigation in a simpler geometry is required in order to obtain the insight into the origin of the observed features.

References

[1] D. Beckmann, H. B. Weber, and H. v. Löhneysen, Phys. Rev. Lett. **93**, 197003 (2004).

[2] S. Russo, M. Kroug, T. M. Klapwijk, and A. F. Morpurgo, Phys. Rev. Lett. **95**, 027002 (2005).

[3] P. Cadden-Zimansky and V. Chandrasekhar, Phys. Rev. Lett. **97**, 237003 (2006).

[4] L. Hofstetter, S. Csonka, J. Nygard and C. Schönenberger, Nature **461**, 960 (2009).

[5] L. G. Herrmann, F. Portier, P. Roche, A. Levy Yeyati, T. Kontos, and C. Strunk, Phys. Rev. Lett. **104**, 026801 (2010).

[6] H. Kamerlingh Onnes, Leiden Comm. **120b, 122b, 124c** (1911).

[7] J. Bardeen, L. N. Cooper, and J. R. Schrieffer, Phys. Rev. **108**, 1175 (1957).

[8] L. N. Cooper, Phys. Rev. 104, 1189 (1956).

[9] O. Madelung, Introduction to Solid-State Theory (Springer-Verlag, 1978).

[10] G. E. Blonder, M. Tinkham, and T. M. Klapwijk, Phys. Rev. B **25**, 4515 (1982).

[11] A. F. Andreev, Zh. Eksp. Teor. Fiz. **46**, 1823 (1964) [Sov. Phys. JETP **19**, 1228 (1964)].

[12] A.F. Volkov, A.V. Zaitsev and T.M Klapwijk, Physica C **210**, 21 (1993).

[13] C.J. Lambert and R. Raimondi, J. Phys.: Condens. Matter **10**, 901 (1998).

[14] A.A. Golubov, F.K. Wilhelm, and A.D. Zaikin, Phys. Rev. B **55**, 1123 (1997).

[15] F.K. Wilhelm, A.D. Zaikin and G. Schön, J. Low Temp. Phys. **106**, 305 (1997).

[16] W. Belzig, F.K. Wilhelm, C. Bruder, G. Schön and A.D. Zaikin, Superlattices and Microstructures 25, 1251 (1999).

[17] W. Belzig, R. Shaikhaidarov, V. V. Petrashov, and Yu. V. Nazarov, Phys. Rev. B 66, 220505(R) (2002).

[18] Yu. V. Nazarov, Superlattices and Microstructures 25, 1221 (1999).

[19] V. Chandrasekhar, chapter in The Physics of Superconductors: Vol. II, Ed. K. H. Bennemann and J. B. Ketterson (Springer, Berlin, 2004).

[20] K. D. Usadel Phys. Rev. Lett. 25, 507 (1970).

[21] G. Eilenberger, Z. Phys **214**, 195 (1968).

[22] A.V. Zaitsev, Zh. Eksp. Teor. Fiz. **86**, 1742 (1984) [Sov. Phys. JETP **59**, 1015 (1985)].

[23] M. Yu. Kuprianov and V. F. Lukichev, Zh. Eksp. Teor. Fiz. **94**, 139 (1988) [Sov. Phys. JETP **67**, 1163 (1988)].

[24] S. -K. Yip, Phys. Rev. B **58**, 5803 (1998)

[25] Matthias Eschrig, Phys. Rev. B **61**, 9061 (2000).

[26] J. C. Hammer, J. C. Cuevas, F. S. Bergeret, and W. Belzig, Phys. Rev. B **76**, 064514 (2007).

[27] P. Virtanen and T. Heikkilä, Appl. Phys. A **89**, 625 (2007).

[28] S. N. Artemenko, A. F. Volkov, and A. V. Zaitsev, Solid State Comm. **30**, 771 (1979).

[29] Y. V. Nazarov, Phys. Rev. Lett. **73**, 1420 (1994).

[30] S. Yip, Phys. Rev. B **52**, 15504 (1995).

[31] Y. V. Nazarov and T. H. Stoof, Phys. Rev. Lett. **76**, 823 (1996).

[32] A. F. Volkov, N. Allsopp, C. J. Lambert, J. Phys.:Cond. Matt. **8**, L45 (1996).

[33] C.-J. Chien and V. Chandrasekhar, Phys. Rev. B **60**, 3655 (1999).

[34] P. Visani, A. C. Mota, and A. Pollini Phys. Rev. Lett. **65**, 1514 (1990).

[35] P. Charlat, H. Courtois, Ph. Gandit, D. Mailly, A. F. Volkov and B. Pannetier, Czech. J. Phys. 46, Supplement **S6**, 3107 (1996)

[36] W.L. McMillan, Phys. Rev. **175**, 537 (1968)

[37] A.A. Golubov and M.Yu. Kupriyanov, J. Low Temp. Phys. **70**, 83 (1988); Zh. Eksp. Teor. Fiz. **96**, 1420 (1989) [Sov. Phys. JETP **69**, 805 (1989)].

[38] W. Belzig, C. Bruder, and G. Schön, Phys. Rev. B **54**, 9443 (1996).

[39] F. Zhou, P. Charlat, B. Spivak, and B. Pannetier, J. Low Temp. Phys. **110**, 841 (1998).

[40] Dmitri A. Ivanov, Raphael von Roten, and Gianni Blatter, Phys. Rev. B **66**, 052507 (2002).

[41] H. le Sueur, P. Joyez, H. Pothier, C. Urbina, and D. Esteve, Phys. Rev. Lett. **100**, 197002 (2008).

[42] P. Dubos, H. Courtois, B. Pannetier, F. K. Wilhelm, A. D. Zaikin, and G. Schön, Phys. Rev. B **63**, 064502 (2001).

[43] H. Courtois, P. Charlat, Ph. Gandit, D. Mailly, B. Pannetier, J. of Low Temp. Phys. **116**, 187 (1999).

[44] P. Cadden-Zimansky, J. Wei and V. Chandrasekhar, Nat. Phys. **5**, 393 (2009).

[45] M. S. Crosser, Jian Huang, F. Pierre, Pauli Virtanen, Tero T. Heikkilä, F. K. Wilhelm, and Norman O. Birge. Phys. Rev. B **77**, 014528 (2008).

[46] J. M. Byers and M. E. Flatte, Phys. Rev. Lett. **74**, 306 (1995).

[47] G. Deutscher and D. Feinberg, Appl. Phys. Lett. **76**, 487 (2000).

[48] G. Falci, D. Feinberg, and F. W. J. Hekking, Europhys. Lett. **54**, 255 (2001).

[49] Bignon, M. Houzet, F. Pistolesi, and F. W. J. Hekking, Europhys. Lett. 67, 110 (2004).

[50] R. Mélin and D. Feinberg, Eur. Phys. Jour. B **26**, 101 (2002).

[51] A. Levy Yeyati, F. S. Bergeret, A. Martn-Rodero, and T. M. Klapwijk, Nat. Phys. **3**, 455 (2007).

[52] John Clarke, Phys. Rev. Lett. **28**, 1363 (1972).

[53] M. Tinkham and John Clarke, Phys. Rev. Lett. **28**, 1366 (1972).

[54] J. Brauer, F. Hubler, M. Smetanin, D. Beckmann, and H. v. Löhneysen, Phys. Rev. B **81**, 024515 (2010).

[55] F. Hübler, J. Camirand Lemyre, D. Beckmann, and H. v. Löhneysen, Phys. Rev. B **81**, 184524 (2010).

[56] K. Yu. Arutyunov, H.-P. Auraneva, and A. S. Vasenko, Phys. Rev. B **83**, 104509 (2011).

[57] F. Hübler, M. J. Wolf, D. Beckmann, and H. v. Löhneysen, Phys. Rev. Lett. **109**, 207001 (2012).

[58] M. J. Wolf, F. Hübler, S. Kolenda, H. v. Löhneysen, and D. Beckmann, Phys. Rev. B **87**, 024517 (2013).

[59] C. H. L. Quay, D. Chevallier, C. Bena, M. Aprili, Nat. Phys. **9**, 84 (2013).

[60] F. J. Jedema, A. T. Filip and B. J. van Wees, Nature **410**, 345 (2001).

[61] S. Takahashi and S. Maekawa, Phys. Rev. B **67**, 052409 (2003).

[62] Jonghwa Eom, Ph.D. Thesis, Northwestern University (1998).

[63] Chen-jung Chien, Ph.D. Thesis, Northwestern University (1998).

[64] Jose Aumentado, Ph.D. Thesis, Northwestern University (2000).

[65] Zhigang Jiang, Ph.D. Thesis, Northwestern University (2005).

[66] Zhengfan Zhang, Ph.D. Thesis, Northwestern University (2006).

[67] Paul Cadden-Zimansky, Ph.D. Thesis, Northwestern University (2008).

[68] Manan Mehta, Ph.D. Thesis, Northwestern University (2015).

[69] Samuel Davis, Ph.D. Thesis, Northwestern University (2017).

[70] Varada Bal, Ph.D. Thesis, Northwestern University (2018).

[71] B. Cord, C. Dames, K. Berggren, and J. Aumentado, J. Vac. Sci. Tech. B **24**, 3139 (2006).

[72] H.-S. Chang, J. P. Pon, K.-C. Hsieh, and C. C. Chen, J. Electron. Mater. **30**, 1171 (2001).

[73] M. Tinkham, Introduction to Superconductivity (Second Edition, Dover, Mineola, NY, 1996).

[74] P. Virtanen, PhD Thesis, Helsinki University of Technology (2009).

[75] E. A. Demler, G. B. Arnold, and M. R. Beasley, Phys. Rev. B **55**, 15174 (1997).

[76] V. V. Ryazanov, V. A. Oboznov, A. Yu. Rusanov, A. V. Veretennikov, A. A. Golubov, and J. Aarts, Phys. Rev. Lett. **86**, 2427 (2001).

[77] T. Kontos, M. Aprili, J. Lesueur, F. Genêt, B. Stephanidis, and R. Boursier Phys. Rev. Lett. **89**, 137007 (2002).

[78] F. Hübler, M. J. Wolf, T. Scherer, D. Wang, D. Beckmann, and H. v. Lhneysen Phys. Rev. Lett. 109, 087004 (2012).

[79] S. Teukolsky, W. H. Press, W. T. Vetterling, B. P. Flannery, chapter in Numerical Recipes in C: The Art of Scientific Computing (1986).

APPENDIX A

Recipe for numerical simulation

I would like to briefly describe the relaxation method that we used in the numerical simulation presented in Chapter 2. Since the majority of basics on formulating the relaxation method is borrowed from the reference written by Teukolsky *et al.* [**79**], I recommend the reference for the detailed explanation. The original codes for performing the numerical calculation sketched here were written in IDL (Interactive Data Language) by Prof. Venkat Chandrasekhar to produce the results presented in Ref. [**19**], and the modified codes were written in Python by the author to produce the results presented in this thesis.

The problem that we treat here is categorized as *two point boundary value problem* (TP-BVP) where boundary conditions are given at two points, usually at the end points. To be more specific, the problem is to find the solution of N coupled first-order ordinary differential equations (ODE), satisfying n_1 boundary conditions at the starting point x_1, and $n_2 = N - n_1$ boundary conditions at the final point x_2. The differential equations are given as

$$\frac{dy_i(x)}{dx} = g_i(x, y_1, y_2, \cdots, y_N) \qquad i = 1, 2, \cdots, N. \tag{A.1}$$

The boundary conditions at x_1 and x_2 are given as

$$B_{1j}(x_1, y_1, y_2, \cdots, y_N) \;=\; 0 \qquad j = 1, \cdots, n_1 \tag{A.2}$$

$$B_{2k}(x_2, y_1, y_2, \cdots, y_N) \;=\; 0 \qquad j = 1, \cdots, n_2 \tag{A.3}$$

The first step in relaxation method is to replace the ODEs by approximate finite-difference equations (FDEs) on a set of mesh points that spans the domain of interest. For example, a first-order ODE

$$\frac{dy}{dx} = g(x, y) \tag{A.4}$$

can be replaced by

$$y_k - y_{k-1} - (x_k - x_{k-1})\, g\left[\frac{1}{2}(x_k + x_{k-1}), \frac{1}{2}(y_k + y_{k-1})\right] = 0 \tag{A.5}$$

where k runs from 2 to N. If we consider N coupled first order ODEs on a mesh of M points, the solution can be represented as a vector $\mathbf{y}_k$ including the entire set of $y_1, y_2, \cdots, y_N$ at x_k as the elements. Since the solution should be found for all M mesh points, represented as $y_{j,k}$ ($j = 1, 2, \cdots, N$, $k = 1, 2, \cdots, M$), the total number of unknown is MN. For the point x_k, the above FDE is given by

$$0 = \mathbf{E}_k \equiv \mathbf{y}_k - \mathbf{y}_{k-1} - (x_k - x_{k-1})\mathbf{g}_k(x_k, x_{k-1}, \mathbf{y}_k, \mathbf{y}_{k-1}). \qquad k = 2, 3, \cdots, M \tag{A.6}$$

Therefore, the FDEs provide $N(M-1)$ equations for the MN unknowns and the rest N equations are given by the boundary conditions $\mathbf{E}_1 \equiv \mathbf{B}(x_1, \mathbf{y}_1)$ at the first point x_1 and $\mathbf{E}_{M+1} \equiv \mathbf{C}(x_M, \mathbf{y}_M)$ at the final point x_M.

By expanding the FDEs in first-order Taylor series with respect to a small change $\Delta\mathbf{y}_k$, we obtain

$$\mathbf{E}_k(\mathbf{y}_k + \Delta\mathbf{E}_k, \mathbf{E}_{k-1} + \Delta\mathbf{E}_{k-1}) \simeq \mathbf{E}_k(\mathbf{y}_k, \mathbf{E}_{k-1}) + \sum_{n=1}^{N} \frac{\partial \mathbf{E}_k}{\partial y_{n,k-1}} \Delta y_{n,k-1} + \sum_{n=1}^{N} \frac{\partial \mathbf{E}_k}{\partial y_{n,k}} \Delta y_{n,k} \tag{A.7}$$

for interior points, $k = 2, 3, \cdots, M$. For the solution, $\mathbf{E}(\mathbf{y} + \boldsymbol{\Delta}\mathbf{y})$ should be become zero upon the change of $\Delta\mathbf{y}_k$, which leads to

$$\sum_{n=1}^{N} S_{j,n}\Delta y_{n,k-1} + \sum_{n=N+1}^{2N} S_{j,n}\Delta y_{n-N,k} = -E_{j,k}, \quad j = 1, 2, \cdots, N \tag{A.8}$$

where

$$S_{j,n} = \frac{\partial E_{j,k}}{\partial y_{n,k-1}}, \;\; S_{j,n+N} = \frac{\partial E_{j,k}}{\partial y_{n,k}}, \;\; n = 1, 2, \cdots, N \tag{A.9}$$

The quantity $S_{j,n}$ is an $N \times 2N$ matrix at each point x_k. A similar approach can be made at the boundaries as

$$\sum_{n=1}^{N} S_{j,n}\Delta y_{n,1} = -E_{j,1} \;\; j = 1, \cdots, n_1 \tag{A.10}$$

where $S_{j,n} = \frac{\partial E_{j,1}}{\partial y_{n,1}}$ with $n = 1, 2, \cdots, N$ for the first boundary and

$$\sum_{n=1}^{N} S_{j,n}\Delta y_{n,M} = -E_{j,M+1}, \quad j = 1, \cdots, n_2 \tag{A.11}$$

where $S_{j,n} = \frac{\partial E_{j,M+1}}{\partial y_{n,M}}$ with $n = 1, 2, \cdots, N$ for the second boundary. By constructing single column vectors $\Delta\mathbf{y}$ consisting of $\Delta\mathbf{y}_k$ and $\mathbf{E}$ consisting of $\mathbf{E}_k$, we can set up a matrix equation $\mathbf{S}\boldsymbol{\Delta}\mathbf{y} = -\mathbf{E}$, where the dimension of $\mathbf{S}$, $\Delta\mathbf{y}$, and $\mathbf{E}$ is $NM \times NM$, NM, and NM respectively. The structure of the matrix equation is schematically shown in Figure A.1 to help the visualization of the matrix equation.

The procedure to find the solution is as the following: First, an initial guess for the solution $y_{j,k}$ should be made. Then, based on the initial guess, the matrices $\mathbf{S}$ and $\mathbf{E}$ are constructed. By solving the matrix equation $\mathbf{S}\boldsymbol{\Delta}\mathbf{y} = -\mathbf{E}$, the vector $\Delta\mathbf{y}$ can be found,

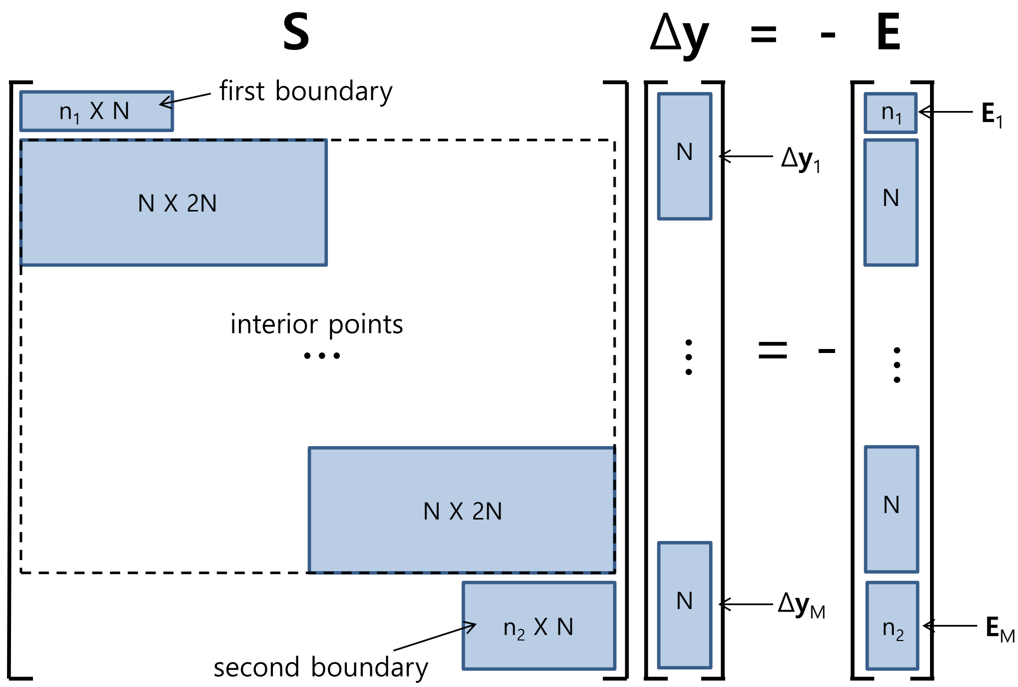

Figure A.1. The structure of the matrix equation is schematically shown where the dimension of $\mathbf{S}$, $\Delta\mathbf{y}$, and $\mathbf{E}$ is $NM \times NM$, NM, and NM respectively.

which is used to set the new solution for the next iteration of constructing and solving the same matrix equation. This process goes on until the amplitude of the vector $\Delta\mathbf{y}$ becomes vanishingly small.

Let me elaborate the procedure with an example. The task is to solve the Usadel equation for a normal metal wire between a normal metal reservoir and a superconducting reservoir, as shown in Figure 2.5 in Chapter 2. The Usadel equation is given in equation 2.31a and 2.31b. As explained before, the equations are normalized by the Thouless energy $E_T = \hbar D/L_0^2$ if the length of the wire under consideration is L_0, which results in equation 2.56a and 2.56b. Then the equations are split into four first-order ODEs as given in equation 2.57. Since we treated the real and imaginary part of θ, θ', ϕ, and ϕ' separately, we have 8 first-order ODEs for 8 variables $y_1 = \mathbf{Re}(\theta)$, $y_2 = \{\mathbf{Re}(\theta)\}'$, $y_3 = \mathbf{Im}(\theta)$, $y_4 = \{\mathbf{Im}(\theta)\}'$, $y_5 = \mathbf{Re}(\phi)$,

$y_6 = \{\mathbf{Re}(\phi)\}'$, $y_7 = \mathbf{Im}(\phi)$, and $y_8 = \{\mathbf{Im}(\phi)\}'$, which can be replaced by FDEs for the interior points x_k $(k = 2, 3, \cdots, M)$ as the following.

(A.12)

$$
\begin{aligned}
E_{1,k} &= (y_{1,k} - y_{1,k-1}) - \frac{h}{2}(y_{2,k} + y_{2,k-1}) \\
E_{2,k} &= (y_{2,k} - y_{2,k-1}) - h\epsilon \left[\cos(y_{1,k})\sinh(y_{3,k}) + \cos(y_{1,k-1})\sinh(y_{3,k-1})\right] \\
&- \frac{h}{4}\left[(y_{6,k}^2 - y_{8,k}^2)\sin(2y_{1,k})\cosh(2y_{3,k}) + (y_{6,k-1}^2 - y_{8,k-1}^2)\sin(2y_{1,k-1})\cosh(2y_{3,k-1})\right] \\
&+ \frac{h}{2}\left[y_{6,k}\, y_{8,k}\cos(2y_{1,k})\sinh(2y_{3,k}) + y_{6,k-1}\, y_{8,k-1}\cos(2y_{1,k-1})\sinh(2y_{3,k-1})\right] \\
E_{3,k} &= (y_{3,k} - y_{3,k-1}) - \frac{h}{2}(y_{4,k} + y_{4,k-1}) \\
E_{4,k} &= (y_{4,k} - y_{4,k-1}) + h\epsilon \left[\sin(y_{1,k})\cosh(y_{3,k}) + \sin(y_{1,k-1})\cosh(y_{3,k-1})\right] \\
&- \frac{h}{4}\left[(y_{6,k}^2 - y_{8,k}^2)\cos(2y_{1,k})\sinh(2y_{3,k}) + (y_{6,k-1}^2 - y_{8,k-1}^2)\cos(2y_{1,k-1})\sinh(2y_{3,k-1})\right] \\
&- \frac{h}{2}\left[y_{6,k}\, y_{8,k}\sin(2y_{1,k})\cosh(2y_{3,k}) + y_{6,k-1}\, y_{8,k-1}\sin(2y_{1,k-1})\cosh(2y_{3,k-1})\right] \\
E_{5,k} &= (y_{5,k} - y_{5,k-1}) - \frac{h}{2}(y_{6,k} + y_{6,k-1}) \\
E_{6,k} &= \left[y_{6,k} - y_{6,k}\cos(2y_{1,k})\cosh(2y_{3,k}) - y_{8,k}\sin(2y_{1,k})\sinh(2y_{3,k})\right] \\
&- \left[y_{6,k-1} - y_{6,k-1}\cos(2y_{1,k-1})\cosh(2y_{3,k-1}) - y_{8,k-1}\sin(2y_{1,k-1})\sinh(2y_{3,k-1})\right] \\
E_{7,k} &= (y_{7,k} - y_{7,k-1}) - \frac{h}{2}(y_{8,k} + y_{8,k-1}) \\
E_{8,k} &= \left[y_{8,k} - y_{8,k}\cos(2y_{1,k})\cosh(2y_{3,k}) + y_{6,k}\sin(2y_{1,k})\sinh(2y_{3,k})\right] \\
&- \left[y_{8,k-1} - y_{8,k-1}\cos(2y_{1,k-1})\cosh(2y_{3,k-1}) + y_{6,k-1}\sin(2y_{1,k-1})\sinh(2y_{3,k-1})\right]
\end{aligned}
$$

which is in a total of $8(M-1)$ equations where $\epsilon = E/E_T$ and $h = 1/M$. As explained before, the rest 8 equations come from the boundary condition, 4 at the first point and 4 at the final point. θ_0 for a superconducting reservoir is given in equation 2.38. Since the first point is connected to a normal reservoir (N) where $\Delta = 0$, $\theta_0 = 0$. By setting $\phi = 0$ for this problem, we have $y_{1,1} = 0$, $y_{3,1} = 0$, $y_{5,1} = 0$, and $y_{7,1} = 0$, which leads to FDEs as

$$\begin{aligned} E_{1,1} &= y_{1,1} \\ E_{2,1} &= y_{3,1} \\ E_{3,1} &= y_{5,1} \\ E_{4,1} &= y_{7,1}, \end{aligned} \tag{A.13}$$

whereas for the final point connected to a superconducting reservoir (S),

$$\begin{aligned} E_{1,M+1} &= y_{1,M+1} - \mathbf{Re}(\theta_0) \\ E_{2,M+1} &= y_{3,M+1} - \mathbf{Im}(\theta_0) \\ E_{3,M+1} &= y_{5,M+1} \\ E_{4,M+1} &= y_{7,M+1}. \end{aligned} \tag{A.14}$$

With the matrix $\mathbf{E}$ constructed from the FDEs, we can construct the matrix $\mathbf{S}$ by using the definition for the element $S_{j,n}$ given above.

In order to start the iteration of solving $\mathbf{S\Delta y} = -\mathbf{E}$, one needs to make a guess for an initial solution as explained before. For a point $x_k = h(k-1) = \frac{k-1}{M}$ $(k = 1, \cdots, M+1)$, the initial solution is simply set by a linear function as

$$
\begin{aligned}
y_{1,k} &= \mathbf{Re}(\theta_0) \times x_k \\
y_{3,k} &= \mathbf{Im}(\theta_0) \times x_k \\
y_{5,k} &= 0 \\
y_{7,k} &= 0.
\end{aligned}
\tag{A.15}
$$

Then the iteration is repeated until the amplitude of vector $\mathbf{\Delta y}$ diminishes. The initial solution that we set and the final solution of the Usadel equation is shown in Figure A.2 for $\epsilon = E/E_T = 10$ and $\Delta = 1000E_T$. In this manner, the Usadel equation can be numerically solved for various values of energy, which provides the spectral properties of the system under consideration.

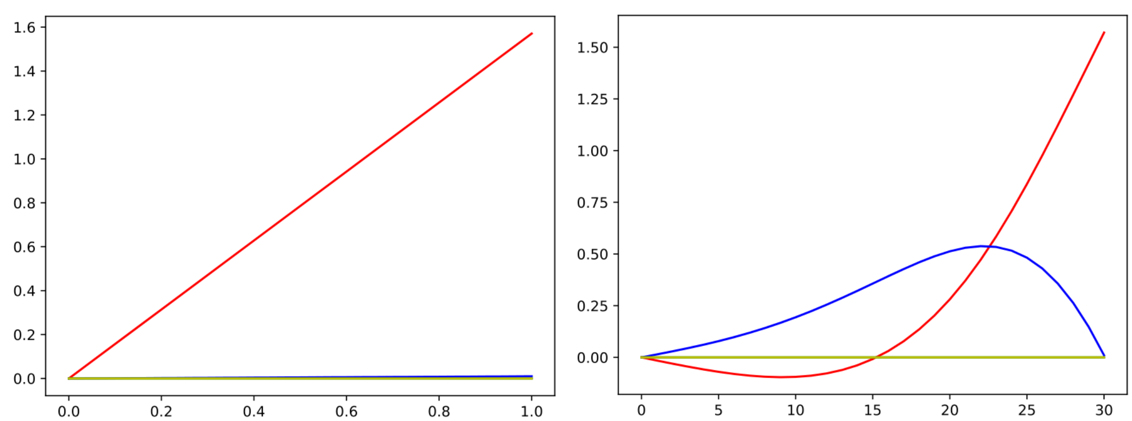

Figure A.2. The initial and the final solution of the Usadel equation. Red: $y_1 = \mathbf{Re}(\theta)$, Blue: $y_3 = \mathbf{Im}(\theta)$, Green: $y_5 = \mathbf{Re}(\phi)$, Yellow: $y_7 = \mathbf{Im}(\phi)$.